Chapter 5

Simultaneous determination of J_c^G, J_c^{GB} and grain size: application to different experimental conditions

In the previous chapter we have presented a new methodology based on dc-magnetometry that has enabled us to determine simultaneously the grain and grain boundary critical current densities of coated conductors and therefore, allowed us to analyze independently the critical currents associated to the Abrikosov vortices (AV) within the grains and to Abrikosov-Josephson vortices (AJV) at the grain-boundaries, respectively (see section 1.4.2).

In this chapter we present a complete study of the interaction of these two critical current densities and the dependence of both on fundamental parameters such as type of substrate, growth process, YBCO texture, YBCO thickness, as well as

effects from modifications induced at the grain boundaries by mechanical deformation of the tapes.

5.1 MAGNETIC GRAIN SIZE OF CCS ON IBAD AND RABITS SUBSTRATES

YBCO grains are usually a replica of the underneath biaxially-textured substrate grain-structure [48] and therefore, the grain size and grain to grain alignment of the superconducting layers is basically predetermined by the chosen substrate. IBAD and RABiTS substrates are characterized by very different grain sizes. A typical IBAD substrate has grains of about 0.5-3σm, while for a RABiTS substrate one has grains of about 30-100σm, and consequently are the YBCO grains grown on top.

The average magnetic grain size of a certain coated conductor (see section 3.4.2) can be calculated by means of magnetic measurements of hysteresis loops with the determination of the experimental values H_{peak}^{sat} and $H_m(M_{rem}^{sat})$ and using equation 4-10 (i.e. $H_{peak}^{sat}/H_m(M_{rem}^{sat})=g(a/t)$), which only depends on the grain size, 2a, and the thickness of the YBCO layer. As it has been discussed in section 3.4.2, the magnetic grain size depends on the ratio J_c^{GB}/J_c^G, since the current loops that are formed inside the grains (which define the magnetic grain size) fill a larger region of the structural grain for small values of J_c^{GB}/J_c^G.

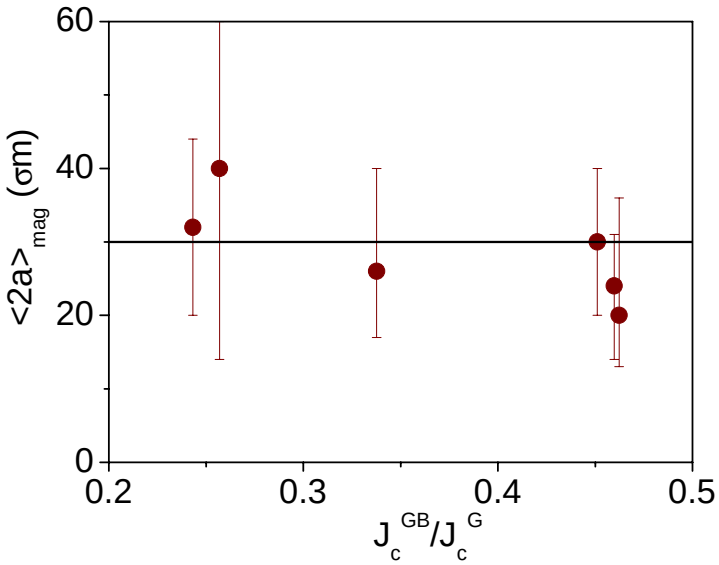

Fig. 5-1. Magnetic grain size calculated for different RABiTS samples as a function of the ratio J_c^{GB}/J_c^G.

Fig. 5-1 shows the magnetic grain size calculated for several RABiTS samples grown by ex situ BaF_2 process on similar nickel substrates with different ratio J_c^{GB}/J_c^G. The values that we have obtained for all the RABiTS samples can be considered

constant within the error, with an average value of <2a> ℑ30σm (solid line in the figure). This value is slightly smaller than the structural grain size measured for these substrates, $<2a>_{subs}$ ℑ45σm, since J_c^{GB} is different from zero, although we see that it does not strongly depend on the ratio J_c^{GB}/J_c^G, within the range analyzed.

Fig. 5-2 shows the grain critical current density, determined by means of equation 4-7 (i.e. J_c^G ℑH_{peak}^{sat}/xt), where x is a numerical factor depending on the calculated grain size, as a function of the average grain size, <2a>, obtained for several IBAD and RABiTS conductors, analyzed at 77K.

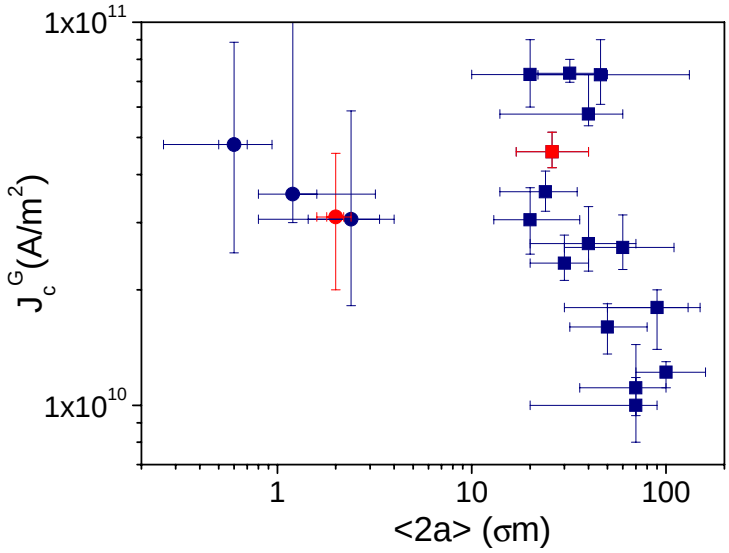

Fig. 5-2. Grain critical current at 77K as a function of the average grain size determined for several IBAD (⌀) and RABiTS (y) coated conductors. Samples where supplied by ORNL (USA), Zentrum für FunktionWekstoffe (Germany) and IFW (Germany).

The values of <2a> found for the different IBAD samples go from <2a>=0.5σm to 2.5σm, whereas for RABiTS samples a clearly larger grain size is detected with <2a>=20-100σm, depending on the type of Nickel substrate. These magnetic grain sizes are consistent with the structural grains determined by EBSD for the two types of CCs (section 2.2.3). Fig. 5-3 shows the grain maps obtained by EBSD for a YBCO layer of a standard IBAD sample ($IBADt1.13_{ORNL-B}$) and for a RABiTS sample ($RABt0.49_{ORNL-B}$). These two samples are shown in red in Fig. 5-2. Notice that the values of <2a> that we got (<2a>=2σm for the IBAD CC and 26σm for the RABiTS CC), agrees with the average grain size shown in the EBSD maps.

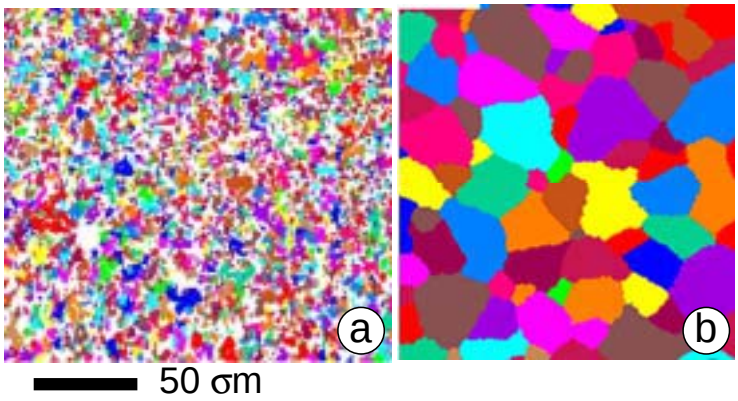

Fig. 5-3. EBSD maps of the YBCO layer obtained for the IBAD CC IBADt1.13$_{ORNL-B}$ (a) and for the RABiTS CC RABt0.49$_{ORNL-B}$ (b). A grain is defined as a contiguous set of points aligned within 1∀ Colours are assigned only to identify unique grains and do not reflect grain orientation.

The J_c^G values shown in Fig. 5-2 are quite different from sample to sample owing to the different growth conditions and thickness of the YBCO layer. However, the large values obtained, $J_c^G(77K)=1.10^{10}A/m^2$-$7.10^{10}A/m^2$, which are in the expected range of YBCO thin films grown on single crystals, indicate that all these coated conductors are of very high quality. Additionally one can observe that the same range of J_c^G can be obtained indistinctly for both types of coated conductors indicating that similar Abrikosov vortex pinning force can be achieved at the grains of IBAD and RABiTS coated conductors, although they have been grown with different methods (PLD or BaF_2) and they present very different grain sizes.

5.1.1 UNCORRELATED YBCO AND SUBSTRATE GRAIN-BOUNDARY NETWORKS

YBCO films produced by the ex situ conversion BaF_2-based precursors are characterized by a biaxially aligned laminar grain structure that results from the anisotropic growth characteristics of the YBCO phase and its formation from a transient liquid phase during the conversion process [82-84]. If the process is optimized , the amount of liquid phase during the growth can be minimized and thus, the grain structure formed is a replica of the underneath biaxially-textured substrate (Fig. 5-4a). However, if the growth process occurs with an excess of liquid formation, it generates an epitaxial YBCO grain structure overgrowing the substrate grain boundary network and the final grain size for the YBCO is larger than the substrate grain size (Fig. 5-4b) [85]. Hence, liquid mediated growth processes are able to control the conditions for replicating the grain boundary networks of the substrate.

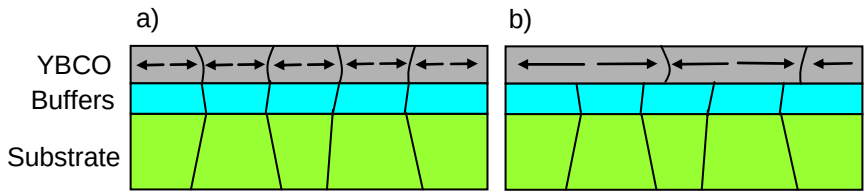

Fig. 5-4. Cross section scheme of the grain structure of a YBCO CC where the YBCO grains replicate the underneath substrate (a) and where the YBCO grains overgrow the substrate grains (b).

It has been reported recently that in IBAD type coated conductors of thickness larger than 2σm, even a bi-modal structure across the thickness has been observed [86] suggesting different growth events. Fig. 5-5 shows a TEM image of the sample IBADt2.90$_{ORNL-A}$ where a bilayered structure can be distinguished. A submicron grain size is observed at the top of the YBCO film, while very large grains, up to 50-80 σm are found in the bottom half of the film.

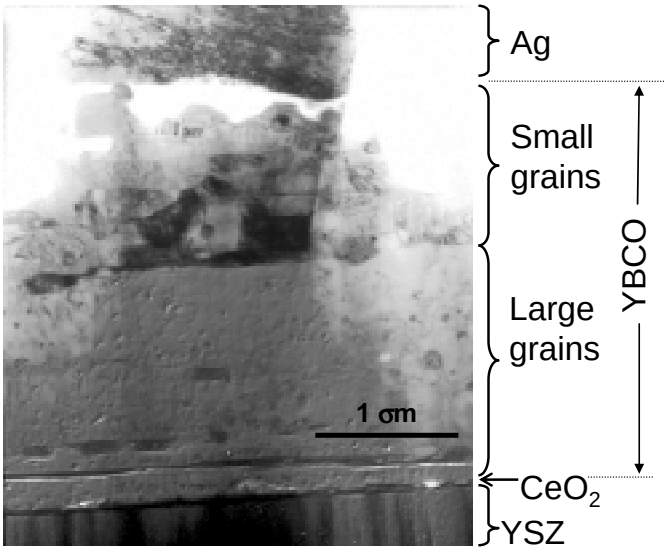

Fig. 5-5. Cross-sectional TEM image of the sample IBADt2.90$_{ORNL-A}$, showing a bilayer structure.

In this section we will analyze different IBAD and RABiTS coated conductors, grown by the ex situ conversion BaF_2-based precursors, whose GBs replicate the substrate GB network and conductors where the YBCO GB clearly overgrew those from the substrates. In particular IBADt2.90$_{ORNL-A}$, initially grown as a 2.9σm thick YBCO layer, with a bimodal structure was thinned down to 1.33σm by ion milling, ensuring that only large grains, ℑ50-80σm, where present in the remaining film, IBADt1.33$_{ORNL-A}^{mill}$. This sample will be an example of a YBCO GB network largely overgrowing the IBAD GB structure since the characteristic grain size for a typical IBAD coated conductor which replicates the GB substrate structure is about 1σm. A contrasting case is observed for an IBAD sample with tℑ1.1σm (IBADt1.13$_{ORNL-B}$), which

presents a much smaller grain size, ℑ1-2σm, consistent with a controlled liquid mediated process expected from a film grown with optimized conditions [58]. This work has been done in collaboration with ORNL, who supplied the samples to analyze, and with LANL and UW who provided the TEM and EBSD analysis, respectively.

Fig. 5-6 shows magneto-optical images obtained for a) the 1.1σm IBAD sample which YBCO layer replicates the substrate GB, IBADt1.13$_{ORNL-B}$ and b) the 2.9σm IBAD sample, milled down to 1.33σm, IBADt1.33$_{ORNL-A}^{mill}$, after zero field cooling the samples at 77K and applying a magnetic field of 50mT.

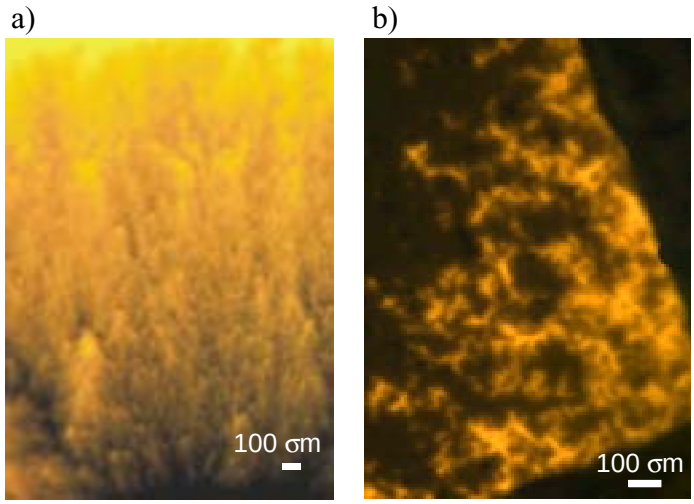

Fig. 5-6. Magneto-optical images for IBADt1.13$_{ORNL-B}$ (a) and IBADt1.33$_{ORNL-A}^{mill}$ (b) after zero field cooling the samples at 77 K and applying a magnetic field of 50 mT, respectively.

Due to different grain structures these two samples present a very different pattern of magnetic flux penetration. Fig. 5-6a displays a typical MO image of an IBAD CC with grains in the range of the MO resolution, which is a few microns. On the contrary, in Fig. 5-6b we clearly identify the penetration of magnetic flux into a GB network with grains in the range of 50-80σm, thus indicating that the micron grain size of the substrate is not replicated in the YBCO layer.

The different grain size of these two IBAD samples has also been observed by EBSD maps of the YBCO GBs. Fig. 5-7 presents the EBSD grain map of the YBCO layer obtained for IBADt1.13$_{ORNL-B}$ (a) and IBADt1.33$_{ORNL-A}^{mill}$ (b), where colours are assigned to identify points aligned within 1^o. The EBSD pattern confirms the presence of YBCO grains over 50σm-80σm in size for the sample IBADt1.33$_{ORNL-A}^{mill}$ while small grains of about 1σm are observed for IBADt1.13$_{ORNL-B}$, in full agreement with the MO result.

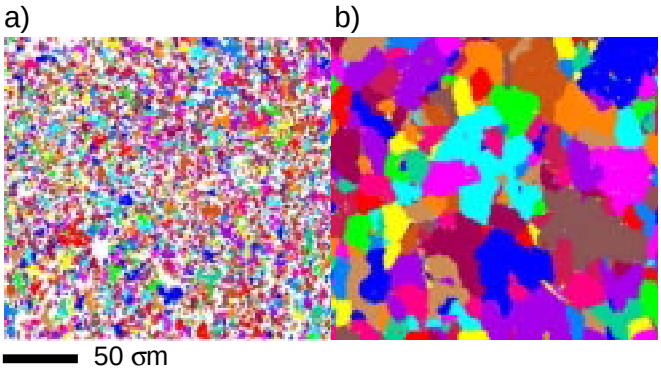

Fig. 5-7. Grain maps produced by EBSD of the $YBa_2Cu_3O_7$ layer of $IBADt1.13_{ORNL\text{-}B}$ (a) and $IBADt1.33_{ORNL\text{-}A}^{mill}$ (b) where a grain is identified as a contiguous set of points aligned within 1°.Colors are assigned to identify unique grains and do not reflect grain orientation.

We performed magnetization hysteresis loops in order to determine the critical current densities and average magnetic grain size of both IBAD samples. Fig. 5-8 displays a comparison of the saturated reverse branches of the M(H) curve at 77K for both samples. Notice that the two curves present a peak of magnetization at very different $\sigma_0 H_a$. $IBADt1.13_{ORNL\text{-}B}$ with the smallest grain size (open symbols) peaks at $\sigma_0 H_{peak}^{sat}$=0.006T while $IBADt1.33_{ORNL\text{-}A}^{mill}$ (closed symbols) peaks at $\sigma_0 H_{peak}^{sat}$=0.044T. The maximum magnetic field needed to saturate the remanent magnetization have also been determined with minor loops being, $\sigma_0 H_m(M_{rem}^{sat})$=0.045T and 0.075T for $IBADt1.13_{ORNL\text{-}B}$ and $IBADt1.33_{ORNL\text{-}A}^{mill}$, respectively (see Fig. 5-9). With these two experimental values, $\sigma_0 H_{peak}^{sat}$ and $\sigma_0 H_m(M_{rem}^{sat})$, the average grain size <2a> of each sample can be determined by means of equation 4-10 (i.e. $H_{peak}^{sat}/H_m(M_{rem}^{sat})=g(a/t)$).

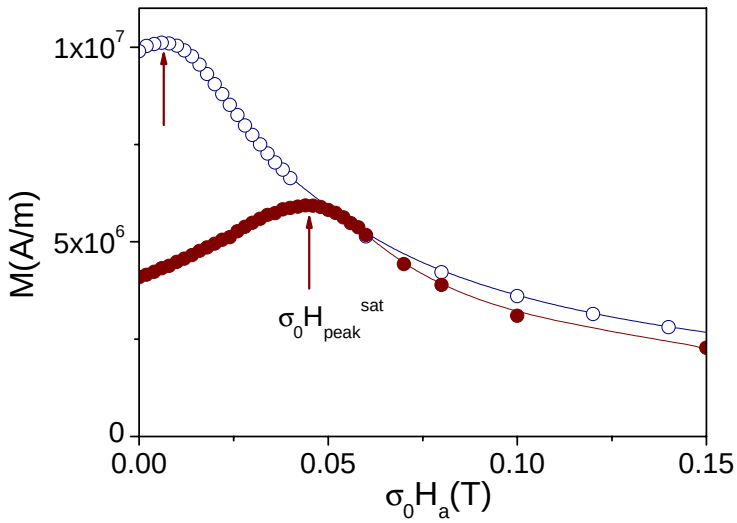

Fig. 5-8.Saturated reverse branches of the magnetization curve for $IBADt1.13_{ORNL\text{-}B}$ (open symbols) and $IBADt1.33_{ORNL\text{-}A}^{mill}$ (closed symbols) at 77K. The saturated peak position, $\sigma_0 H_{peak}^{sat}$, is indicated in arrows.

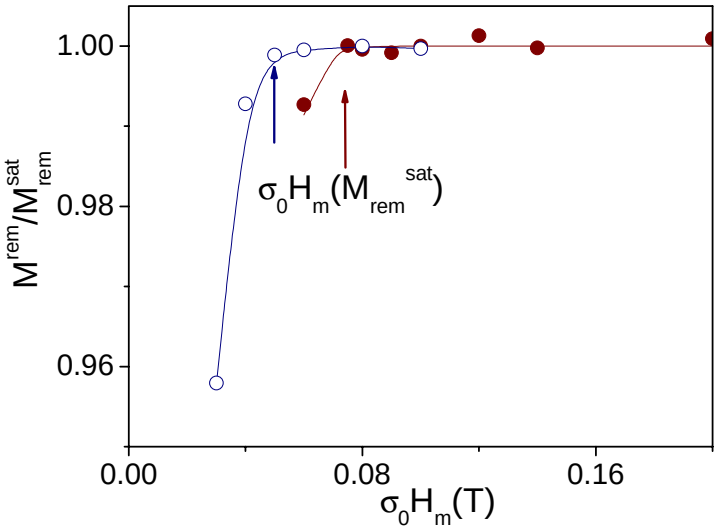

Fig. 5-9. Saturation of the remanent magnetization for IBADt1.13$_{ORNL-B}$ (open symbols) and IBADt1.33$_{ORNL-A}^{mill}$ (closed symbols) at 77K, where the maximum applied field required to saturate M_{rem}, $\sigma_0 H_m(M_{rem}^{sat})$ is indicated.

The same analysis has also been performed at two YBCO RABiTS samples grown with conditions similar to the two IBAD samples. RABt1.01$_{ORNL-B}$, with t=1σm, grown with an optimized process which controls the amount of liquid formation (process B) and RABt1.08$_{ORNL-A}$ with t=1.1σm grown with an uncontrolled process that induce an excess of liquid (process A). Fig. 5-10 shows the values of $g(a/t)=H_{peak}^{sat}/H_m(M_{rem}^{sat})$, obtained for the two IBAD CCs analyzed above (IBADt1.13$_{ORNL-B}$ and IBADt1.33$_{ORNL-A}^{mill}$) and for these two RABiTS CCs. Since all four samples have almost the same thickness (about 1σm) the larger value of g is an indication of a larger grain size <2a>. From this data we have obtained grain sizes of <2a>=2σm and 70σm for IBADt1.13$_{ORNL-B}$ and IBADt1.33$_{ORNL-A}^{mill}$, respectively, in clear agreement with the MO and EBSD data shown above. The determined grain size values for RABt1.01$_{ORNL-B}$ and RABt1.08$_{ORNL-A}$ are 20σm and 60σm, respectively. So that, we observe that in the case of the RABiTS samples we also detect a large grain size for the sample processed with an excess of liquid formation during the grown, although the difference in grain size is not as significant as in the case of IBAD samples.

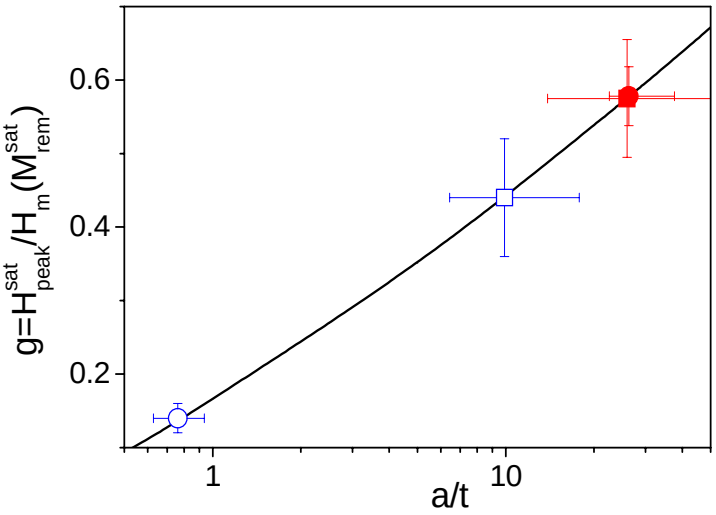

Fig. 5-10. Theoretical factor $g=H_{peak}^{sat}/H_m^{sat}$ as a function of the cylinder aspect ration a/t (continuous line) shown in Fig. 4-19. Superposed to the continuous line are the experimental g values for IBADt1.13$_{ORNL-B}$ (¹), IBADt1.33$_{ORNL-A}^{mill}$ (¸), RABt1.01$_{ORNL-B}$ (Ã)and RABt1.08$_{ORNL-A}$ (Â).

Additionally, we have also analyzed several RABiTS with different thickness and similar texture (÷λ3 6°-7°) grown with the processes A and B. Fig. 5-11 shows the average grain size obtained for the two IBAD samples discussed above together with the two sets of RABiTS samples studied as function of the thickness.

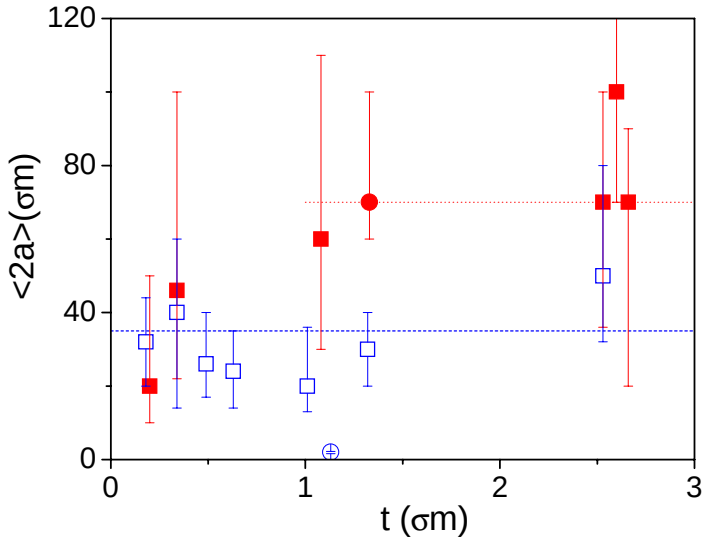

Fig. 5-11. Average grain size determined for several RABiTS samples with different thickness grown by process A (Â) and process B (Ã). Also shown is the grain size obtained for the IBAD samples IBADt1.33$_{ORNL-A}^{mill}$ (¸) and IBADt1.13$_{ORNL-B}$ (¹). Dashed line indicates the average grain size for the RABiTS samples grown with the process B and dotted line shows the average grain size correspondent to RABiTS samples, thicker than1σm, grown with process A.

Notice that the average grain size is about <2a>3 35σm (dashed line in the figure) for all the RABiTS samples grown with the optimized process (process B) which approximately coincides with that of the underneath textured layer. EBSD was used to

map out the grain size of YBCO and underlying NiW substrate for one of this samples (RABt0.49$_{ORNL-B}$) shown in Fig. 5-12b and Fig. 5-12a, respectively. Clearly observed is a direct replica of the substrate in the YBCO layer, with an average grain size similar to that detected by means of magnetic measurements. Fig. 5-12c presents an overlap of the YBCO GBs (red) onto the NiW substrate GBs (gray). All the YBCO grain boundaries correspond to those of the substrate.

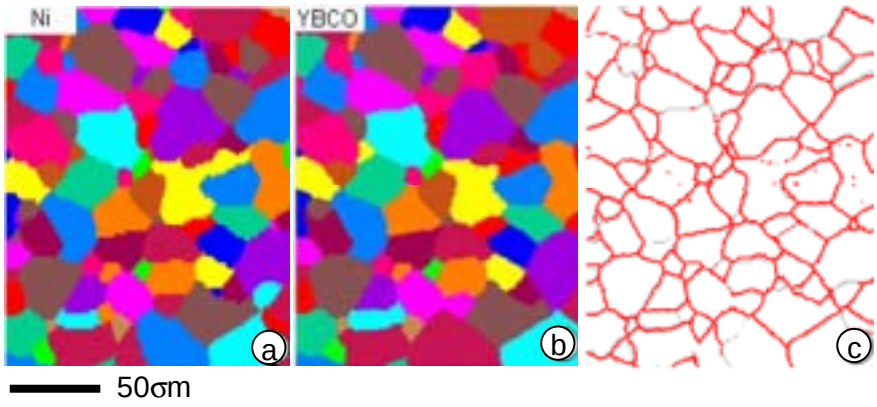

Fig. 5-12. EBSD data from a RABiTS sample, grown with a controlled liquid mediated process (RABt0.49$_{ORNL-B}$), without an excess of liquid formation. Grain maps are defined as in Fig. 5-7. Grain map of the NiW substrate (a), YBCO grain map in the same area scan as in the substrate (b) and grain boundary map showing all GBs ∅2^o for the data of (a) in gray and (b) in red (c).

For RABiTS samples grown with an uncontrolled process (process A), the grain size obtained is clearly larger (<2a>ℑ60σm) for samples thicker than1σm (dotted line in the figure) since, when the process is uncontrolled, the presence of a large amount of liquid is accentuated for thicker samples [85]. One of these thick samples (RABt2.60$_{ORNL-A}$) has also been analyzed by EBSD. Fig. 5-13b shows a grain map from YBCO layer of RABt2.60$_{ORNL-A}$ and Fig. 5-13a shows the underlying substrate. In this case, there is no immediate correlation between the grain maps in Fig. 5-13 a) and b). Fig. 5-13c is a overlay of YBCO GBs (red) onto the substrate GBs (gray). We clearly see the overgrowth of some of the substrate GBs by the YBCO grains, which comes out with a larger grain size, in agreement with that observed by magnetic measurements.

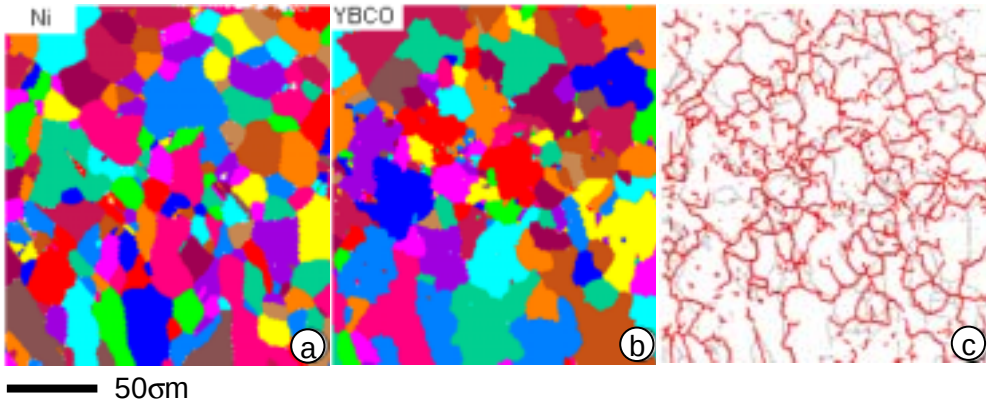

Fig. 5-13. EBSD data from a RABiTS sample, grown with an excess of liquid formation during the process (RABt2.60$_{ORNL-A}$). Grain maps are defined as in Fig. 5-7. Grain map of the NiW substrate (a), YBCO grain map in the same area scan as in the substrate (b) and grain boundary map showing all GBs ∅2^o for the data of (a) in gray and (b) in red (c)

Hence, we distinguish between two types of grains, those originated from an accurate controlled growth process which size are determined by the grain size of the underneath textured layer (grain size of about 2σm and 35σm for IBAD and RABiTS, respectively) and those generated in a growth process with an excess of liquid which produces grains in the order of 60-70σm in both IBAD and RABiTS substrates.

Now, we are interested in the correlation between the presence of these two types of grains and the critical current densities of YBCO CCs. Fig. 5-14 shows the values of grain and grain boundary critical current densities obtained for all the samples analyzed as a function of the thickness at 77K.

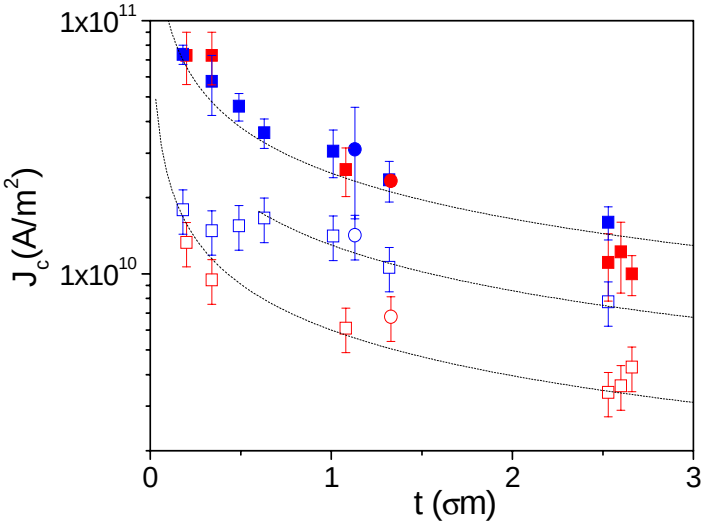

Fig. 5-14. Thickness dependence of J_c^G (closed symbols) and J_c^{GB} (open symbols) determined for several RABiTS samples grown by process A (red squares) and process B (blue squares). Also shown is the critical current obtained for the IBAD samples IBADt1.33$_{ORNL-A}^{mill}$ (red circle) and IBADt1.13$_{ORNL-B}$ (blue circle). Dashed lines are guides for the eyes.

Notice that, for all the samples analyzed, the values of $J_c^G(t)$ decreases with the sample thickness following the same curve, independently of the growth process, indicating that the superconducting properties of both types of grains are very similar. This suggests that the microstructure of the grains grown by an ex situ BaF_2 process, which sets their vortex pinning capabilities, is very similar in both cases.

In contrast, the values of $J_c^{GB}(t)$ do depend on the type of GB network. For YBCO GBs replicating the underneath GB substrate (in blue), the $J_c^{GB}(t)$ curve is clearly above the one obtained for the samples with YBCO GBs overgrowing the underneath GB substrate network (in red). These results indicate the better performance for current transport of the YBCO structure propagating from an already pre-existing network of dislocations in the substrate. We can then conclude that the origin of the decrease of the percolative J_c^{GB} of coated conductors which YBCO GB network does not replicate the substrate, must be assigned to the nature of these particular GBs and not to the pinning characteristics of the grains. In that, the decreasing of J_c^{GB} for the non-replicated GB networks could be associated to an observed degradation of the out-of-plane grain alignment as well as to the presence of precipitates which have been identified by TEM [82] and located at the GB. Fig. 5-15 shows how ÷ϖ in the YBCO (relative to the YSZ buffer) evolves as a function of thickness for several films grown by process A and B. Up to about 1σm, out of plane texture in the YBCO is slightly better than the substrate, but then for thicker films, the texture slightly gets worse for samples grown by process B and clearly much worse for samples grown by process A, in agreement with the smaller J_c^{GB}.

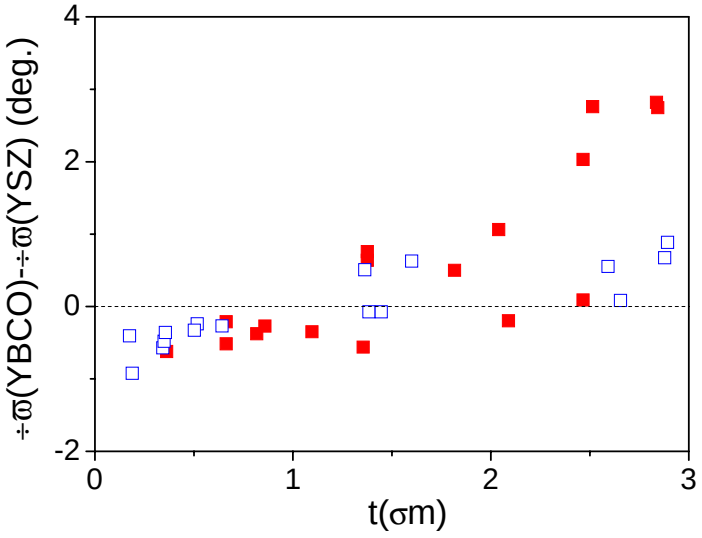

Fig. 5-15. Thickness dependence of the in plane texture in the YBCBO, relative to the YSZ buffer for different samples grown by process A (Â) and process B (Ã).

With this study, we have shown that the percolative current density, J_c^{GB}, of coated conductors is very much dependent on the actual conditions of the growth process used, i.e. ex-situ BaF_2 growth, and that special care has to be taken in this liquid mediated processes if one wants to grow CC above 1σm thickness. The percolative current density, J_c^{GB}, is maximized when the YBCO GB network replicates the underneath textured layer. We have shown that J_c^{GB} is very much depending on the nature of the YBCO grain-boundary microstructure induced by propagating the [100]-tilt dislocations of the textured substrate, while the actual substrate configuration and grain size is not. The grain critical current, J_C^G, is determined by the growth process technique (ex-situ BaF_2) which controls the vortex pinning capabilities for a given YBCO film thickness, but is not affected by the existence of GB network continuity throughout the full conductor.

5.2 INFLUENCE OF THE YBCO LAYER TEXTURE

As it has been described previously in section 1.4 the principal limitation of the percolative critical current density in YBCO coated conductors, J_c^{GB}, is the presence of grain boundaries. So that, a high biaxial textured YBCO layer is required in order to obtain high J_c conductors.

The GB critical current density of several coated conductors with different texture has been determined by using equation 4-12 (i.e. $J_c^{GB}=3M_{peak}^{sat}/R$). Additionally YBCO thin films grown on single crystalline substrates have also been included for comparison proposes. In Fig. 5-16 we show the values of J_c^{GB} obtained for several samples as a function of the measured FWHM phi-scan, $\div\lambda$ (see section 2.2.3). Although there exists a certain scattering due to the fact that these samples have very different thickness (from 0.2σm to 3σm), substrate (IBAD and RABiTS) and growth process (PLD and BaF_2), the exponential dependence of $J_c^{GB}(\lambda)$ described in section 1.4.1 has been observed. For instance, the IBAD sample which presents a J_c^{GB} above the exponential fitting line, is thinner (t=0.23σm) than the other three IBAD samples presented (t≥1σm), which clearly follows the fitting line. As we will see in next section, J_c decreases with the YBCO thickness. Samples with J_c^{GB} bellow the fitting line correspond to thicker samples or samples with damaged grain boundaries. Overall, the derived $J_c^{GB}(\lambda)$ dependence indicates that grain boundaries are the most significant factor limiting J_c^{GB} values in coated conductors.

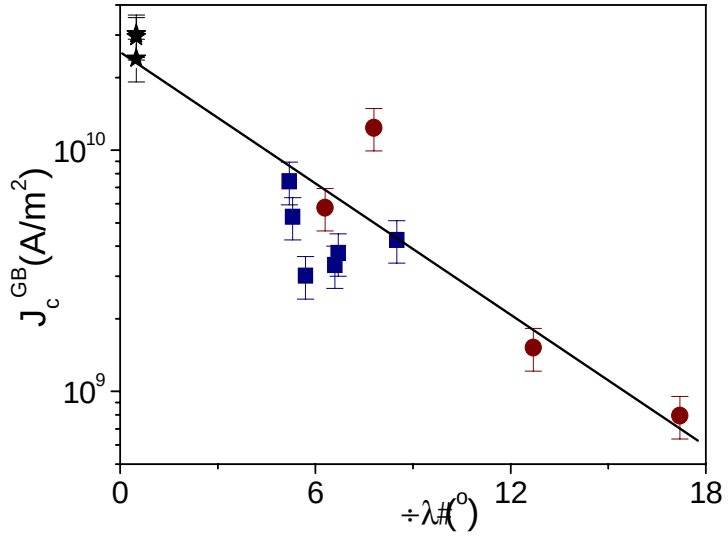

Fig. 5-16. J_c^{GB} as a function of the FWHM of the X-ray phi-scan, ÷λ, for several RABiTS (y) and IBAD (ŏ) samples analyzed. Also presented are some values of J_c obtained for thin films grown on single crystals.(Ċ)

With the aim of studying the effect of the texture in both J_c^{GB} and J_c^G, two samples with similar thickness, t, grown by PLD at the same conditions on IBAD substrates with very different texture have been analyzed. $IBADt1_{Gott}$ with ÷λ=6.5°, t=1σm and $IBADt1.6b_{Gott}$ with ÷λ=17.2°, t=1.6σm. Samples have been supplied by the "Zentrum für FunktionWekstoffe" in Göttingen (Germany).

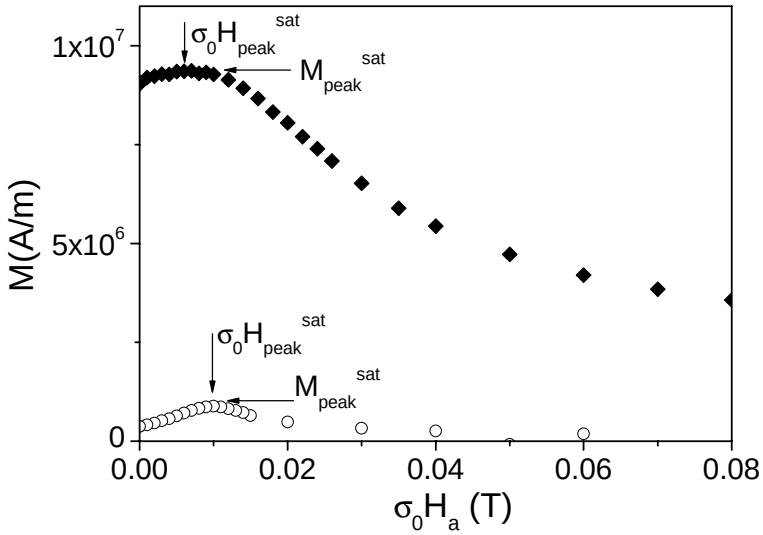

Fig. 5-17. Reverse branches of several hysteresis loops measured at 77K with $\sigma_0 H_m$=0.02T, 0.04T and 0.1T, for $IBADt1_{Gott}$ (ß) and $IBADt1.6b_{Gott}$ (¹).

Fig. 5-17 shows the saturated reverse branches of hysteresis loops measured for the two samples. Notice that both curves present a peak of magnetization at a similar position, although the magnetization is more than one order of magnitude smaller for the sample with worse texture. By determining the ratio $H_{peak}^{sat}/H_m(M_{peak}^{sat})$

and using equation 4-10, we have obtained the average magnetic grain size for both samples, being <2a>=2.5σm and 3σm for IBADt1$_{Gott}$ and IBADt1.6b$_{Gott}$, respectively. As we have already seen in section 2.2.3, the expected structural grain size for a standard IBAD coated conductor is between 1-5σm, which agrees with the values that we have obtained.

Once we have determined the average grain size, the grain critical current density can be calculated by using equation 4-7 ($J_c^G \Im H_{peak}^{sat}/xt$). Since we have found similar values of $\sigma_0 H_{peak}^{sat}$ the calculated curves $J_c^G(T)$ are very similar for both samples (closed symbols in Fig. 5-18). The corresponding values of $J_c^{GB}(T)$ have been determined by using equation 4-12 ($J_c^{GB}=3M_{peak}^{sat}/R$). In this case, since the magnetization is much smaller for the sample IBADt1.6b$_{Gott}$, the values of $J_c^{GB}(T)$ obtained for this sample are about one order of magnitude smaller than that obtained for the sample IBADt1$_{Gott}$ (open symbols in Fig. 5-18). Moreover, the values of $J_c^{GB}(T)$ obtained for both samples are smaller than $J_c^G(T)$. The difference between J_c^G and J_c^{GB} arises from the reduction in the effective grain boundary cross section by the dislocation cores (see section 1.4.1). This reduction is bigger as higher is the misorientation angle, i.e. for samples with worse texture.

We can conclude then, that the pinning of AV inside the grains does not depend on the texture of the YBCO layer whereas the pinning of the AJV in the grain boundaries clearly depends on the misorientation between grains. The core length of AJV in the grain boundaries increases as J_c^{GB}/J_c^G decreases, so that, a larger core of AJV leads a weaker pinning along the GB (see section 1.4.1).

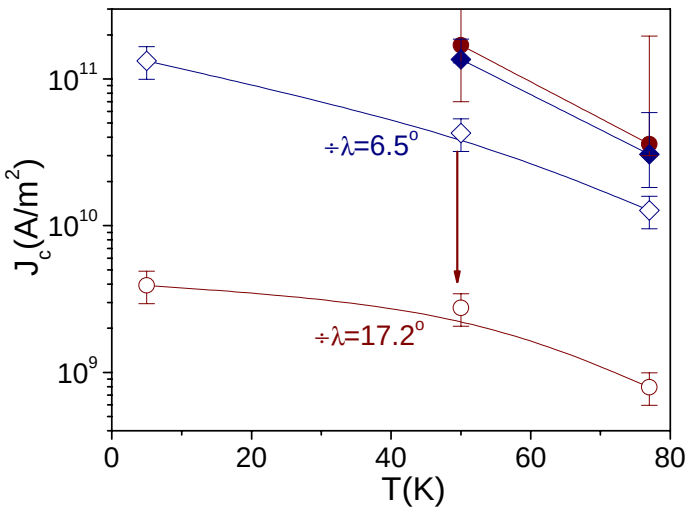

Fig. 5-18. Temperature dependence of J_c^{GB} (open symbols) and J_c^G (closed symbols) for IBADt1$_{Gott}$ (↓) and IBADt1.6b$_{Gott}$ (⇙).

Therefore we can conclude that the main J_c limiting mechanism for transport critical current in coated conductors is indeed determined by the GB angles. So that, one require misorientation angles less than 4^o in order to avoid the region of exponential decrease of J_c^{GB} with the GB misorientation angle (see section 1.4.1).

5.3 VORTEX PINNING MECHANISMS IN YBCO COATED CONDUCTORS

We have seen that the critical current density of YBCO coated conductors is strongly affected by the existence of grain boundaries and thus J_c^{GB} is limited by the texture of the sample. This situation, however, is modified when we deal with highly textured coated conductors ($\div\lambda<5^o$-7^o), i.e. with misorientations of the GB network low enough to reduce the effect of the grain boundaries and allow J_c^{GB} to be influenced by J_c^G. Although Abrikosov vortices are clearly governing the vortex pinning properties of the grains and thus governing J_c^G, the physical mechanisms associated to the critical currents of the grain boundary network is somewhat more complicated. With the new methodology we have developed, we can determine J_c^{GB} and J_c^G of the same coated conductor independently, and thus sort out the relationship existing between AJV associated to the grain-boundaries and AV at the grains.

We have studied the relation between the critical currents in several samples with similar texture but different thickness in order to determine the origin of J_c^{GB} dependence with the thickness of the YBCO layer. Additionally we have analyzed the dependences of the critical current density with the magnetic field in YBCO thin films grown on single crystals and YBCO coated conductors in order to investigate the pinning mechanisms in both cases.

5.3.1 CORRELATION OF J_c^G AND J_c^{GB} WITH THE THICKNESS OF THE YBCO LAYER

YBCO coated conductors have emerged as a promising material for superconducting power applications. To meet the technical requirements of these applications, CCs need to deliver large critical current, I_c, values. An obvious approach to improve I_c is to increase the thickness, t, of the superconducting layer, but it has been observed by transport measurements [87] that the percolative critical current density, J_c^{GB}, decrease with increasing the film thickness. Fig. 5-19 shows the transport critical current density determined for several YBCO IBAD coated conductors of different thickness where a clear decreasing of the critical current density with the thickness is observed. The cause of the decrease of J_c with YBCO thickness still

remains unclear and thus the study of this issue is particularly interesting for the development of coated conductors.

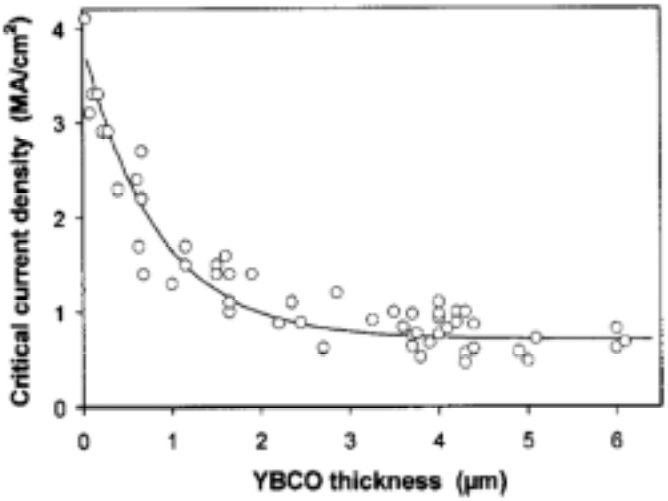

Fig. 5-19. Transport critical current density as a function of the thickness measured at 77K for several YBCO on IBAD YSZ coated conductors [87].

For this study we have analyzed several RABiTS coated conductors grown by ex situ conversion of BaF_2 based precursors on RABiTS substrates with the same texture (÷λℑ6°-7°) but with different YBCO thickness.

Fig. 5-20 shows the average magnetic grain size determined with equation 4-10, as a function of the sample thickness. We have obtained a similar grain size for all the coated conductors analyzed, <2a>ℑ35σm, as it is expected since all the samples have been grown on the same substrate. All these samples have been grown with an optimized process (process B in section 5.1.1) where the YBCO grain boundaries replicates the substrate GB network.

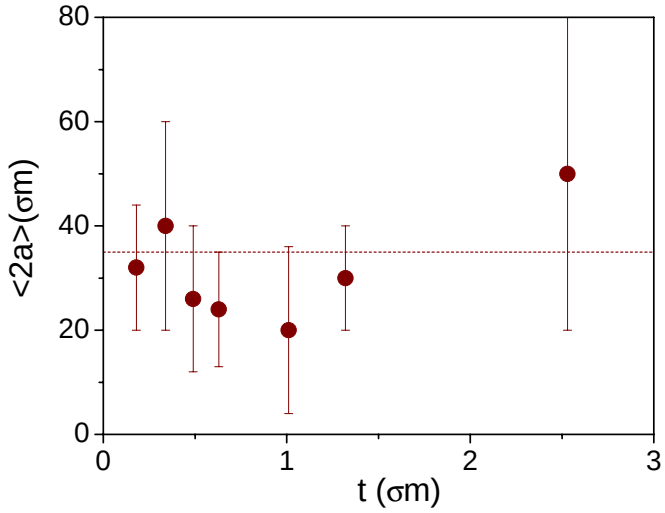

Fig. 5-20. Average grain size determined for several RABiTS samples grown by ex situ conversion of BaF_2 based precursors with different thickness.

Results of $J_c^G(t)$ and $J_c^{GB}(t)$ calculated at 77K and at about zero magnetic field by means of equation 4-7 and 4-12, respectively, are presented in Fig. 5-21. We have also included the correspondent values of the transport critical current density, for all the coated conductors, which clearly agree with the J_c^{GB} determined by means of magnetic measurements.

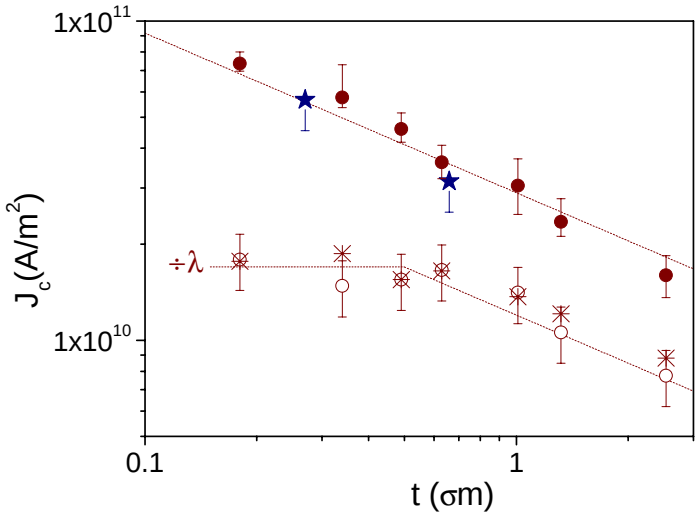

Fig. 5-21. Thickness dependence of J_c^G (¸) and J_c^{GB} (¹) determined for several RABiTS coated conductors at 77K by magnetic measurements and the correspondent transport critical current density (ü). Also shown the J_c values of two thin films grown on single crystals with the same buffer architecture as the RABiTS CCs (CeO_2/YSZ/Y_2O_3) (Ċ). Dashed lines are guides for the eyes.

Notice that, not only J_c^{GB} decrease while increasing the thickness of the YBCO layer, t, but also J_c^G decreases with t. Hence, we clearly observe a correlation between the two critical current densities. In fact, $J_c^{GB}(t)$ can be adjusted with the same power law as $J_c^G(t)$, for samples with t>0.5σm, although at low thickness the limitation of the texture (÷λ3$6^o$-7^o) seems to govern the maximum of J_c^{GB} and the value $J_c^{GB}(t)$ remains constant at J_c^{GB}3$2.10^{10}$A/m^2.

The observed correlation between J_c^G and J_c^{GB} can be understood if we consider an interaction of the AV pinned inside the grains with the AJV pinned at the grain-boundaries. Then the strong pinned AV located beside the grain boundaries could hold AJV and thus, by increasing the pinning force within the grains, the unpinning of AJV at the grain boundaries would also be much difficult (see Fig. 5-22). In this situation we will have a higher J_c^{GB} for the thinner coated conductors (where we have obtained higher J_c^G) although all the samples have the same texture. We propose then that J_c^{GB} at large thickness may be improved by enhancing grain vortex pinning capabilities at these thickness.

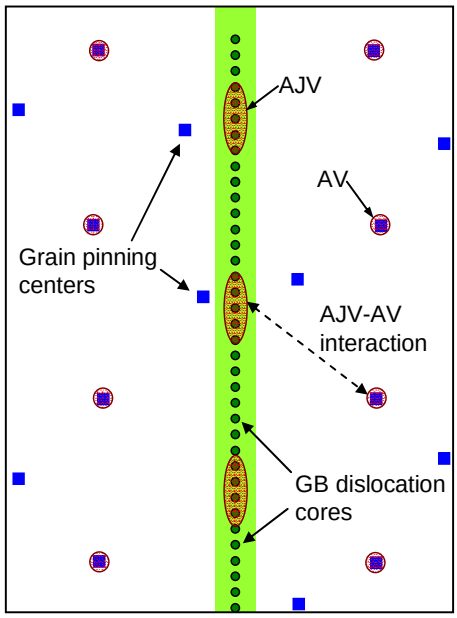

Fig. 5-22. Schematic representation of vortex configuration in a coated conductor. There exists a magnetic interaction between the AJV pinned at the GB dislocations and AV pinned at the grain pinning centres.

The observed decrease of $J_c^G(t)$ can be explained if the density of pinning centres in the grains will not stay constant through the whole thickness, i.e. not all the defects induced at the interface between the YBCO layer are effective at the YBCO top layer. However, this argument cannot explain the decrease of $J_c^{GB}(t)$ since in this case the GB dislocations formed due to the grain misorientation, go well through the sample. Comparing the values of $J_c^G(t)$ with the ones obtained for two YBCO thin films of different thicknesses, grown by the same technique on single crystals buffered with the same multilayer structure (also presented in Fig. 5-21), we observe that the values follow the same $J_c(t)$ curve indicating that the pinning achieved within the grains of the coated conductor is as good as the one obtained in a film grown on a single crystal of the same thickness.

It has been observed that by means of an improvement in the ex situ conversion of BaF_2 process, it is possible to increase the transport critical current density of coated conductors, although no changes in the values of ÷λ have been detected for these particular samples [88]. We have analyzed a set of samples grown by this process (process C) on RABiTS substrates with the same texture (÷λ6°-7°) as the samples previously analyzed (grown by process B). We want to see if, in this case, we also find that the increase of J_c^{GB} would correlate with an increasing of J_c^G. Fig. 5-23 shows the values of $J_c^G(t)$ and $J_c^{GB}(t)$ that we have obtained for the samples grown by process C, in comparison with the results obtained for samples grown by process B. We observe that the values of $J_c^{GB}(t)$ are higher for the samples grown by

the improved process, in agreement with a higher transport critical current previously observed, but in this case we do not observe an improvement of $J_c^G(t)$.

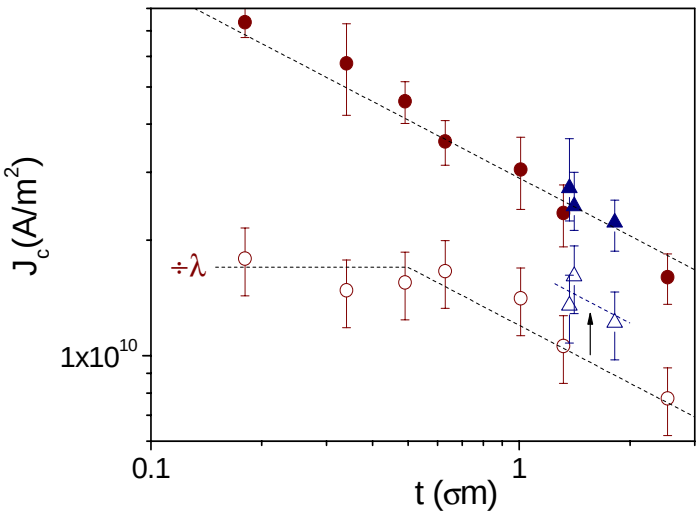

Fig. 5-23. Thickness dependence of J_c^G (closed symbols) and J_c^{GB} (open symbols) determined for several RABiTS coated conductors at 77K grown by process B (¸) and C (¡). Dashed lines are guides for the eyes.

Further analysis on the microstructure of these particular samples has evidenced that, with the improved process (process C), grains grow forming meanders at the grain boundaries (observed by EBSD and TEM). Fig. 5-24 shows the grain boundary maps obtained for a 0.8 σm sample grown by this improved process. Grain boundary colours means different misorientation angles. Fig. 5-24a shows the map obtained for the YSZ substrate and Fig. 5-24b corresponds to the YBCO layer. Notice that the substrate grain structure is recognizable in the YBCO layer, i.e. YBCO grains replicates the substrate GB network, although GBs meander. Fig. 5-25 shows the meandering effect between two grains, in detail. These data has been acquired at the University of Wisconsin (UW) by Matt Feldmann [89].

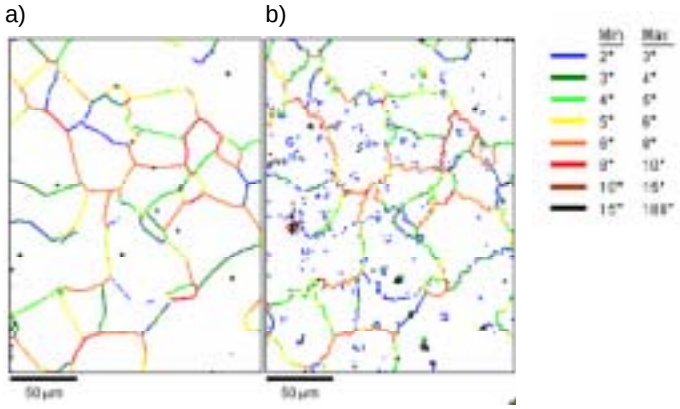

Fig. 5-24. Grain boundary map obtained for a RABiTS coated conductor grown by BaF_2 with process C. Fig. 5-24a) shows the GBs measured in the YSZ substrate and Fig. 5-24b) the YBCO GBs in the same area scan.

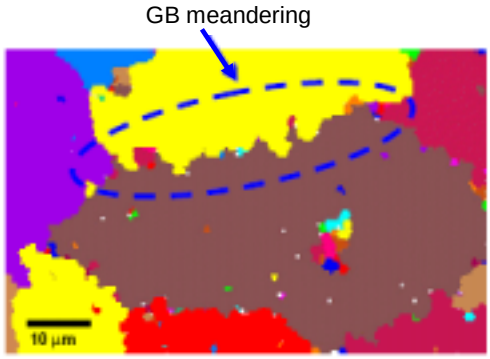

Fig. 5-25. EBSD grain map obtained for the same sample described Fig. 5-24 where a detail of GB meandering can be appreciated.

Meandering in the YBCO grain boundaries has also been observed by TEM. Fig. 5-26 shows a TEM image of a RABiTS sample with t=1.25σm, grown by BaF_2 with process C, where meandering through the thickness can be identified [90]. TEM analysis has been performed by T. Holesinger at LANL.

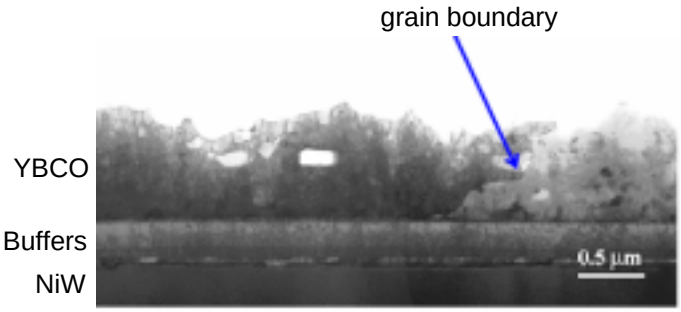

Fig. 5-26. Cross sectional TEM image of a 1.25σm RABiTS sample grown by BaF_2 with process C, showing GB meandering through the thickness.

The effect of GB meandering in the J_c^{GB} has been studied by means of transport measurements in thin film bycristals by Feldmann et al. [89]. They patterned transport paths, in YBCO thin films grown by PLD on 5° STO bicrystal substrates, forming different angles with the bicrystal GB (Fig. 5-27)

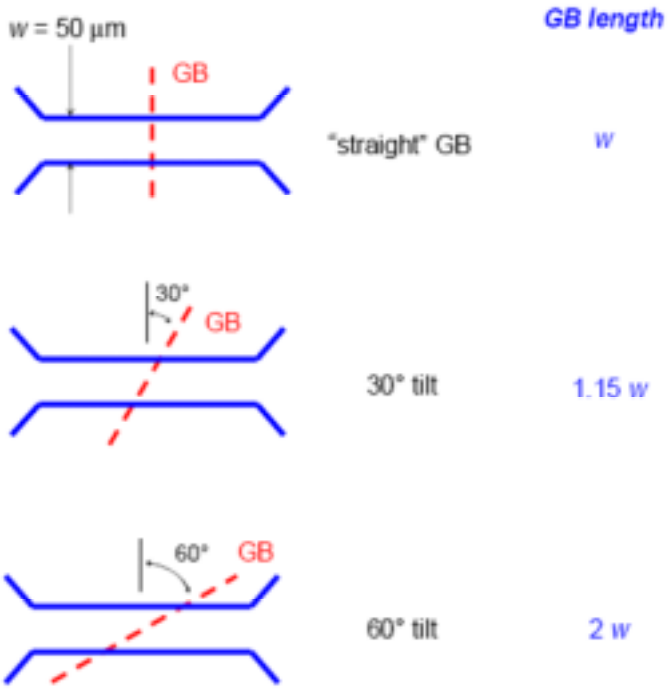

Fig. 5-27. Schematic representation of tree transport paths trough a GB forming different angles with the GB line.

When the angle between the GB and the section path increases, the effective GB length through the current path also increases as $l_{GB}=w/\cos(\chi)$, where l_{GB} is the GB length, χ the tilted angle and w is the with of the path. By increasing the total area of the grain boundary we are increasing the total section where supercurrent can flow and thus we are increasing J_c^{GB}. Fig. 5-28 shows the transport critical current density measured for a straight GB and for GBs tilted 30^o and 60^o [89], where we can observe that increasing the tilting angle the transport critical current through the GB certainly increases. This effect also occurs in coated conductors with GB meandering since due to the GB meanders there are a lot of tilted GBs in the current path. Therefore, we conclude that the improvement in the growing conditions (process C) does not change the pinning capabilities of the grains, i.e. does not change J_c^G, but modifies in fact the effective grain boundary cross section and thus increases J_c^{GB}. Notice that the critical current density obtained for the bicrystals merge with the one measured for the single crystal at a certain field which will be commented in section 5.3.2.c.

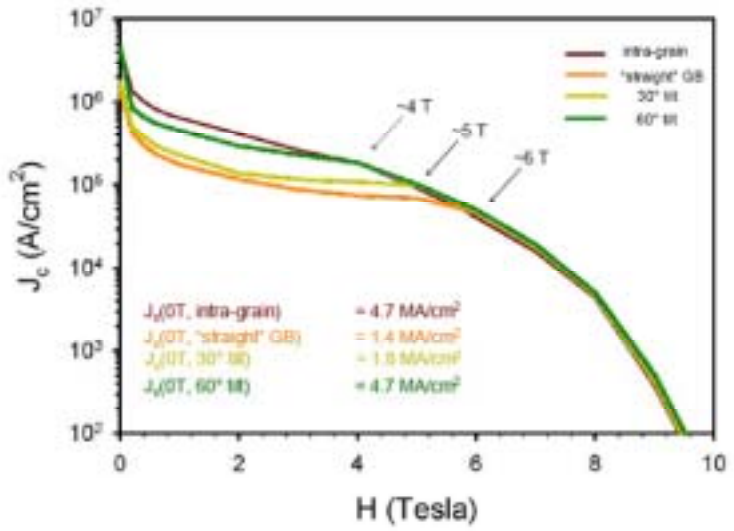

Fig. 5-28. Magnetic field dependence of transport critical current for a YBCO thin film grown by PLD on a 5° STO bicrystal [89]. Different curves show the values of the critical current measured inside the grains and through the grain boundary, where different tilted paths have been patterned (see Fig. 5-27).

In order to better understand the correlation existing between J_c^G and J_c^{GB}, we have represented the values of J_c^{GB} as a function of J_c^G, for all the samples grown by the BaF_2 process on RABiTS and IBAD substrates with similar texture, ÷λℑ6°-7° that we have analyzed. We have included samples grown by process A and B, described in section 5.1.1, and samples grown by process C, described in this section. Results are shown in Fig. 5-29.

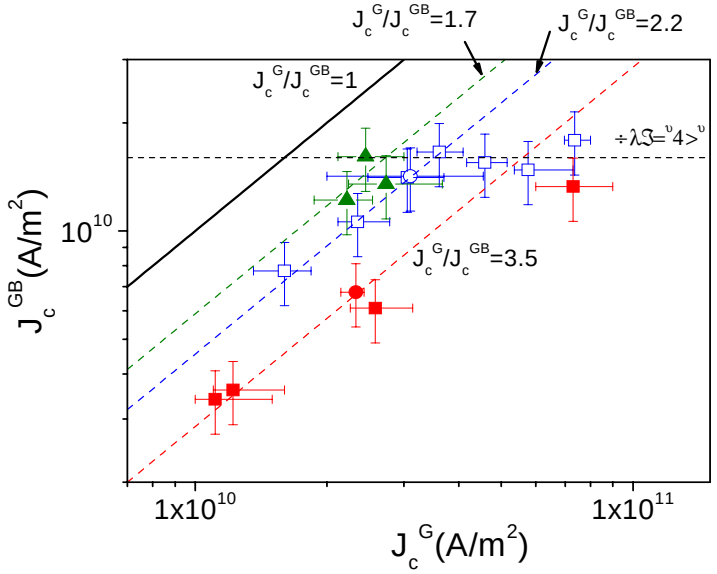

Fig. 5-29. J_c^{GB} as a function of J_c^G obtained for several samples grown by BaF_2 on RABiTS and IBAD substrates of similar texture, ÷λℑ6°-7°. Different symbols correspond to, RABiTS samples grown by process A (Â), IBAD samples grown by process A (¸), RABiTS samples grown by process B (Ã), IBAD samples grown by process B (¹) and RABiTS samples grown by process C (¡). Solid line corresponds to the curve J_c^G/J_c^{GB}=1 and dashed lines represent different ratios J_c^G/J_c^{GB}. The maximum value of J_c^{GB} marks the texture limitation (dotted line).

As it has been discussed above, we clearly observe a correlation between J_c^G and J_c^{GB}. Hence, by increasing J_c^G, J_c^{GB} also increases. Additionally we have found that, for samples grown by BaF_2, it is possible to increase J_c^{GB}, without changing J_c^G, approaching the curve $J_c^G/J_c^{GB}=1$ (solid line in the figure) by optimizing the growing process. For samples grown by process A, where an excess of liquid is induced during the growth, we have obtained $J_c^G/J_c^{GB}=3.5$. For samples grown by an improved process (process B) with a controlled amount of liquid, we obtain $J_c^G/J_c^{GB}=2.2$. And finally, for samples grown by a better optimized process (process C), which induces GB meandering, we have obtained the ratio, $J_c^G/J_c^{GB}=1.7$. The different ratios J_c^G/J_c^{GB} have been indicated as dashed lines in Fig. 5-29. However, we observe that increasing J_c^G, J_c^{GB} also increases following the dashed lines until it reach a saturation value, $J_c^{GB}\Im 1.6.10^{10}A/m^2$. Hence, we observe that the YBCO texture limits the maximum J_c^{GB} that can be reached in the sample (dotted line in the figure).

Fig. 5-30 shows the values J_c^{GB} vs. J_c^G obtained for two IBAD samples with very different texture grown by PLD, analyzed in section 5.2. Although both samples present similar values of J_c^G, in this case, J_c^{GB} is clearly limited by the texture (dotted lines in the figure)

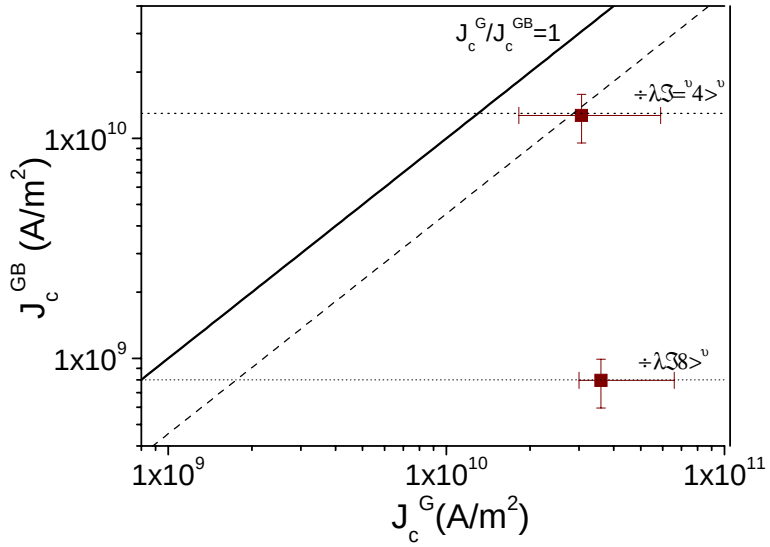

Fig. 5-30. J_c^{GB} as a function of J_c^G obtained for two IBAD samples grown by PLD on substrates with different texture. Solid line corresponds to the curve $J_c^G/J_c^{GB}=1$ and dashed line to $J_c^G/J_c^{GB}=2.2$. Texture limitation is represented by dotted lines.

We can conclude then, that J_c^{GB} is clearly influenced by J_c^G, and that increasing the pinning capabilities of the grains we can improve J_c^{GB}. However, we have also observed that it is possible to increase the percolative critical current density, J_c^{GB}, by changing the nature or the effective length of the grain boundaries without changing J_c^G, i.e. without modifying pining inside the grains.

5.3.2 FIELD DEPENDENCE OF J_C^G AND J_C^{GB}

In order to further study the vortex pinning capabilities in YBCO thin films and coated conductors we have analyzed the dependence of the critical current density with the magnetic field, $J_c(H)$, for both systems. This analysis will allow us to study the relationship between $J_c^G(H)$, determined for a YBCO thin film, and $J_c^{GB}(H)$, determined for a YBCO coated conductor, and understand the different pinning regimes appearing for the Abrikosov vortices inside the grains, and for the Abrikosov-Josephson vortices in the GBs.

5.3.2.a VORTEX PINNING BY NATURAL LINEAR DEFECTS IN YBCO THIN FILMS GROWN ON SINGLE CRYSTALS

In clean YBCO single crystals the pinning and dynamics of vortices may be described by the theory of weak collective pinning [6]. A single vortex is pinned by many point pinning centres that are randomly distributed and has a random pinning force. The vortex tries to increase its pinning energy by taking advantage of as many pinning centres as possible, and secondly a vortex wants to remain straight in order to minimize its elastic energy. As a result of this competition between pinning and elastic energy, the vortex breaks up in elastically correlated pieces of length L_c, the correlation length. This picture works very well in describing the situation in clean single crystals of high-T_c superconductors, but it is not appropriate for strong pinning centres observed in HTS thin films or irradiated single crystals [91]. In the case of strong pinning, vortices are pinned over their full length by an extended defect, which locally suppresses the superconducting order parameter. The Bose glass theory [7] has successfully described the strong pinning results of irradiated single crystals or YBCO thin films with intrinsic linear defects [92-95].

The irradiation of single crystals or films with heavy ions creates amorphous ion tracks where the crystal structure is heavily distorted, causing a suppression of the superconducting order parameter. Also the core of a dislocation in thin films is characterized by a strong deformation of the crystal lattice and a corresponding suppression of the order parameter. The starting point in the Bose glass theory is that at low magnetic fields a single vortex is strongly pinned by a linear (columnar) defect. The vortices can freely accommodate to the pinning sites until the shear energy exceeds the pinning energy per unit length, U_p. Then the crossover to a collective pinning regime occurs at the crossover or accommodation field [7,92].

$$\mu_0 H_{cross} \; - 4(U_p / U_0) B_A \qquad 5\text{-}1$$

where $U_0=A_0^2/4\phi\sigma_0\varsigma^2$ is the characteristic vortex energy per unit length, A_0 is the flux quantum and $B_A=n_{lin}A_0$ is the matching field, at which the vortex density exactly equals the defect density, n_{lin}.

Experimentally, the matching field B_A can be determined unambiguously from the irradiation dose or, in the case of dislocation pinning in thin films, by counting the number of etchpits [93,96]. The accommodation field is determined by the interaction between the vortex lattice and the pinning defects. For $\sigma_0 H << B_A$ there are many available defects per vortex. In this limit each vortex is localized in one track forming a Bose-glass phase [6,7]. To find a track, a vortex must typically displace from its equilibrium position by a distance comparable to the mean separation between defects, $d_0=(A_0/B_A)^{1/2}$. As field increases, the flux line lattice parameter $a_0=(A_0/B)^{1/2}$ decreases. When d_0 becomes a significant fraction of a_0 the elastic energy cost of the lattice distortion turns relevant and the net energy that the vortex gains by sitting on the track is lower. This situation basically occurs when all the pinning centres are occupied with a vortex. In fact, it has been observed that for YBCO thin films at 5K $\sigma_0 H_{cross}/B_A \Im 0.7$ [94].

The accommodation field, $\sigma_0 H_{cross}(T)$ marks a crossover from strong individual vortex pinning (where vortex-vortex interactions are much weak than interactions between vortex and pinning centres) to a collective pinning regime where vortex-vortex interaction plays a major role. In general, it marks the end of a plateau in the critical current density [92].

At low magnetic fields $\sigma_0 H < \sigma_0 H_{cross}$, we can consider that all the vortices can be pinned in linear defects and thus the critical current density is given by equating the Lorentz force with the pinning force, i.e.

$$J_c B - n f_p \qquad 5\text{-}2$$

Where f_p is the pinning force per unit length, $f_p=U_p/\bullet_{ab}$, (which can be considered independent of the magnetic field), $\bullet_{ab}$ is the in-plane coherence length and n is the planar distribution of pinned vortices, $n=1/a_0^2$. Then by using $a_0=(A_0/B)^{1/2}$, one obtains a J_c independent of B.

$$J_c - \frac{f_p}{A_0} \qquad 5\text{-}3$$

At higher magnetic fields $\sigma_0 H > \sigma_0 H_{cross}$ only a small fraction of vortices are within linear defects and hence directly pinned. The other vortices are kept at their position by the elastic interactions with these strongly pinned vortices. Two mechanisms of vortex pinning are possible in this regime. The collective pinning is related to the pinning of vortex bundles with transverse size R_c, given by,

$$R_c - d_0 \frac{\varepsilon_{ab}^3}{a_0 c_o^2} \qquad 5\text{-}4$$

where c_0 is the radius of the cylindrical pinning energy well. This regime is important when $R_c > d_0$. The critical current is defined by the valance between the Lorentz force exerted on the bundle and the shear deformation energy necessary to shift the bundle to the next metastable state.

$$J_c B R_c^2 \varepsilon_{ab} - c_{66} \varepsilon_{ab}^2 \qquad 5\text{-}5$$

Where c_{66} is the shear modulus given by,

$$c_{66} \mid \frac{A_0 B}{16' \mu_0 \lambda_{ab}^2} \qquad 5\text{-}6$$

where ς_{ab} is the in-plane penetration depth. Using equation 5-4 for the correlation radius, one obtains.

$$J_c(B) \mid \frac{A_0 c_0^4}{16' \mu_0 \lambda_{ab}^2 \varepsilon_{ab}^5} \frac{B_A}{B} \qquad 5\text{-}7$$

Another proposed mechanism is the so called plastic pinning, which becomes relevant, when $R_c << d_0$. In this case vortices which are locked between these pinned islands of size R_c will move under sufficient current before depinning of the vortices trapped by the linear defects take place. The corresponding critical current density is given by the balance between the elastic and Lorentz forces in the area d_0^2.

$$J_c B d_0^2 a_0 - c_{66} a_0^2 \qquad 5\text{-}8$$

which results,

$$J_c(B) - \frac{\sqrt{A_0}}{16' \mu_0 \lambda_{ab}^2} \frac{B_A}{\sqrt{B}} \qquad 5\text{-}9$$

It has been observed that collective pinning is important when d_0 is small, i.e. when there are many vortex in the material, whereas in a more dilute linear defect system, vortices are plastically pinned [94]. In irradiated single crystals, where a lot of defects are induced, collective pinning has been detected [97].

5.3.2.b $J_c(H)$ ANALYSIS OF YBCO THIN FILMS GROWN ON SINGLE CRYSTALS

We have analyzed the magnetic field dependence of the critical current of several YBCO thin films deposited by different techniques on single crystalline substrates. Two YBCO thin films deposited by ex situ conversion of BaF_2 based precursors, $SCt0.27_{ORNL-A}$ and $SCt0.66_{ORNL-A}$, with thickness, t=0.27σm and t=0.66σm, respectively, and two more films deposited by PLD, $SCt0.2_{Dres}$, with t=0.2σm and $SCt0.25_{Gott}$ with t=0.25σm. These last two samples have been grown at different laboratories. For all the films analyzed we have found that J_c exhibits a plateau for magnetic fields $\sigma_0 H < \sigma_0 H_{cross}$ as it is expected according to equation 5-3. Above $\sigma_0 H_{cross}$, a gradual transition to a power-law behaviour, i.e. $J_c(H) \nabla H^{-\zeta}$, is found. Fig. 5-31 shows the magnetic field dependence obtained for the film $SCt0.66_{ORNL-A}$ at 5K, 50K and 77K. The arrows indicate the accommodation field, $\sigma_0 H_{cross}$, which have been determined by the crossing of the power law fit and the low field plateau. When the magnetic field approaches the irreversibility field the critical current decrease very fast with the magnetic field and does not follow the power law fit anymore (dotted lines in Fig. 5-31). This does not necessarily mean that there is a crossover to another pinning mechanism. Some authors [94], have been ascribed it to the fact that the relaxation in this region becomes so strong that J_c is strongly affected by flux creep and a determination of J_c is very difficult since depends a lot on the measuring technique (SQUID magnetometry, ac-susceptibility).

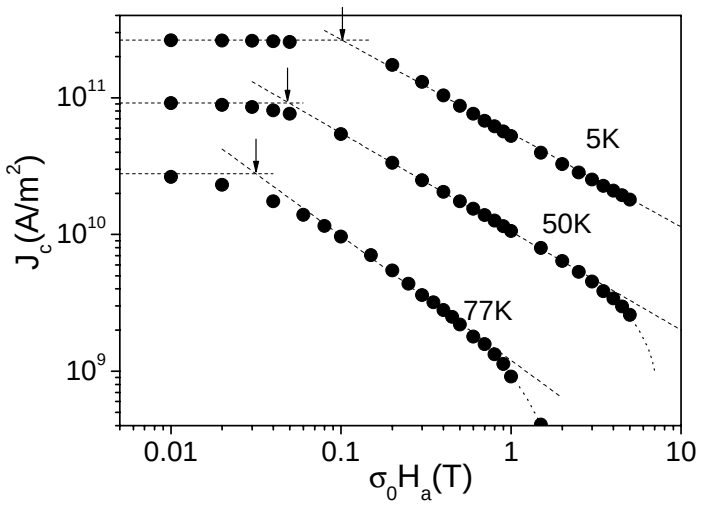

Fig. 5-31. Magnetic field dependence of the critical current density of the film $SCt0.66_{ORNL-A}$ at various temperatures. The arrows indicate the accommodation field $\sigma_0 H_{cross}$ determined at each temperature.

From Fig. 5-31 one observes that the value of $\sigma_0 H_{cross}$ decreases as the temperature increases, due the temperature dependence of U_p/U_0. For all the films

analyzed we have obtained similar values of $\sigma_0 H_{cross}(T)$, within the range of 0.1T-0.15T at 5K, 0.02T-0.07T at 50K and 0.01T-0.04T at 77K, as it is shown in Fig. 5-32, indicating that they have similar dislocation densities (see equation 5-1). We have presented in Table 5-1 the dislocation spacing determined at 5K, for two single crystals with $\sigma_0 H_{cross}$=0.12T and 0.15T being 129nm and 113nm, respectively.

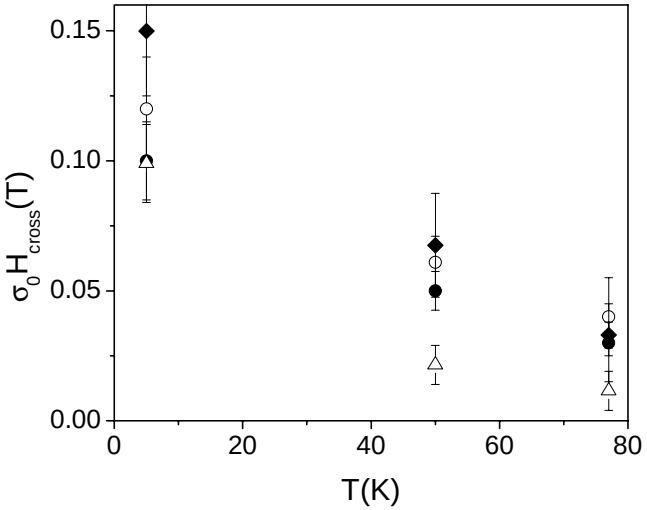

Fig. 5-32. Temperature dependence of the accommodation field, $\sigma_0 H_{cross}(T)$, for the films $SCt0.27_{ORNL\text{-}A}$ (¹), $SCt0.66_{ORNL\text{-}A}$ (¸), $SCt0.2_{Dres}$ (r) and $SCt0.25_{Gott}$ (ß).

The other parameter that we can determine with the curves $J_c(H)$ is the exponent ζ of the power law fit, $J_c(H) \nabla H^{-\zeta}$, for $\sigma_0 H > \sigma_0 H_{cross}$. Fig. 5-33 shows the values of $\zeta(T)$ obtained for all the films analyzed. Notice that in general $\zeta(T)$ increases with temperature, being almost 1 at 77K for al the samples. At low temperatures (T<50K) $\zeta(T)$ approaches to $\zeta \Im 0.5$ for the two films grown by PLD while for the films grown by ex situ BaF_2 precursors $\zeta \Im 0.7$.

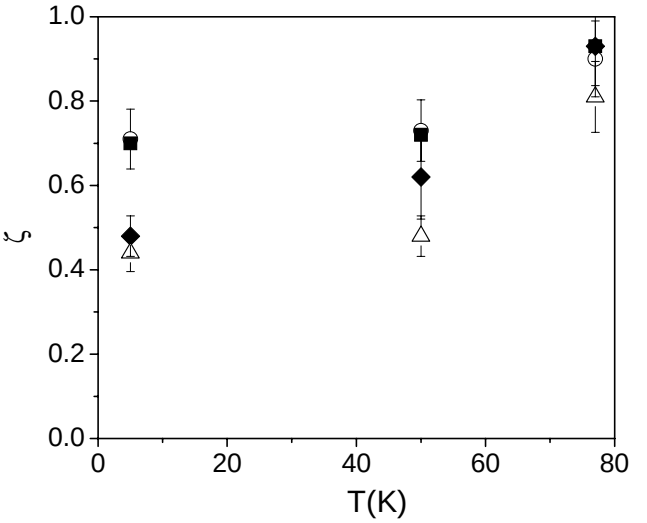

Fig. 5-33. Exponents ζ for the power law fit, $J_c(H) \nabla H^{-\zeta}$, at high magnetic fields for the films $SCt0.27_{ORNL\text{-}A}$ (¹), $SCt0.66_{ORNL\text{-}A}$ (¸), $SCt0.2_{Dres}$ (r) and $SCt0.25_{Gott}$ (ß).

The $J_c \nabla 1/H$ dependence found at 77K is the typical behaviour for a collective pinning regime (see equation 5-7). At low temperatures, the values of $\zeta \Im 0.5$ obtained for the two samples grown by PLD, indicate a shear pinning regime (equation5-9) while in general for $0.5<\zeta<1$ the vortex pinning mechanism is rather more complicated possibly due to a combination between collective and shear pinning, which depends on the temperature. The reason to change from one mechanism to the other is not clear and needs further investigation. Nevertheless, since the bundle size depends on the temperature, being smaller at lower temperatures [7,98] it is expected a plastic regime at low temperatures.

5.3.2.c $J_c(H)$ ANALYSIS OF YBCO IBAD AND RABiTS COATED CONDUCTORS

The same analysis has been performed to several IBAD and RABiTS coated conductors grown by both ex situ conversion of BaF_2 precursors and by PLD. For coated conductors the local magnetic field at the grain boundaries has the contribution of the return field coming from the grains, i.e. $\sigma_0 H_{loc}^{GB}=\sigma_0(H_a-H_{return})$, and thus the maximum of the magnetization appears at $\sigma_0 H_a>0$ for the positive branch of the magnetization and at $\sigma_0 H_a<0$ at the negative branch (see section 4.2.2). This situation leads to a hysteretic behaviour of J_c with the applied magnetic field as it has been discussed in section 4.2.4.c.

We have studied the dependence of J_c^{GB} with the local magnetic field, which gives us a non hysteretic curve, $J_c^{GB}(H_{loc}^{GB})$. In order to do that, we have to subtract the contribution of the return field to the whole hysteresis loop. In section 4.2.4, we have determined the return field at each applied field of the hysteresis loop, $\sigma_0 H_{retun}(H_a)$ considering a certain field dependence of J_c^G, and we have subtracted the corresponding values to the applied field. In this section, since we want to analyze several hysteresis loops and a priori we do not know the field dependence of J_c^G, we have used an approximation to determine the curve $J_c^{GB}(H_{loc}^{GB})$, by considering that the return field does not depend on the applied magnetic field for the field range analyzed, i.e. $\sigma_0 H_{retun}$ is almost constant in all the hysteresis loop. As we can directly determine the value of $\sigma_0 H_{return}$ at the magnetization peak, when $\sigma_0 H_{loc}^{GB}=0$ and $\sigma_0 H_{peak}=\sigma_0 H_{return}$, we have calculated the local magnetic field at the grain boundary as $\sigma_0 H_{loc}^{GB}=\sigma_0(H_a-H_{peak})$. Fig. 5-34 shows the normalized J_c^{GB} determined for the sample IBADt1.6a_{Gott}, as a function of the local field calculated in section 4.2.4 as $\sigma_0 H_{loc}^{GB}=\sigma_0(H_a-H_{return}(H_a))$ (closed symbols) compared with $\sigma_0 H_{loc}^{GB}=\sigma_0(H_a-H_{peak})$ (open symbols). Notice that both curves show the same field dependence of J_c^{GB} and only a slight shift in the local

magnetic field of ≈0.015T has been observed. Hence, we are not inducing too much error by considering $\sigma_0 H_{loc}^{GB} \approx \sigma_0(H_a - H_{peak})$ whereas we are simplifying very much the analysis.

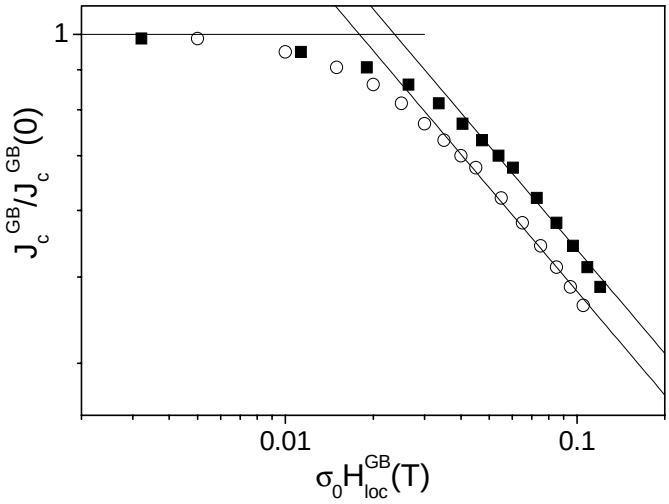

Fig. 5-34. Normalized GB critical current determined for the sample IBADt1.6a$_{Gott}$ at 50K, as a function of the local magnetic field calculated as $\sigma_0 H_{loc}^{GB}=\sigma_0(H_a-H_{return}(H_a))$(closed symbols) and as $\sigma_0 H_{loc}^{GB}=\sigma_0(H_a-H_{peak})$ (open symbols).

Fig. 5-35 shows the GB critical current density determined from the reverse branch of the hysteresis loop, measured at 77K, for the IBAD coated conductor IBADt1.2$_{Gott}$ as a function of the applied magnetic field (closed symbols) and as a function of the local magnetic field at the grain boundary calculated as $\sigma_0 H_{loc}^{GB}=\sigma_0(H_a-H_{peak})$ (open symbols). The latter is the one that we will use in order to determine the dependence of J_c^{GB} with the magnetic field.

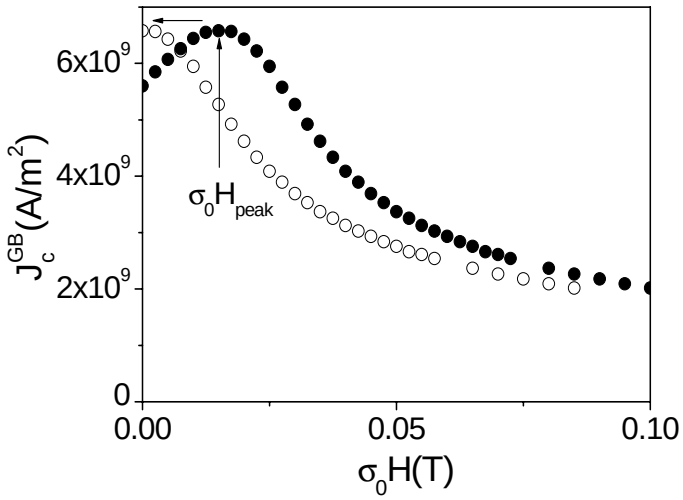

Fig. 5-35. Critical current density determined for the sample IBADt1.2$_{Gott}$ at 77K as a function of the applied magnetic field, $\sigma_0 H_a$ (closed symbols) and as a function of the calculated local magnetic field at the grain boundaries, $\sigma_0 H_{loc}^{GB}=\sigma_0(H_a-H_{peak})$ (open symbols).

Fig. 5-36 shows the magnetic field dependence of J_c^{GB} obtained for sample IBADt1.2$_{Gott}$ at 5K, 50K and 77K. We observe a plateau at low magnetic fields and a power law behaviour at large magnetic fields, $J_c^{GB}(H) \propto H^{-\zeta}$, with $\zeta \approx 0.5$ for all the temperatures. Therefore, we can determine a crossing field, $\sigma_0 H_{cross}^{CC}$, indicated by arrows in the figure, as the point where the plateau change to a power law.

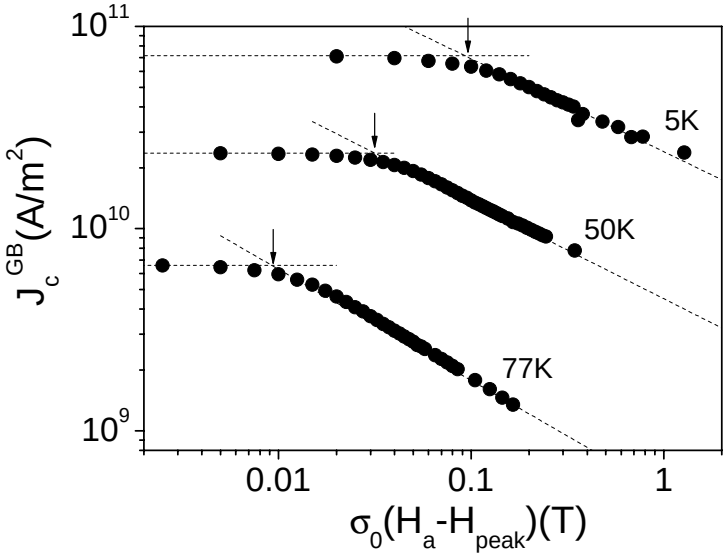

Fig. 5-36. Magnetic field dependence of the GB critical current density obtained for the IBAD CC IBADt1.2$_{Gott}$ at various temperatures. The arrows indicate the accommodation field $\sigma_0 H_{cross}^{CC}$ determined at each temperature.

Fig. 5-37 shows the values of ζ obtained for a great variety of IBAD and RABiTS coated conductors analyzed at different temperatures. Notice that for all of them we have found an exponent $\zeta \approx 0.5$, independent of the temperature. Very recently, our group has succeeded in performing transport critical current measurements in YBCO coated conductors. They have also found a plateau for the transport critical current density at low applied magnetic fields and a power law dependence with values of $\zeta \approx 0.5$, also independent of the measuring temperature (5K-77K), at high magnetic field, similarly to what we have observed for all the samples analysed.

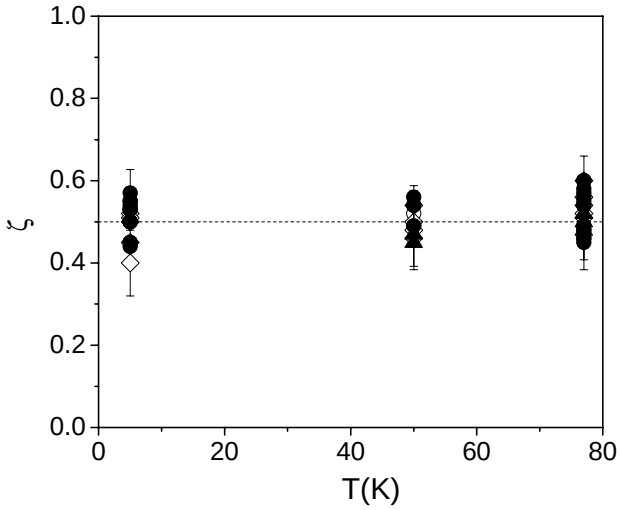

Fig. 5-37. Exponents ζ for the power low fit, $J_c(H) \propto H^{-\zeta}$, at high magnetic fields for several PLD IBAD CCs ( ), PLD RABiTS CCs ( ), BaF_2 RABiTS CCs ( ) and BaF_2 IBAD CCs ( ).

In the case of coated conductors, we have to take into account that the dislocation cores present at the grain boundaries can act as a linear pinning centres (see section 1.4.1). The potential of dislocations to enhance vortex pinning can be appreciated if one evaluates the matching field, B_A, for which the vortex distance, $a_0=(A_0/B)^{1/2}$, in the GB equals the dislocation spacing, $D=|\mathbf{b}|/2\sin(\chi/2)$ (see section 1.4.1). For a 5° boundary, the dislocation spacing is about D≈4-5nm, which gives $B_A \approx 100$T. Consequently, for the range of grain boundaries that one has in coated conductors, 5°-12°, we expect that all the AJV in the boundary encounter a free pinning centre, at all applied magnetic fields. In that case, assuming a 1D array of AJV pinned at the grain boundaries, with a motion dominated by their pinning energy, thus where the interaction between these AJV and the neighbouring AV is negligible, we can determine the critical current density considering the AJV in a single vortex pinning regime according to equation 5-2 ($J_c B \propto n f_p$). However, since the vortex motion is dominated by a line of equally spaced defects, the density of pinned vortices will be $n=1/(wa_0)$, where w is the GB width and thus we obtain a field dependence of J_c^{GB},

$$J_c^{GB} \propto \frac{f_p}{w\sqrt{A_0}} \frac{1}{\sqrt{B}} \qquad 5\text{-}10$$

in clear agreement with the experimental results. This dependence has been previously observed in YBCO thin films grown on bicrystal substrates [28] and predicted for a network of strong pinning planar defects [30].

One would expect that this behaviour would be maintained by lowering the magnetic field. However, that is not the case observed experimentally. At

$\sigma_0 H < \sigma_0 H_{cross}^{CC}$, a plateau with J_c independent of H is reached. By analyzing the values $\sigma_0 H_{cross}^{CC}$ obtained for several IBAD and RABiTS coated conductors and comparing them with the crossing field, $\sigma_0 H_{cross}$, measured for non-granular YBCO thin films (see Table 5-1) we realize that $\sigma_0 H_{cross}^{CC}$ is surprisingly similar to $\sigma_0 H_{cross}$, and that these values do not appreciably depend on the thickness of the YBCO layer or on the deposition process. For the coated conductors we have considered a larger error in $\sigma_0 H_{cross}$ according to the error that we induce determining the local magnetic field as $\sigma_0 H_{loc}^{GB} = \sigma_0 (H_a - H_{peak})$.

Sample	***Substr.***	***Grown process***	***t(σm)***	***$\sigma_0 H_{cross}$(T) (T=5K)***	***$\sigma_0 H_{cross}^{CC}$(T) (T=5K)***	***d_0(nm)***
$SCt0.27_{ORNL-A}$	*SC*	*BaF_2*	*0.27*	*0.12∂0.01*		*129∂5*
$RABt0.34_{ORNL-B}$	*RABiTS*	*BaF_2*	*0.34*		*0.13∂0.05*	*124∂24*
$RABt0.63_{ORNL-B}$	*RABiTS*	*BaF_2*	*0.63*		*0.16∂0.05*	*111∂20*
$SCt0.25_{Gott}$	*SC*	*PLD*	*0.25*	*0.15∂0.01*		*113∂20*
$IBADt1_{Gott}$	*IBAD*	*PLD*	*1*		*0.13∂0.05*	*124∂24*
$IBADt1.6a_{Gott}$	*IBAD*	*PLD*	*1.6*		*0.095∂0.05*	*145∂35*

Table 5-1. Values of $\sigma_0 H_{cross}$ determined for two YBCO non-granular thin films and $\sigma_0 H_{cross}^{CC}$ found for several YBCO IBAD and RABiTS coated conductors, at T=5K. We have also shown the correspondent average defect spacing.

This result seems to indicate that there is a clear correlation between $\sigma_0 H_{cross}^{CC}$, associated to AJV motion, and $\sigma_0 H_{cross}$, associated to the matching field of the grains. i.e. to the appearance of interstitial AV. So that, assuming that $\sigma_0 H_{cross}^{CC}$ could be related with the pinning centres existing inside the grains we can determine the corresponding dislocation spacing by $d_0 = (A_0/B_A)^{1/2}$, where we have considered $B_A(5K) \Im \sigma_0 H_{cross}(5K)$ for non-granular single crystals and $B_A(5K) \Im \sigma_0 H_{cross}^{CC}(5K)$ for the coated conductor grains. In that case, similar values of $\sigma_0 H_{cross}$ and $\sigma_0 H_{cross}^{CC}$ would mean similar density of pinning centres in the non-granular single crystals than in the coated conductor grains (see Table 5-1).

The observed plateau at $\sigma_0 H < \sigma_0 H_{cross}^{CC}$ might be understood by assuming that the AJV at the grain boundaries are moving through channels between strongly pinned AV ($\sigma_0 H < B_A$) like in the experiment of [99-101]. In that case the vortex channels have been generated by irradiating a BISCCO single crystal by heavy ions with a mask in such a way that columnar tracks were formed in regions of the sample leaving weak pinning channels. In this experiment vortex motion of weakly pinned vortices in the channels is dominated by the interaction between these vortices and the neighbouring strongly pinned vortices, i.e. the pinning energy in the channel is small in comparison with the elastic energy. Therefore in order to move the vortices of the channel the

Lorentz force has to be balanced with the elastic force determined by the shear modulus, c_{66}, and the critical current density can be expressed as,

$$J_c \nabla c_{66} / wB \qquad 5\text{-}11$$

where w is the width of the channel and c_{66} is given by equation 5-6, resulting a J_c independent of B.

In our case, this interpretation would imply that at low magnetic fields, AJV weaker pinned at the GBs move plastically in between strongly pinned AV, i.e. AV would hold AJV retarding its motion until the Lorentz force surpasses the shear force. This situation would be in agreement with the results shown in section 5.3.1 for CC of different thickness analysed at about zero magnetic field.

In any case, it is surprising that at low magnetic fields the experimental results seem to indicate that a strongly interacting AV-AJV system is encountered (plateau of $J_c^{GB}(H)$) while at higher magnetic fields a system governed by individual pinning motion of AJV in a 1D distribution of linear defects is attained ($J_c^{GB}(H) \nabla H^{-0.5}$). In addition, it is important to remind that the crossover between these two regimes has to be related with the appearance of interstitial vortices at the grains. One could imagine that these interstitial vortices are able to shield the strong interaction between the strongly pinned AV and the AJV at the GBs and by some means enable AJV to enter into a single vortex regime governed by their own pinning entergy.

The different field dependence of J_c, that can be observed for non-granular thin films and coated conductors has been compared in Fig. 5-38. Notice that, as we have discussed above, the values of $\sigma_0 H_{cross}$ and $\sigma_0 H_{cross}^{CC}$ (where the critical current density starts to decrease with a power low behaviour), are similar in both systems at each temperature. However, since the value of J_c for the non-granular thin film decreases faster with the magnetic field than the value of J_c^{GB} for the coated conductor we can define another crossing field that we call, $\sigma_0 H_{joint}$, which marks the point where the two critical currents merge. In this situation the current density necessary to move vortices located at the grain boundaries, already moves vortices located inside the grains, i.e. $J_c^{GB} \Im J_c^G$. The same crossover field has been determined from transport measurements performed in bicrystals [89] (see Fig. 5-28) and in coated conductors [102].

Above $\sigma_0 H_{joint}$ the coated conductor does not follows the power law $J_c(H)\nabla H^{-0.5}$ (expected for 1D distribution of AJV motion in a single vortex pinning regime), since we are moving AJV and AV at the same time. The $J_c(H)$ dependence measured above $\sigma_0 H_{joint}$ seems to follow a power law similar to that observed for the non-granular film until the magnetic field approaches the irreversibility line where a faster decrease of $J_c(H)$ is observed (see section 5.3.2.b). In any case, the motion above $\sigma_0 H_{joint}$ should be associated to a complicated situation where motion of both AJV and AV has to be considered.

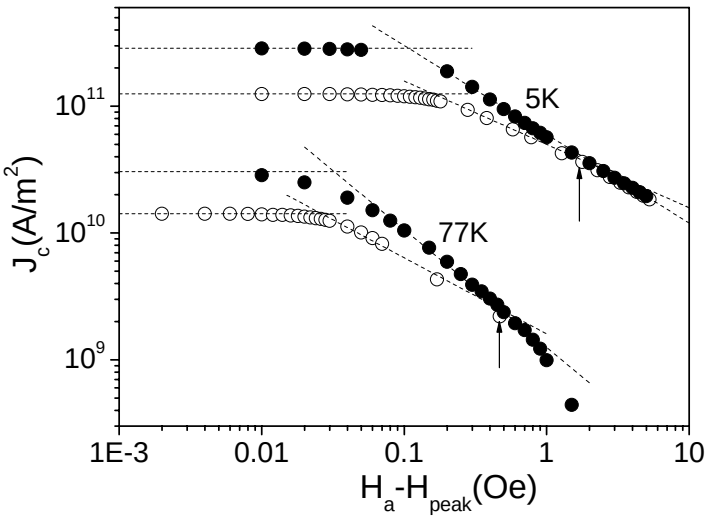

Fig. 5-38. Magnetic field dependence of the critical current density obtained for a non-granular YBCO thin film, SCt0.66$_{ORNL-A}$, and for a coated conductor, RAB.t1.37$_{ORNL-C}$, at 5K and 77K. We have indicated with arrows the values of $\sigma_0 H_{joint}$ at each temperature.

By determining the values of $\sigma_0 H_{cross}^{CC}(T)$ and $\sigma_0 H_{joint}(T)$ at different temperatures we can define a phase diagram for vortex motion in coated conductors.

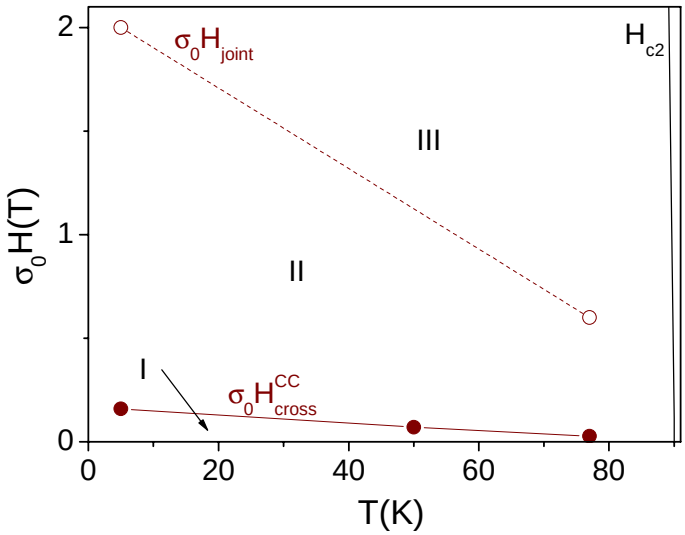

Fig. 5-39. Magnetic phase diagram for AV and AJV in a coated conductor, determined from the analysis of $J_c^{GB}(H)$ and $J_c^G(H)$, where three different regimes can be described.

At low field, below $\sigma_0 H_{cross}^{CC}$, (region I) only motion of AJV at the grain boundaries has to be considered ($J_c^{GB}<J_c^G$). In this case, the observed plateau of $J_c^{GB}(H)$ might be understood assuming that AJV move plastically in between the strongly pinned AV in the grains ($\sigma_0 H<B_A^G$) by overcoming the shear force. So that, we have to consider that the vortex-vortex interaction force is higher than the pinning force.

In the region between $\sigma_0 H_{cross}^{CC}$ and $\sigma_0 H_{joint}$ (region II) we also have motion of AJV at the grain boundaries ($J_c^{GB}<J_c^G$) although now there are interstitial AV in the grains. According to the power law dependence obtained $J_c^{GB}(H)\nabla H^{-0.5}$, the AJV motion has been associated to an individual pinning regime of 1D distribution of linear defects. In this case the GB pinning force dominates over vortex-vortex interaction force.

At high magnetic fields, above $\sigma_0 H_{joint}$, (region III) J_c^{GB} equals J_c^G and motion of both AV and AJV has to be considered. The pinning regime that we observe in this region is associated to a collective regime which give a power law dependence $J_c(H)\nabla H^{\zeta}$, with $\zeta \Im 0.5\text{-}1$. When the applied magnetic field approaches the irreversibility field we observe a strong decrease of J_c.

5.4 MECHANICAL DEFORMATION OF THE TAPES

For current transport applications, coated conductors have to be flexible and long length materials able to transport high currents through a percolative network of small angle grain boundaries. We have seen that the ability to transport large current densities is principally limited by grain boundary misorientation (section 5.2) but of course a good connection between grains, with no cracks formation at the grain boundaries, have to be insured in order to avoid a critical current reduction.

To deal with this issue and characterize the maximum stresses that can be applied to YBCO coated conductors, we have studied the evolution of J_c^{GB} and J_c^G after mechanical deformation of the tapes. Two coated conductors with different substrate architectures, RABiTS and IBAD, have been considered in order to evaluate the strain tolerance in each case. $RABt0.63_{ORNL\text{-}B}$, which is a 0.63σm film grown by BaF_2 ex situ process on a CeO_2(0.015σm)/YSZ(0.15σm)/Y_2O_3(0.2σm)/Ni(1.5σm)/NiW RABiTS tape(50σm) and $IBADt1_{Gott}$ which is a 1σm film grown by PLD on a CeO_2(0.9σm)/IBAD-YSZ(1σm)/NiCr SS tape(100σm). Bending tests have been performed on both samples. The tests consisted on winding the samples around cylinders of different

radius, ψ, with the YBCO layer facing outside, inducing a tensile bend strain at the layer. Thus, the applied strain was increased by decreasing the cylinder radius. The bend strain tolerance has been characterized by the percentage deformation, κ, calculated assuming a tape with homogeneous mechanical properties, $\kappa=L/2\psi$, where L is the substrate thickness (L≅50σm for the RABiTS CC and L≅100σm for the IBAD CC), that is much smaller than the bending diameter [103]. However the actual strain experienced by the YBCO layer could be less than κ because of the different mechanical properties of the metallic substrate and the oxide layers.

Fig. 5-40 shows the reverse branch of saturated hysteresis loops measured for the sample $RABt0.63_{ORNL-B}$ at 77K, as grown, κ=0%, and after three consecutive bendings around cylinders of radius ψ=0.8cm, 0.62cm and 0.4cm, which corresponds to induced deformations of κ=0.31%, 0.4% and 0.62%, respectively. Notice that an important reduction of the magnetization has been observed after each bending step which is associated to a decrease in J_c^{GB} according to equation 4-12, i.e. $J_c^{GB}=3M_{peak}^{sat}/R$.

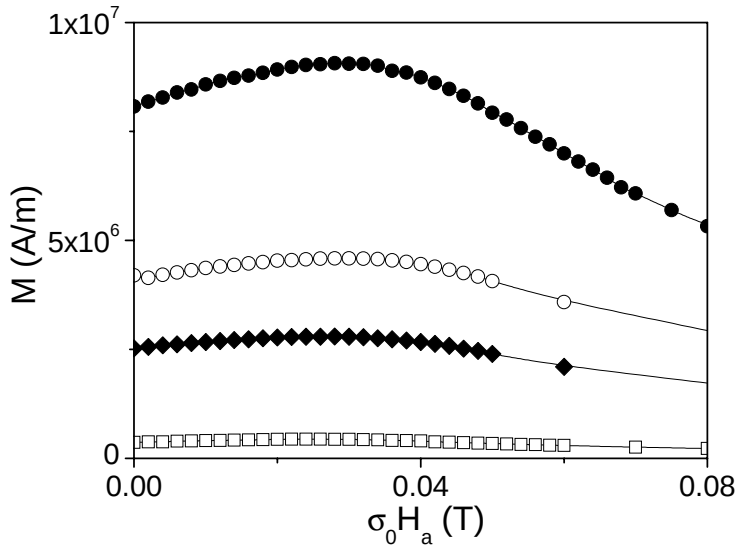

Fig. 5-40. Saturated reverse branches of the magnetization curve for $RABt0.63_{ORNL-B}$ at 77K, as grown (⌀) and after consecutive bendings tests with induced deformations of κ=0.31% (ʒ), κ=0.4% (↓) and κ=0.62% (Ĭ).

However, when the reverse curves are normalized to the corresponding magnetization value at the peak position (Fig. 5-41), one can observe that the magnetization peak appears at exactly the same applied magnetic field after the first and the second bending, $\sigma_0H_{peak}^{sat}$=0.028T, and at a slightly lower field after the third one, $\sigma_0H_{peak}^{sat}$=0.026T. The saturation of the remanent magnetization, shown in Fig. 5-42 also occurs at the same maximum applied field, $\sigma_0H_m(M_{rem}^{sat})$≅0.06T, for the

sample as grown and after the first two bendings, while $\sigma_0 H_m(M_{rem}^{sat})$≈0.05T after third one. With these values of $\sigma_0 H_{peak}^{sat}$, and $\sigma_0 H_m(M_{rem}^{sat})$ the grain size, <2a> and J_c^G can be determined using equations 4-10 and 4-7, respectively.

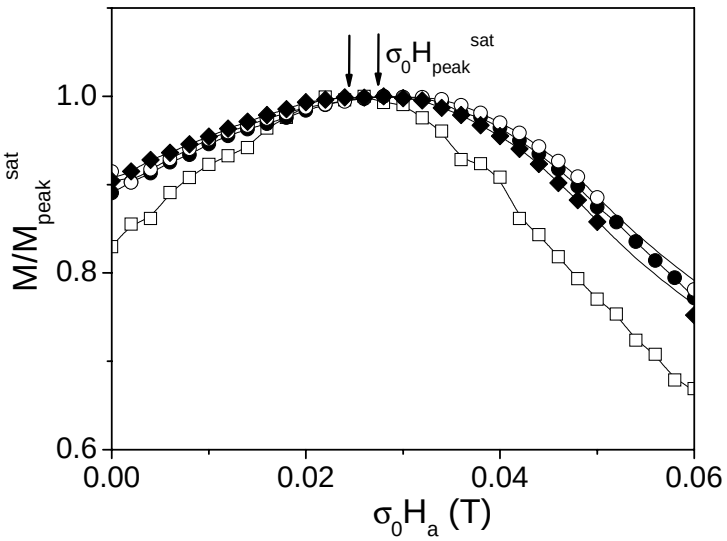

Fig. 5-41. Saturated reverse branches of the magnetization curve for RABt0.63$_{ORNL-B}$ at 77K, normalized to the saturated value of the magnetization at the peak, M_{peak}^{sat}, as grown (▫) and after consecutive bendings tests with induced deformations of κ=0.31% (○), κ=0.4% (◆) and κ=0.62% (□). The magnetic field at the peak position, $\sigma_0 H_{peak}^{sat}$, is indicated with arrows.

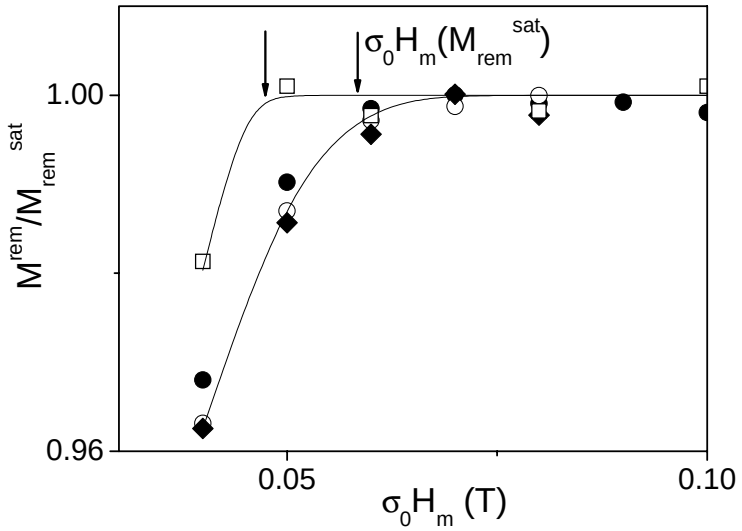

Fig. 5-42. Remanent magnetization normalized to its saturated value as a function of the maximum applied field, for RABt0.63$_{ORNL-B}$ at 77K, as grown (▫) and after consecutive bendings tests with induced deformations of κ=0.31% (○), κ=0.4% (◆) and κ=0.62% (□). Pointed with arrows are the maximum fields that saturates M^{rem}, $\sigma_0 H_m(M_{pem}^{sat})$.

Fig. 5-43 shows the evolution of J_c^{GB} and J_c^G with the bending strain, κ, at 77K. We clearly see that J_c^{GB} is reduced after each deformation, while J_c^G stays constant during all the bending process. Notice that the grain size, presented in Fig. 5-44, neither changes when the sample is deformed, being <2a>≈25σm.

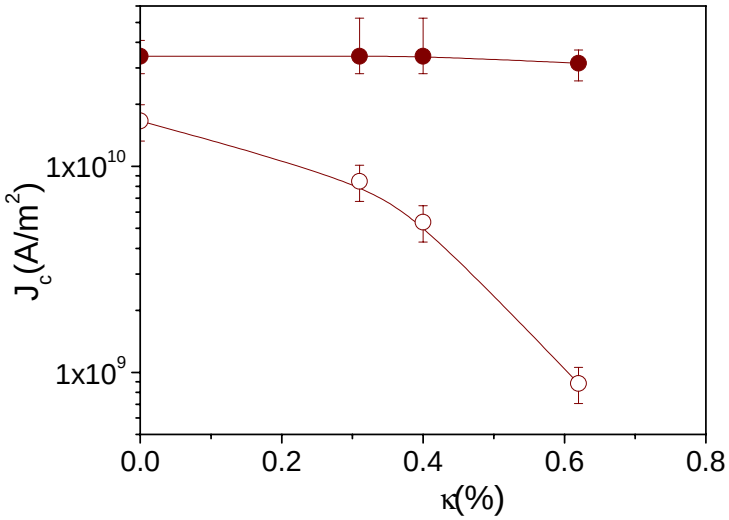

Fig. 5-43. J_c^G (closed symbols) and J_c^{GB} (open symbols) as a function of the bending strain, κ, for the RABiTS sample RABt0.63$_{ORNL-B}$ at 77K.

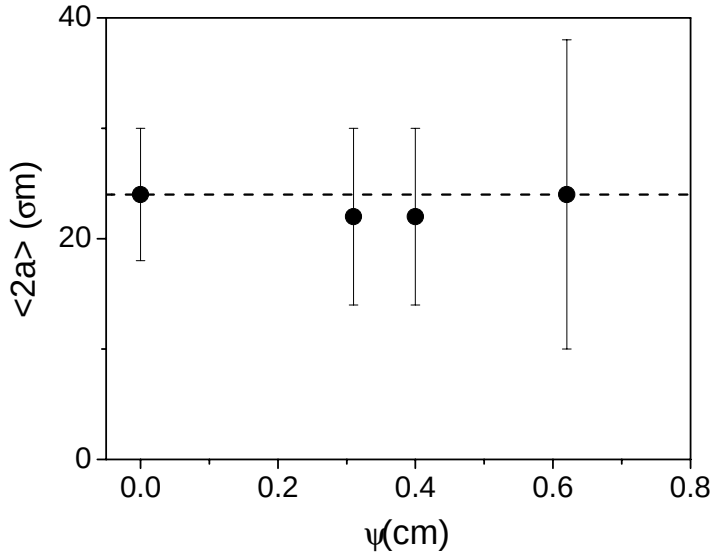

Fig. 5-44. Average magnetic grain size, <2a>, determined for the sample RABt0.63$_{ORNL-B}$ as a function of the bend strain.

The reduction in J_c^{GB} indicates that the grain boundary network has been damaged when the sample is submitted to large strain deformations. Fig. 5-45 shows a scanning electron microscopy (SEM) image of the sample RABt0.63$_{ORNL-B}$, after all the sequence of bending tests corresponding to a $J_c^{GB}(\kappa=0.62\%)/ J_c^{GB}(\kappa=0\%)=0.05$, where one can clearly identify the formation and propagation of transverse cracks in some regions of the sample, which confirms the degradation of the percolative critical current and evidences the importance of controlling the mechanical properties of these materials.

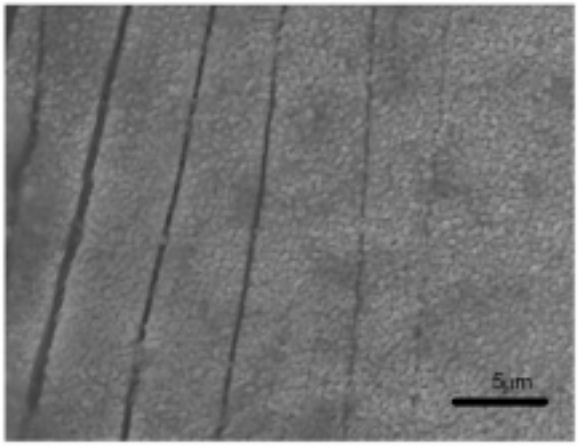

Fig. 5-45. SEM image of the sample RABt0.63$_{ORNL-B}$ after three consecutive bendings with induced deformations of κ=0.31%, 0.4% and 0.62%. Transverse cracks can be observed, caused by tensile stress.

Additionally, as J_c^G stays constant after all the bending strains, we can conclude that the pinning of the Abrikosov vortices within the grains is not affected for the mechanical deformation of the tapes and that the cracks induced are only located at the grain boundaries.

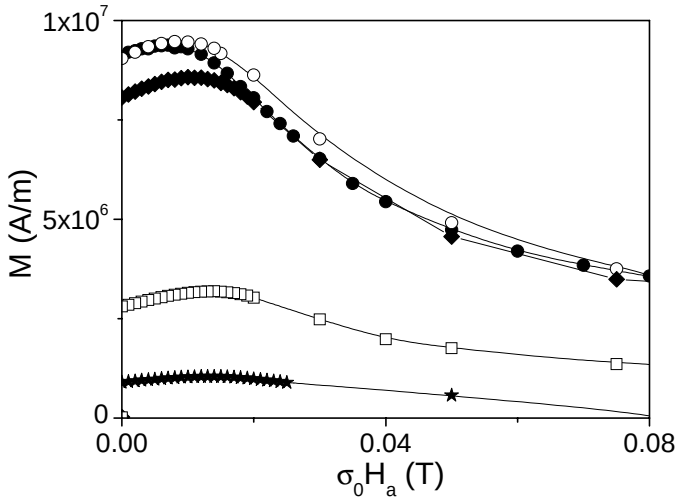

Fig. 5-46. Saturated reverse branches of the magnetization curve for IBADt1$_{Gott}$ at 77K, as grown (⇄) and after consecutive bending tests with induced deformations of κ=0.63% (ʒ), 0.8%(↓), 1.25% (Ĭ) and 2.6% (Ċ).

The same analysis has been performed to an IBAD coated conductor, IBADt1$_{Gott}$. Shown in Fig. 5-46 the obtained saturated reverse branches of the magnetization curve, at 77K, before bending tests, κ=0%, and after the induced deformations of κ=0.63%, 0.8%, 1.25% and 2.6%. Comparing these curves with the ones obtained for the RABiTS sample (Fig. 5-40) we observe that in the latter case, the magnetization also decreases after each bending process but the strain needed to obtain the same reduction in magnetization is higher. This corresponds to a faster

degradation of J_c^{GB} with the bending strain for the RABiTS sample than for the IBAD, as it will be shown in Fig. 5-51.

From the normalized reverse magnetization curves obtained for IBADt1$_{Gott}$, shown in Fig. 5-47, one observes that the magnetization does not peak at the same applied field after the bending tests, as it happened for the RABiTS CC, but rather the peak moves to higher magnetic fields when the sample is bended, $\sigma_0 H_{peak}^{sat}$=0.007T, 0.008T, 0.01T, 0.013T, 0.013T for κ=0.63%, 0.8%, 1.25% and 2.6%, respectively. Moreover, the saturation of the grain magnetization takes place at lower magnetic fields after each deformation, $\sigma_0 H_m(M_{rem}^{sat})$ 0.04T, 0.035T and 0.028T for κ=0%, 0.8% and 2.6%, respectively, as it is shown in Fig. 5-48.

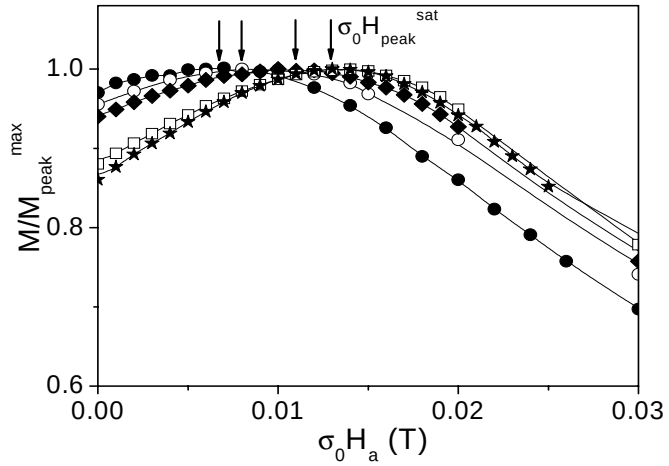

Fig. 5-47 Saturated reverse branches of the magnetization curves, normalized to the saturated value of the magnetization at the peak, M_{peak}^{sat}, obtained for IBADt1$_{Gott}$, at 77K, as grown (▲) and after consecutive bending tests with induced deformations of κ=0.63% (▼), 0.8%(↓), 1.25% (■) and 2.6% (●).The magnetic field at the peak position, $\sigma_0 H_{peak}^{sat}$, is indicated for each curve.

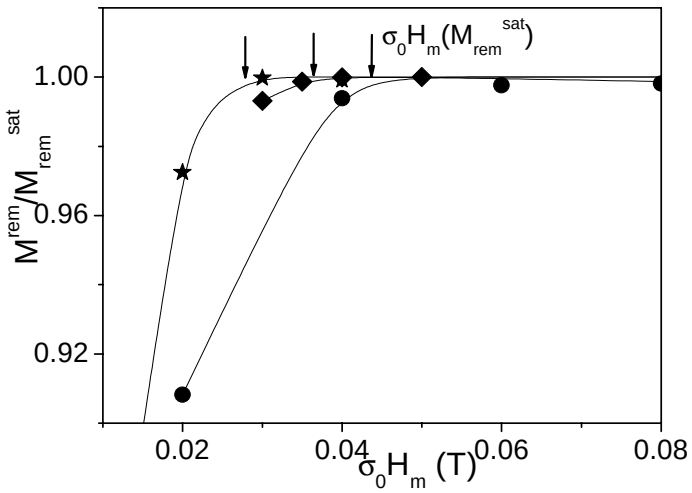

Fig. 5-48. Remanent magnetization normalized to its saturated value as a function of the maximum applied field for IBADt1$_{Gott}$ at 77K, as grown (▲) and after consecutive bending tests with induced deformations of 0.8%(↓) and 2.6% (●). Pointed with arrows the maximum field that saturates M^{rem}, $\sigma_0 H_m(M_{pem}^{sat})$.

The different values obtained for $\sigma_0 H_{peak}^{sat}$, $H_m(M_{rem}^{sat})$ result in variations of J_c^G and grain size, <2a>, during the bending process performed to the IBAD CC, contrary to what happens for the RABiTS sample. Fig. 5-49 shows the values of J_c^G obtained, as a function of the applied bending strain. Notice that in this case, not only J_c^{GB} decreases with the bending tests, but also J_c^G decreases. At the same time, the average grain size, shown in Fig. 5-50, increases after each deformation.

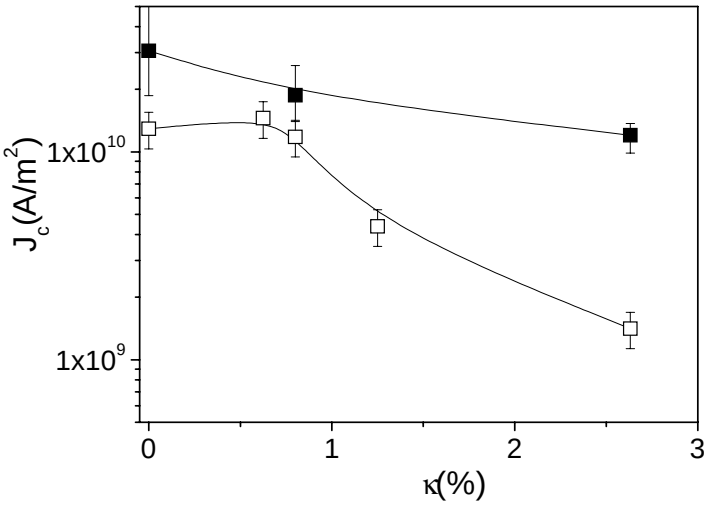

Fig. 5-49. J_c^G (closed symbols) and J_c^{GB} (open symbols) as a function of the bending strain, κ, obtained for the IBAD sample IBADt1$_{Gott}$ at 77K.

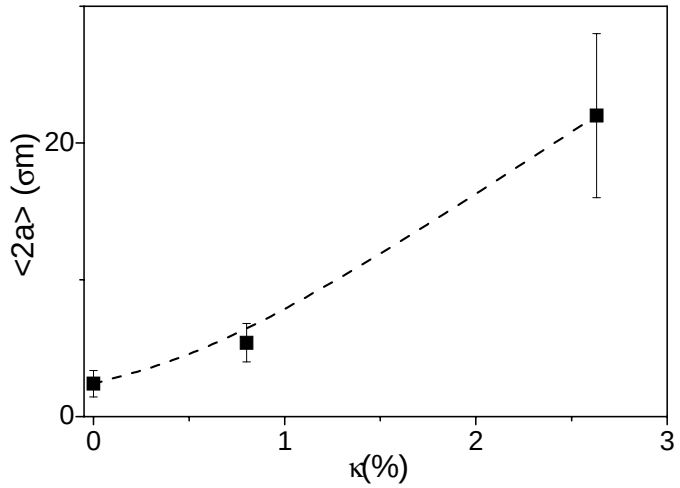

Fig. 5-50. Average magnetic grain size, <2a>, determined for the IBAD sample IBADt1$_{Gott}$ as a function of the bend strain.

The behaviour observed with the IBAD CC can be understood if one assumes that after bending, the grain boundary network become inhomogeneous, i.e. grain boundaries with different quality may exist. The strain deformation could deteriorate some of the high angle GBs (HAGB) between the structural grains generating clusters (colonies) of well connected grains surrounded with current loops with a somewhat depredated critical current density, (for instance; $J_c^{col}/J_c^G \cong 0.7$ for κ=0.8%). Therefore

the final percolative current that would cross the sample, would be affected by the return field of structural grains and grain colonies. By using the program that we have developed to simulate hysteresis loops (presented in section 4.2.4) we have obtained that a 35% of isolated colonies of 10σm in a matrix of small grains (2σm) are able produce the effect observed on the hysteresis loops for κ=0.8%.

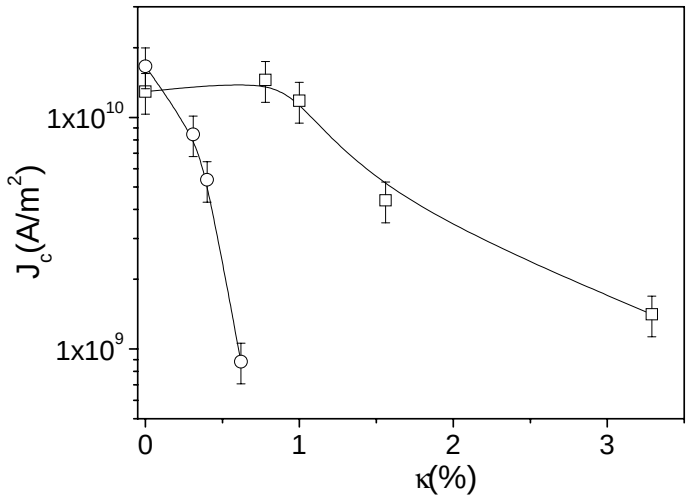

Fig. 5-51. J_c^{GB} as a function of the bend strain obtained at 77K, for the RABiTS sample RABt0.63$_{ORNL-B}$ (ı) and for the IBAD IBADt1$_{Gott}$ (Ã).

Comparing the values of J_c^{GB} obtained for both type of CCs after deformation tests (Fig. 5-51), one observes that the most rapid degradation of J_c^{GB} occurs for the RABiTS-CC, for instance, J_c^{GB} is reduced by 50% when we apply a deformation of κ=0.32% in the RABiTS-CC while for the IBAD-CC we have to apply a deformation of κ=1%. These results indicate that the strain tolerance of the YBCO layer grown on a NiCr stainless steel IBAD substrate is greater than that of the YBCO layer grown on a NiW RABiTS tape. Moreover, since it is known that the degradation of J_c^{GB} increases by increasing the thickness of the YBCO layer [103] this effect is even more evident. We have analyzed an IBAD CC with a thicker YBCO layer than the one grown on the RABiTS substrate and we have still obtained better mechanical properties for the IBAD CC. Therefore we can strongly conclude that IBAD CC possesses a better strain tolerance than RABiTS CC.

The reduction in J_c^{GB}, observed in both samples, clearly evidences that the grain boundary network of the YBCO layer has been damaged when the tape is submitted to strain deformation. The formation and propagation of transverse cracks in some regions of the sample, confirming the degradation of J_c^{GB}, have been observed by SEM in sample RABt0.63$_{ORNL-B}$ (Fig. 5-45).

As a conclusion we have seen that J_c^{GB} of coated conductors can be degraded by applying mechanical deformations at the tapes. For the RABiTS coated conductor we have identified a clear degradation of J_c^{GB} after bending test wile J_c^G stays constant. Moreover, for the IBAD-CC analyzed inhomogeneities on the GB network can be detected after bending. Additionally, we have observed a different strain tolerance for RABiTS and IBAD CCs. For the IBAD sample J_c^{GB} maintains a 90% of its original value when $\kappa<1\%$, while for the RABiTS sample $\kappa=0.32\%$ already reduces J_c^{GB} by 50%. On the other hand, recent axial strain measurements have shown a reversible strain limit for RABiTS of ℑ 0.4% [104]. The present results indicate that reinforcement may be required for RABiTS samples in applications involving extreme bending configurations.

5.5 CONCLUSIONS

In this chapter we have analyzed the values of grain and grain boundary critical current densities, J_c^G and J_c^{GB}, for different coated conductors in order to study their interaction and find which are the main factors that are limiting the percolative critical current in each case. Additionally, we have determined the average magnetic grain size, <2a>, associated to RABiTS and IBAD coated conductors.

We have found that the values of <2a> determined for standard RABiTS and IBAD coated conductors clearly differs in one order of magnitude, <2a>ℑ0.5-2.5σm for IBAD CCs while <2a>ℑ20-100σm for RABiTS CCs. These values agree with the structural grain size measured by EBSD and are the expected ones considering that the GBs in the YBCO layer replicate the substrate pattern. However, in some samples grown by ex situ BaF_2 based precursors, it has been observed by EBSD or TEM that large grains, overgrowing the substrate GB network, are induced by means of an uncontrolled growth process. We have identified these large grains with magnetic measurements and we have found that the associated J_c^{GB} is lower than that obtained for a sample with the YBCO grain boundaries replicating the substrate (grown by an optimized process). Additionally, we have analyzed samples grown by a best optimized process, which induce GB meandering, where J_c^{GB} is even higher. However, the correspondent values of J_c^G do not depend on the growth process indicating that the pinning capabilities of the grains have not change with changing the growing parameters. The different J_c^{GB} observed for the different growing processes has been associated to modifications induced in the GB microstructure, such us precipitates, out-

of-plane grain alignment or GB meandering. All this analysis has been performed with samples of similar texture.

The influence of the GB misorientation angle on J_c^G and J_c^{GB} has been studied by analyzing samples of very different texture. We have found that J_c^{GB} exponentially decreases by increasing the misorientation angle but J_c^G does not depend on the texture. These results clearly reflect the importance of reducing the GB misorientation in coated conductors since it is one of the principal limiting factors for the percolative critical current through the conductor.

By analysing the thickness dependence of J_c^G and J_c^{GB} at about zero magnetic field, we have found that for samples with similar texture J_c^{GB} decreases as well as J_c^G does, so that an interaction between Abrikosov Josephson vortices (AJV) in the GBs and Abrikosov vortices (AV) in the grains is proposed. These results can be explained by considering that stronger pinned AV in the grains, placed near a GB, could hold the AJV in the GBs retarding its motion. The observed decrease of J_c^G with the thickness can be understood by considering that the effectiveness of vortex pinning centres in the grains is higher near the interface between the YBCO layer and the substrate. This argument cannot however explain the decrease of $J_c^{GB}(t)$ since the dislocations at the GBs do instead extend through the full thickness of the layer.

Additionally, by means of measurements of $J_c^G(H)$ in YBCO non-granular thin films, and $J_c^{GB}(H)$ performed in YBCO coated conductors, we have also observed different vortex motion regimes for both systems.

For non granular thin films we have found a crossover field, $\sigma_0 H_{cross} \Im B_A$, that separates a region with J_c independent of the magnetic field (for $\sigma_0 H < \sigma_0 H_{cross}$) from another region where J_c follows a power law behaviour, $J_c(H) \nabla H^{-\zeta}$. The plateau of J_c can be associated to a single vortex pinning regime (region where all the vortices can find a free pinning centre) and the power law corresponds to a regime where vortex-vortex interactions have to be considered. This last regime is associated to the presence of interstitial Abrikosov vortices in the film. The exponent ζ of the power law varies from 0.5 to 1, according to a motion of Abrikosov vortex bundles in a plastic pinning or collective pinning regime, respectively. When approaching the irreversibility field, the critical current density decreases very fast with the applied magnetic field.

For YBCO coated conductors we have also observed a crossover field, $\sigma_0 H_{cross}^{CC}$, that separates a plateau of J_c from a power law dependence of $J_c^{GB}(H) \nabla H^{-\zeta}$.

However, in that case $\sigma_0 H_{cross}^{CC}$ cannot be related with the matching field associated to the GB dislocations, since it is always higher than the applied magnetic field, $B_A^{GB} \Im 100T$, but it can be related with the matching field associated to the coated conductor grains, $\sigma_0 H_{cross}^{CC} \Im B_A^G$ (although we are analyzing the motion of AJV at the GBs). Additionally we have found values of $\zeta \Im 0.5$ for all the coated conductors analyzed, independently on the temperature or the type of coated conductor considered. We associated the plateau observed at $\sigma_0 H < \sigma_0 H_{cross}^{CC}$ to a plastic motion of AJV in a channel surrounded by the strongly pinned AV ($\sigma_0 H < B_A^G$). The power law behaviour has been described by considering an individual pinning motion of AJV with a 1D distribution of linear defects. These results would indicate that when interstitial vortices appears at the grains, the AJV motion change from a strong interacting system of AV-AJV to a system governed by an individual vortex pinning regime at the GBs.

Another crossover field has been found at higher magnetic fields, $\sigma_0 H_{joint}$, from the point where J_c^{GB} and J_c^G merge. This field marks the transition from a regime where only AJV moves to a regime where both types of vortices (AJV and AV) are moving. From the two crossover fields determined at different temperatures we have built up a magnetic phase diagram describing the behaviour of vortex motion in YBCO coated conductor.

CHAPTER 6

AC-SUSCEPTIBILITY STUDY OF YBCO NON-GRANULAR THIN FILMS AND COATED CONDUCTORS

In the previous chapters we have clearly identified the signature of electromagnetic granularity from dc-magnetization curves, and determined and separated J_c^G and J_c^{GB} of coated conductors allowing its independent study.

Ac-susceptibility will be use as a complementary technique to understand the granular nature of YBCO coated conductors since these particular measurements are shown to be a unique tool able to identify different percolative grain boundary domains, which cannot be detected by transport or dc-magnetic measurements, but generate an important dissipation in the conductor. We have used the parametric plots $\theta''(\theta')$ in order to analyze the dissipation GB domains created in the sample. In addition we have studied the different pinning regimes and dynamic responses appearing at different temperatures and ac fields which have allowed us to build a dynamic phase diagram of

the vortex motion in YBCO non-granular thin films and coated conductors. By means of ac-susceptibility data taken at different frequencies we have determined the effective energy barrier for flux motion activated thermally, $U_e(J,T,B)$.

6.1 AC-SUSCEPTIBILITY STUDY OF YBCO THIN FILMS

6.1.1 YBCO THIN FILM GROWN ON A SINGLE CRYSTAL

Ac-susceptibility was already shown to be a very common and effective method to characterize superconducting materials in single crystals, thin films and polycrystalline forms [68,105]. A first ac-susceptibility analysis of a thin film grown on a STO single crystal ($SCt0.2_{THEVA}$) has been realized in order to use it as a typical example of a non-granular superconducting thin film.

Fig. 6-1 shows the temperature dependence of the real and the imaginary components of the ac-susceptibility, θ' and θ'' of $SCt0.2_{THEVA}$ for ac-field amplitudes of $\sigma_0 H_{ac}$=0.01, 0.05, 0.1, 0.5, 1 and 1.5mT at 1111Hz with no dc applied field. Notice that θ' is independent of the temperature until the temperature approaches the superconducting transition, $T_c \cong 88K$. Thus, complete flux shielding is observed until flux starts to penetrate the superconductor near the transition temperature. Accordingly, $\theta''=0$ when flux is shielded while at higher temperatures a peak is generated due to hysteretic losses produced by the flux penetration (see section 3.3.1)

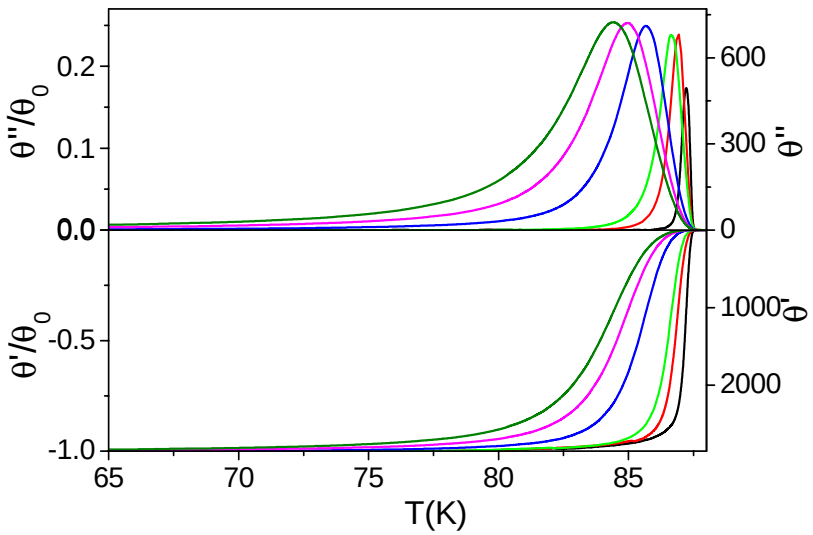

Fig. 6-1. Temperature dependence of the real, θ', and the imaginary, θ'', components of the ac-susceptibility, and the values normalized to its Meissner slope, $\theta'(T)/\theta_0$ and $\theta''(T)/\theta_0$ for the film $SCt0.2_{THEVA}$ for $\sigma_0 H_{ac}$=0.01, 0.05, 0.1, 0.5, 1 and 1.5mT at 1111Hz and zero dc applied field.

The large effect of the demagnetizing fields in thin film geometries can be seen in the absolute values of the ac-susceptibility at low temperatures, $\theta' \Im -2800$ instead of -1 (Right y axis of Fig. 6-1). Left y axis shows the normalized curves $\theta'(T)$ and $\theta''(T)$ to the calculated initial susceptibility for a thin disk, θ_0, defined in section 3.3.1, i.e. $\theta_0=8R/3\phi t$. Notice that this normalization, which takes into account the demagnetizing field effect, gives $\theta'/\theta_0=-1$ as would be expected. Additionally the peak value $\theta''_{peak}/\theta_0 \Im 0.24$ for all ac field amplitudes above $\sigma_0 H_{ac}=0.05$mT is in agreement with Bean critical-state model (section 3.3.1). For ac field amplitudes below 0.05mT this statement is not accomplished, as has already been observed by other authors [106] since we are not in the critical state regime and the theories based on the Bean model are not valid (see section 3.3.3).

We have determined the region, where the Bean model is applicable, by using the methodology described in section 3.3.3. Fig. 6-2 shows the Bean length described in equation 3-11, $\Theta_c=H_{ac}/J_c(T)$, determined according to this methodology, for the film $SCt0.2_{THEVA}$, as a function of $\sigma'=1+\theta'$.

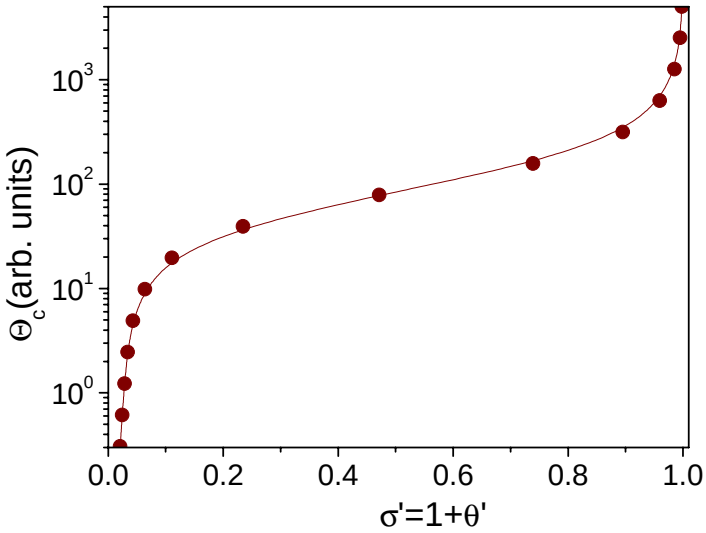

Fig. 6-2. Bean length Θ_c, as a function of $\sigma'=1+\theta'$ obtained for the sample $SCt0.2_{THEVA}$ through the method described in section 3.3.3.

Using the curves $\theta'(T)$ measured at different ac-field amplitudes, H_{ac}, we have determined the dependence of θ' with H_{ac} at a fixed temperature, and by means of the dependence $\Theta_c(1-\theta')$, shown in Fig. 6-2, we can determine Θ_c for each H_{ac} (see Fig. 6-3). In the Bean critical state regime J_c is independent of H_{ac}, and thus according to equation 3-11, Θ_c is proportional to H_{ac}. For the film analyzed we have indicated with arrows the field that marks the onset of the Bean regime at different temperatures, $\sigma_0 H_{ac}^c(T)$. In the same figure we can also identified the existence of a linear regime,

characterized by a Θ_c independent of $\sigma_0 H_{ac}$ (see section 3.3.3). The smooth crossover from linear to nonlinear response determines the boundary $H_{ac}^{l}(T)$

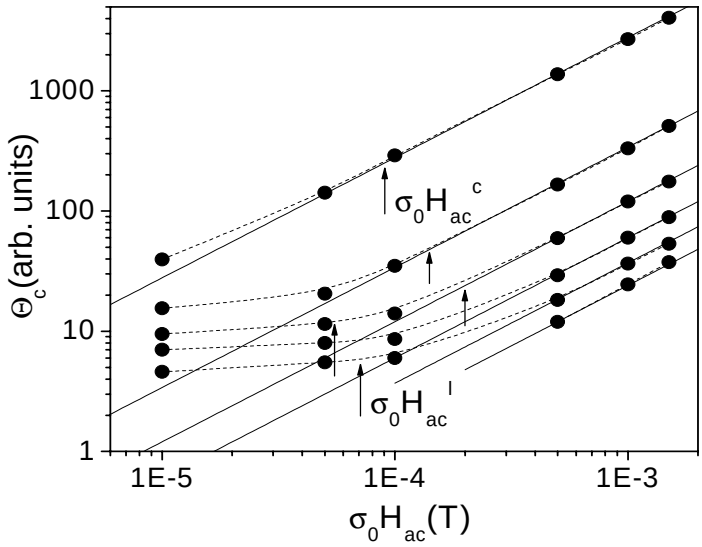

Fig. 6-3. Dependence of the Bean length Θ_c with the ac field amplitude obtained for the film SCt0.2$_{THEVA}$ at different temperatures, T=85K, 84K, 83K, 82K, 81K, 80K from top to bottom. Some of the points which describe the onset of the Bean regime, $\sigma_0 H_{ac}^{c}(T)$, and the crossover to a linear response, $\sigma_0 H_{ac}^{l}(T)$are indicated.

In order to best determine the crossover from linear to nonlinear response we have plot the values of θ' as a function of the ac magnetic field, at different temperatures (Fig. 6-4). The onset of a linear response, indicated by arrows in Fig. 6-4, marks the beginning of H_{ac} dependence of θ'. We have considered a deviation of 0.3% from the measured value at the lowest ac field to determine the crossover line, $\sigma_0 H_{ac}^{l}(T)$.

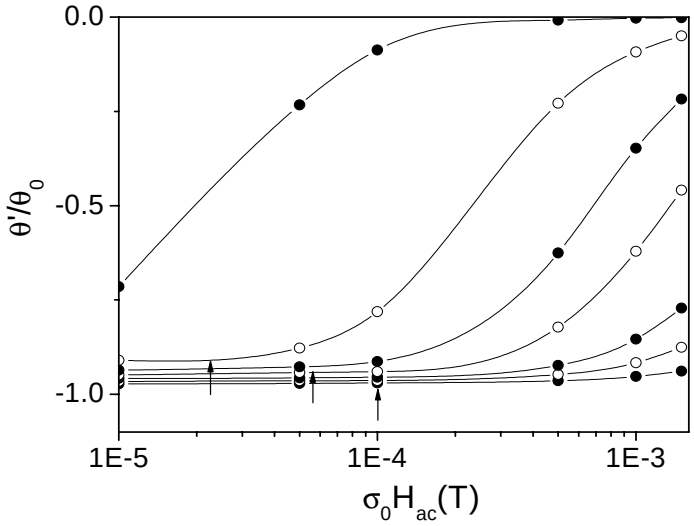

Fig. 6-4. θ' component of the ac-susceptibility as a function of the ac field, obtained for the film SCt0.2$_{THEVA}$ at zero dc applied field at different temperatures , T=87K, 86K, 85K, 84K, 82K, 80K, 75K, from top to bottom. Some of the points which describe the crossover to a linear response, $\sigma_0 H_{ac}^{l}(T)$, are indicated.

Once we have determined the transition lines $\sigma_0 H_{ac}^{c}(T)$ and $\sigma_0 H_{ac}^{l}(T)$, we can build up a phase diagram in the (H_{ac}, T) plane for this sample, and identify the various dynamic regimes and the crossover among them as it has been represented in Fig. 6-5. The phase diagram has been determined at f=1111Hz and at zero applied dc field. In section 3.3.3 we have described the different dynamic regimes appearing in the phase diagram considering a certain dc applied field. So that, we described the Campbell regime assuming pinned vortices oscillating inside the potential wells and the Critical state regime considering inter-valley motion which dominates over most of the sample. In our case, we have performed all the measurements at zero applied dc-magnetic field, but in any case, it is almost impossible to avoid vortices inside the sample due to the remanent field of the superconducting coil (≈0.1mT), even if the 9T coil is demagnetized before the measurements. For a thin film sample owing to the demagnetizing effects, an applied magnetic field of 0.1mT would correspond to an internal field of ≈250mT. Thus, the same interpretation of intra- and inter-valley excitations must be taken into account in the analysis of the response in the solid phase. If it could be ensured that a real zero dc field could be present in the sample, the interpretation of the linear regime should be in terms of true flux screening (London penetration depth), whereas in that of the critical state, only flux gradients of ac vortices (ac vortices inter-valley motions) should be considered.

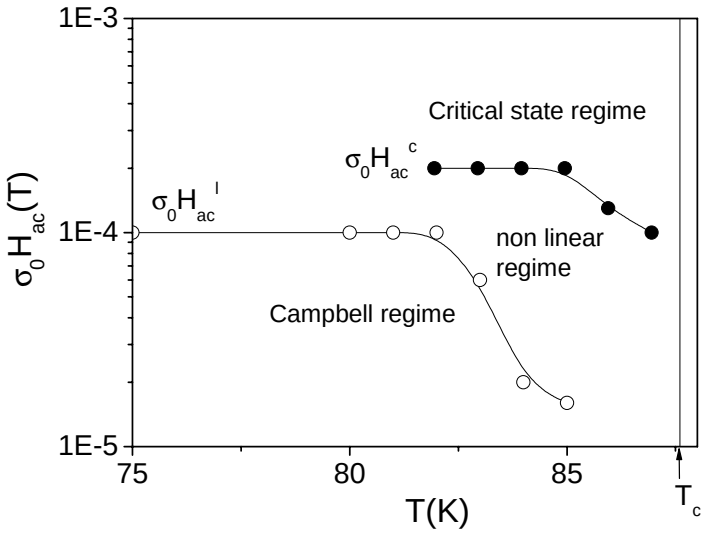

Fig. 6-5. Dynamic phase diagram in the (H_{ac}, T) plane determined for the thin film grown on a single crystal, SCt0.2$_{THEVA}$, at zero applied dc-magnetic field and with a frequency of f=1111Hz.

The transition to a reversible system (vortex liquid) at high temperatures, defined by the irreversibility line, IL, can also be obtained by ac-susceptibility data. By reducing the value of the field amplitude, H_{ac}, the dissipation peak position T_{peak}, can be

pushed to higher temperatures and it may be located at the onset of a nonlinear response, which defines the transition between the irreversible to the reversible state, i.e. it defines the IL [107-109]. Fig. 6-6 shows the temperature dependence of the dissipation peak $\div R\nabla\theta''$ measured for Civale et al. at a fixed dc applied field of 1T and different ac fields for YBCO thin film [107].

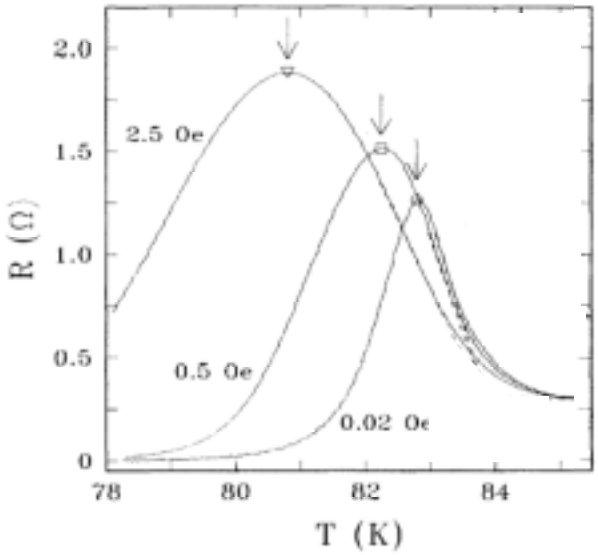

Fig. 6-6. Dissipation peaks θ'' as a function of temperature, measured in a single crystal at f=133.3Hz and with a cd-magnetic field of H_{dc}=0.05T [107].

We note that, even though the low temperature region of the dissipation peak and the position of its maximum, T_{peak}, vary with H_{ac}, at the high temperature side of the peak, $\theta''(T)$ become independent of H_{ac}, which means that it lies in the region of the linear response. So that, the maximum of $\theta''(T)$ at very low ac applied fields, mostly separates regions of linear and nonlinear behaviour for all ac fields. In consequence, we will determine the IL at the θ'' peak position measured at a low field amplitude ($\sigma_0 H_{ac}$=0.01mT). Fig. 6-7 shows the temperature dependence of the real and the imaginary components of the ac-susceptibility, obtained for the film $SCt0.2_{THEVA}$ at $\sigma_0 H_{ac}$=0.01mT and f=1111Hz for different applied dc-magnetic fields.

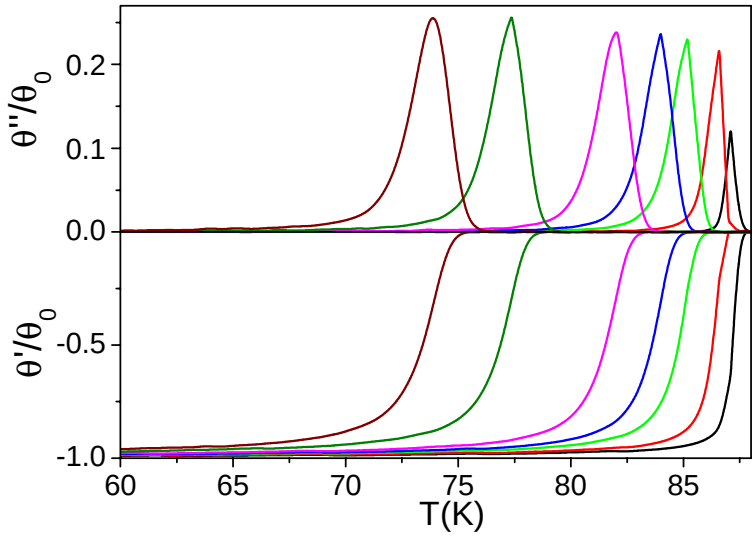

Fig. 6-7. Temperature dependence of θ'/θ_0 and θ''/θ_0 obtained for the film SCt0.2$_{THEVA}$ at $\sigma_0 H_{ac}$=0.01mT and f=1111Hz at different applied dc fields $\sigma_0 H_{ac}$=0T, 0.1T, 0.5T, 1T, 2T, 5.5T and 9T.

The IL determined from the θ''(T) curves measured at different dc fields is shown in Fig. 6-8. The experimental values can be fitted by the equation, $H=H_0(1-T/T_c)^B$, expected for YBCO with H_0=115T and B=1.45. The exponent B obtained is similar to that observed for YBCO, where B≅1.5 [109,110].

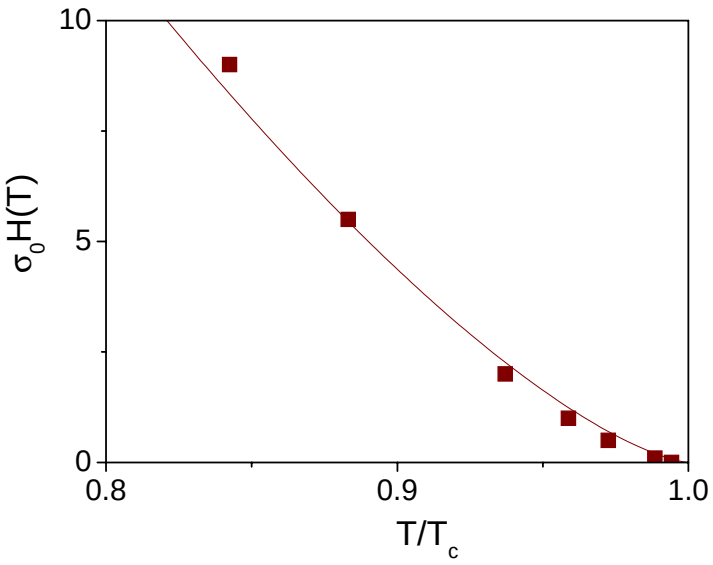

Fig. 6-8. Irreversibility line measured for a YBCO thin film grown on a single crystal, SCt0.2$_{THEVA}$.

The most convenient representation to study de dissipation in the sample is the parametric plot θ''(θ') described in section 3.3.2. Fig. 6-9 shows the normalized θ''(θ') plot obtained for the film SCt0.2$_{THEVA}$, compared with the one simulated for a thin disk in the Bean critical state model (see Fig. 3-9). The curve θ''(θ') has been determined at

$\sigma_0 H_{ac}$=0.5mT, assuring that the critical state is established at all temperatures, according to the onset determined in Fig. 6-3 and Fig. 6-5.

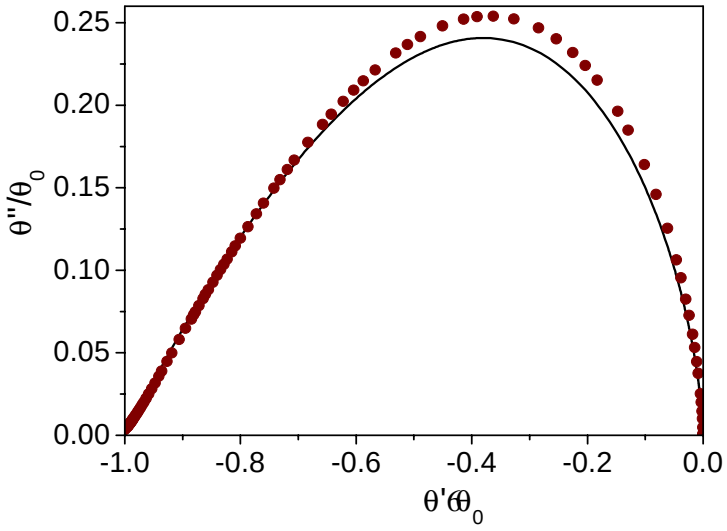

Fig. 6-9. Parametric plot of the complex susceptibility for the film SCt0.2$_{THEVA}$ measured with H_{ac}=0.5mT. Solid line shows the behavior of θ''(θ') for a thin disk in the Bean critical state model.

Notice that, although the two curves are very similar, in fact, θ''_{peak}/θ_0 is slightly higher, θ''_{peak}/θ=0.25, than the expected 0.24 for the Bean model and it is located at θ'_{max}/θ_0=-0.36, which is a little shifted towards θ'=0 in respect to the predicted value in the Bean model θ'_{max}/θ_0=-0.38. Such a small difference is understood by considering J_c to decrease with the magnetic field (see section 3.3.2). The slope of θ''(θ') for θ'⇓ -1 coincides following the theoretical slope up to θ'_{max}/θ_0= -0.7 indicating that no major flux creep effects are present and that we can interpret the experimental results in terms of the Bean critical state.

From the θ''(T) curves measured at different ac field amplitudes, H_{ac}, the critical current density as a function of the temperature, can be determined according to equation 3-12, i.e. $J_c(T_{peak})=2H_{ac}/1.94t$, valid for thin disks with 2R/t>100. Results of J_c(T) obtained by means of the θ''(T) curves presented above are shown in Fig. 6-10 (open symbols). We have also shown, with closed symbols, the J_c values obtained from magnetic hysteresis loops measurements, described in section 4.1.2, where the critical current density at zero internal field, can be determined with equation 4-1, i.e. $J_c=3M_{peak}^{sat}/R$. Although the range of temperatures where J_c can be determined by ac magnetization, with a maximum $\sigma_0 H_{ac}$=0.15mT, is not very wide, it is clear that the J_c values determined from ac-susceptibility measurements extrapolate to those calculated from dc-magnetic measurements.

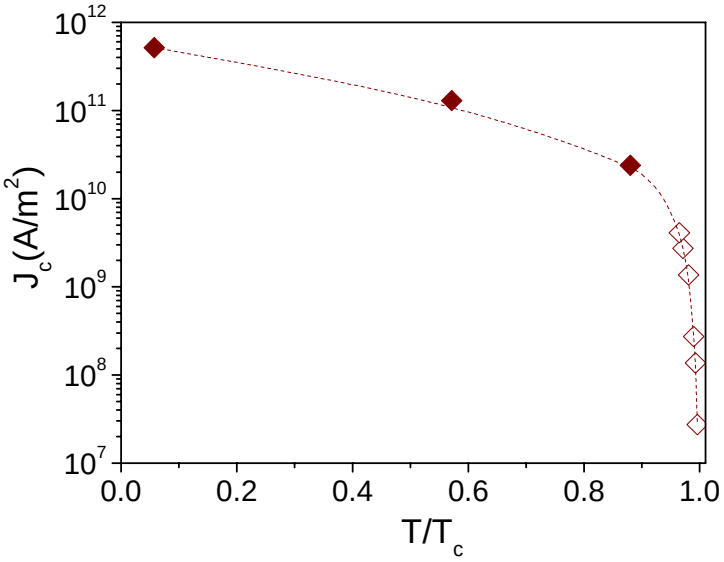

Fig. 6-10. Temperature dependence of the critical current density, $J_c(T)$, determined for the film SCt0.2$_{THEVA}$, from ac-susceptibility data (open symbols) and from dc-magnetization measurements (closed symbols).

6.1.2 THIN FILM GROWN ON A BICRYSTALLINE SUBSTRATE

The ac-susceptibility technique has been largely used in the analysis of granular polycrystalline samples [68,105], since the grain and GB contributions could be identified by the appearance of two peaks in the imaginary component of the ac-susceptibility, θ''. Prior to the study of granular behaviour in coated conductors, we have analyzed a 0.2σm YBCO thin film, grown by PLD on a bicrystalline $SrTiO_3$ substrate with a symmetric 12^o tilt boundary. Thus, we could study which is the ac response in a sample with only one grain boundary. Results are shown in Fig. 6-11.

The large values of θ'ℑ-9500 at low temperatures (5K), clearly reflect that the bicrystal is also affected by strong demagnetizing fields as in the thin film grown on a single crystal analyzed in the previous section. However in the bicrystal, flux penetration and dissipation occur at much smaller fields and temperatures than in the thin film grown on a single crystal. In addition, notice that, for low values of H_{ac}, two peaks may be distinguished at θ'' with values ranging in the order of θ''$_{peak}$ℑ800-1000. The peak appearing at higher temperature has to be ascribed to the dissipation associated to currents flowing inside the grains, which have a higher grain critical current density, J_c^G. The peak appearing at lower temperatures is associated to the flux profile induced with the currents flowing across the full sample and thus crossing the GB, with a lower critical current density, J_c^{GB}. In this case, since we have used a bicrystal with a high angle grain boundary, the dissipation starts at very low temperatures and the dissipation area associated to the low temperature peak depends

strongly on the value of H_{ac} applied. Notice that for low values of H_{ac}, we are able to distinguish the low temperature peak, associated to the GB, although a dissipation tail, associated to areas with low critical current density, appears at low temperatures. If we keep increasing the ac field, we only observe the dissipation tail.

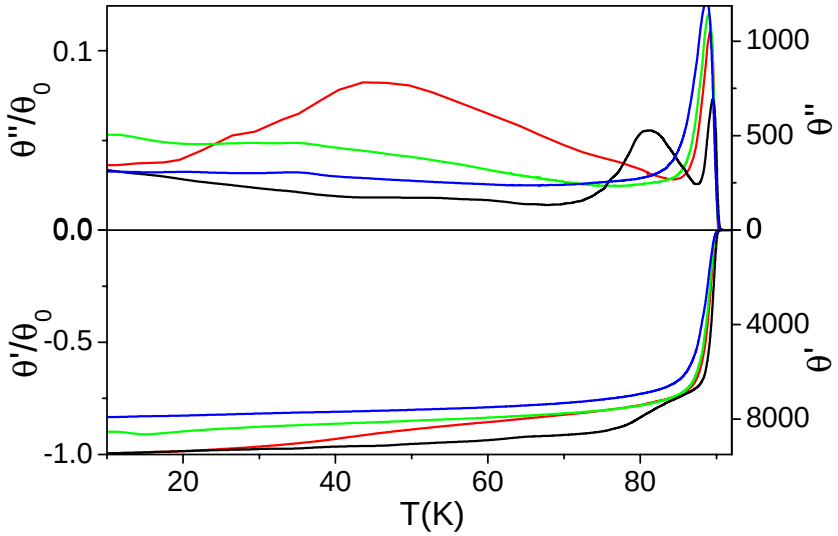

Fig. 6-11. Temperature dependence of the real, θ', and the imaginary, θ'', components of the ac-susceptibility, and the normalized values θ'/θ_0 and θ''/θ_0 for a 12° YBCO bicrystal for $\sigma_0 H_{ac}$=0.01, 0.05, 0.1and 0.2mT at 1111Hz and zero dc applied field.

In general, when the two peaks are sufficiently distant, it is possible to separate the dissipation associated to the grains from that of the GB in the susceptibility curves. So that, at low enough temperatures one can consider total shielding in the grains, i.e. no contribution of the grains in the dissipation losses, whereas at high temperatures, one can assume that the contribution from the GB currents is totally neglected and that all the dissipation losses are associated to the grains. However, this will depend on the grain boundary angle we are analyzing (i.e. on the ratio J_c^{GB}/J_c^{G}).

A very useful plot to identify the two contributions is the parametric plot θ''(θ'). Fig. 6-12 shows the normalized θ''(θ') plot determined from the curves θ'/θ_0(T) and θ''/θ_0 (T), measured at zero dc field and f=1111Hz for different H_{ac}. Two clear peaks can be observed of which θ'' values depend on the H_{ac} field. The peak close to θ'/θ_0=-1 is associated dissipation in the GB whereas that approaching θ'/θ_0=0 to the grain dissipation.

The contribution of the GB dissipation can only be determined at low ac fields, where a peak is distinguished. Considering the curve measured at $\sigma_0 H_{ac}$=0.01mT, we can estimate an effective volume fraction associated to the dissipation at the GB by adjusting the plot $\theta''_{GB}(\theta'_{GB})$ at the peak appearing at low temperature, where,

$$G'_{GB} \mid \; G' / f_{GB} \qquad 6\text{-}1$$

$$G''_{GB} \mid \; G'' / f_{GB} \qquad 6\text{-}2$$

which give us an fraction of f_{GB}=0.24 (dashed line in Fig. 6-12). The remaining fraction would then be associated to dissipation of the grains, f_G=0.76.

A theoretical fit to the peak appearing at high temperatures, is much more difficult to perform, since in this peak we have the contribution of the two grains, and thus the values of θ'_G and θ''_G will depend not only on the volume fraction dissipating at the grains but also on the grain size and on the ratio J_c^{GB}/J_c^{G}. All these considerations make very difficult to find a theoretical fit for the curve $\theta''_G(\theta'_G)$.

Additionally, we observe that the peak appearing at high temperature, keep increasing while we increase the ac magnetic field. This effect can be understood if we consider that at low ac fields the experimental data correspond to a linear response, $H_{ac}<H_{ac}^{l}$, which shows a much smaller dissipation, while by increasing the ac field the vortex dynamics enter in the Bean critical state regime (see section 3.3.3). The onset of the Bean model in this case is very difficult to determine due to the coupling existing between the GB and the grain contributions.

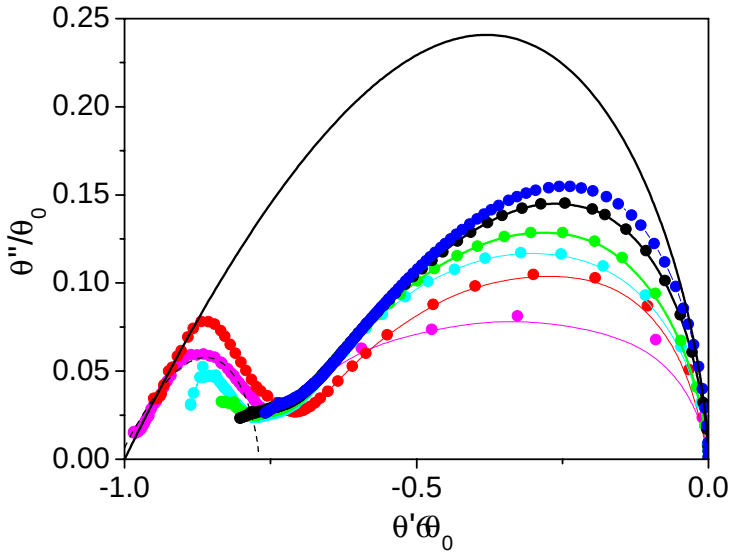

Fig. 6-12. Parametric plot of the complex susceptibility determined for the 12° bicrystal at $\sigma_0 H_{ac}$=0.01, 0.05, 0.1, 0.2, 0.5 and 1.5mT . Solid line shows the behaviour of $\theta''(\theta')$ for a thin disk in the Bean critical state model and dashed line corresponds to the calculated $\theta''_{GB}(\theta'_{GB})$ considering the curve measured at $\sigma_0 H_{ac}$=0.01mT with f_{GB}=0.24.

From the $\theta''(T)$ curves measured at different ac field amplitudes, H_{ac}, the critical current density as a function of the temperature, can be determined according to equation 3-12, i.e. $J_c(T_{peak})=2H_{ac}/1.94t$, since the condition 2R/t>100 is valid

considering all the sample radius or only the grain radius. Fig. 6-13 shows the values of $J_c^{GB}(T)$ and $J_c^{G}(T)$, calculated with the two peaks identified in θ''(T). We have also shown the values of $J_c^{G}(T)$ obtained from magnetic hysteresis loop measurements, by means of equation 4-1, i.e. $J_c=3M_{peak}^{sat}/R$. In this case we can only determine $J_c^{G}(T)$ since the magnetic moment measured in the hysteresis loop corresponds to the magnetic moment of the grains. The magnetic moment associated to the GB currents, which is proportional to J_c^{GB} and to the sample grain size, can be neglected if its compared with the magnetic moment associated to grain currents (proportional to J_c^{G} and grain size) since $J_c^{GB}<<J_c^{G}$ and grain size is comparable to the sample size. Also shown in Fig. 6-13 are the values of $J_c(T)$, determined in the previous section, for the thin film grown on a single crystal, $SCt0.2_{THEVA}$.

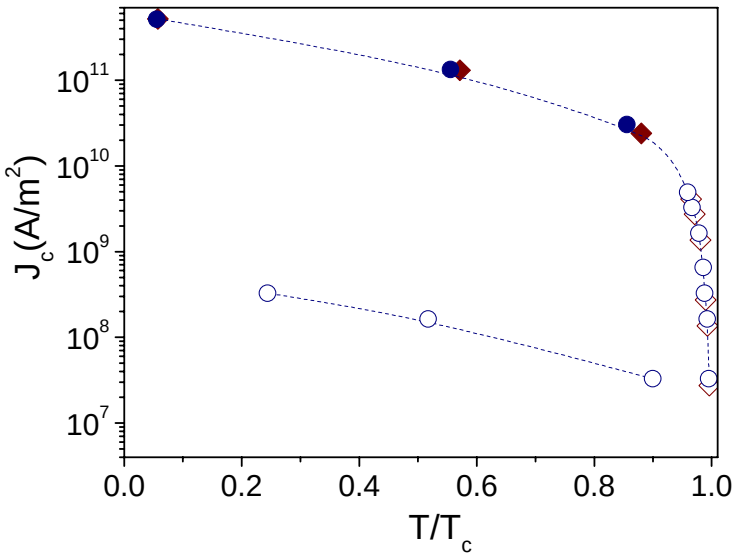

Fig. 6-13. Temperature dependence of the critical current density, J_c, determined from ac-susceptibility data (open symbols) for film $SCt0.2_{THEVA}$ (Ø) and the bicrystal ([1]). For the bicrystal two J_c curves are represented corresponding to J_c^{GB} and J_c^{G}. Also shown are the results obtained from dc-magnetization (closed symbols).

Notice that the values of $J_c^{G}(T)$ obtained for the bicrystal are very similar to those of the $J_c(T)$ values found for the thin film indicating that vortex pinning associated to the grains is very similar for both samples. Additionally, in both cases, the values of $J_c(T)$ determined from ac-susceptibility measurements extrapolate to those calculated from dc-magnetic measurements. A large difference is observed between $J_c^{G}(T)$ and $J_c^{GB}(T)$ determined for the bicrystal (two sets of open circles in Fig. 6-13), $J_c^{GB}/J_c^{G}\cong 0.001$. This ratio is much lower than the expected one for a 12° bicrystal which is about $J_c^{GB}/J_c^{G}\cong 0.05$ (see Fig. 5-16) indicating that this is a bicrystal with degraded grain boundary.

6.2 AC-SUSCEPTIBILITY STUDY OF COATED CONDUCTORS

In the previous section, we have seen that it is possible to identify the contribution of both grain and grain boundary critical currents in a bicrystaline thin film, by means of ac-susceptibility measurements. In this section we will discuss the analysis of ac-susceptibility response of coated conductors, which will allow us to study the dissipation and dynamic regimes, associated to the grain boundary networks present in these materials and which will complement the magnetic granularity study presented in the previous chapters.

6.2.1 A MODEL COATED CONDUCTOR WITH A HOMOGENEOUS GRAIN BOUNDARY NETWORK

We will first analyze the results obtained for a model IBAD coated conductor, IBADt0.23$_{Gott}$, which consists of a 0.23σm YBCO film deposited by PLD on a CeO_2 buffered IBAD-YSZ layer grown on a polycrystalline YSZ substrate, with ÷λ=8º. This CC presents a homogeneous distribution of low angle grain boundaries, as it has been identified by magneto-optic studies.

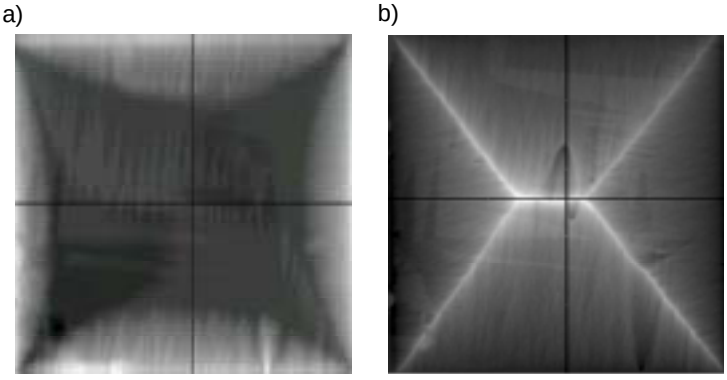

Fig. 6-14. Flux distribution obtained for IBADt0.23$_{Gott}$ at 9K, after ZFC the sample and applying a dc field of $\sigma_0 H_a$=13.2mT (a) and in the remanent state after applying a maximum field of 260mT (b).

We present in Fig. 6-14 two MO images of the IBADt0.23$_{Gott}$ performed during my stay in the "Zentrum für FunktionWekstoffe" of Gottingen. Fig. 6-14a) shows the flux penetration (light zone) obtained after ZFC the sample to T=9K and applying a dc field, $\sigma_0 H_a$=13.2mT. A sharply defined flux front is detected similar to that observed for a thin film [56]. Fig. 6-14b) shows the magnetic flux distribution in the remanent state at T=9K. In those images, no granularity can be detected because in an IBAD CC the grain size is of the order of the MO resolution (ℑ5σm). The light zones observed in the

centre of the sample in Fig. 6-14a) correspond to different domains of the indicator film used.

Results of ac-susceptibility curves measured for IBADt0.23$_{Gott}$ are shown in Fig. 6-15. Notice that the obtained curves are very similar from those already shown for the film SCt0.2$_{THEVA}$ grown on a SC. At low temperatures θ'/θ_0=-1 and the peak value $\theta''_{peak}/\theta_0 \Im 0.24$ when the sample radius is used to calculate θ_0. This evidences that flux penetrates from the surface till the centre of the sample following the critical-state model as it has been observed in the MO study. However, flux penetrates, dissipates and θ'' peaks at lower temperatures than in SCt0.2$_{THEVA}$ film, which indicates that the critical-current density is smaller in agreement with a $\div\lambda$=8º, in the coated conductor. Notice that in the coated conductor, contrary to what happened for the bicrystal, we are not able to detect the peak associated to the dissipation in the grains, since the grain size is much smaller than the sample size and the dissipation associated to the grains gives a negligible signal in the θ''(T) curve compared with the signal associated to the GB currents.

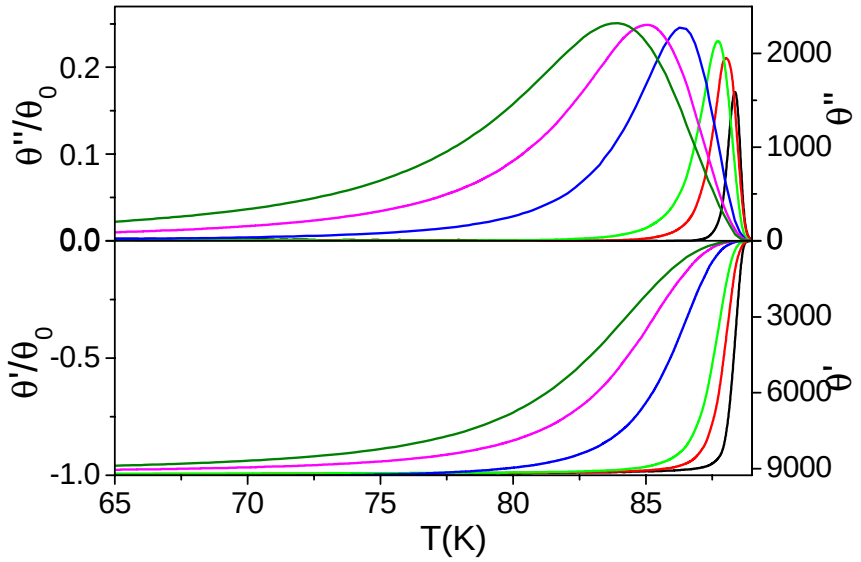

Fig. 6-15. Temperature dependence of the real, θ', and the imaginary, θ'', components of the ac-susceptibility, and the values normalized to its Meissner slope, $\theta'(T)/\theta_0$ and $\theta''(T)/\theta_0$ for IBADt0.23$_{Gott}$ for $\sigma_0 H_{ac}$=0.01, 0.05, 0.1, 0.5, 1 and 1.5mT at 1111Hz and zero dc applied field.

Some theoretical values of θ''_{peak}, calculated for cylinders of different aspect ratio, 2R/t, where R is the radius of the current penetrated region and t the film thickness, are presented in Table 6-1. These values have been calculated by A. Sánchez et al. [111], thanks to our collaboration with the Universitat Autònoma de Barcelona, using a numerical model based on energy minimization which was

presented in[62,65]. For the IBAD coated conductor analyzed, we have an average grain radius of about 0.5-1σm and a thickness of 0.23σm, so that, the expected θ''_{peak} value determined from Table 6-1 is θ''_{peak}≈0.5, which is clearly negligible compared with the experimental values measured in the θ''(T) curves associated to the GB currents, which are in the range of θ''_{peak}≈2000

2R/t	θ''_{peak}
0.1	0.211
0.25	0.228
5	0.697
8	1.00
10	1.20
100	10.3
200	20.4
500	50.9
1000	102
2000	204
5000	509

Table 6-1. Values of the maximum value of θ'', θ''peak, calculated for cylinders of different cylinder aspect ratios, 2R/t.

In fact, since flux penetrates through the grain boundaries till reaching the centre of the sample following a critical-sated model, only from ac-susceptibility measurements we cannot distinguish penetration through a GB network from penetration through a single crystalline film. In other words, flux penetration through a homogeneous GB network behaves qualitatively similarly to a single crystalline material though penetration and dissipation occurs at lower temperatures and ac fields.

Fig. 6-16 shows the parametric plot θ''(θ') obtained for the coated conductor $IBADt0.23_{Gott}$ (closed symbols) compared with the one obtained for the non-granular thin film $SCt0.2_{THEVA}$, analyzed in section 6.1.1 (open symbols) at H_{ac}=0.5mT. The two curves are almost identical indicating that, when flux penetrates in a granular film through a homogeneous grain boundary network, describing a general critical state in the whole sample, the parametric plot θ''(θ'), is the same than that obtained for a non-granular thin film.

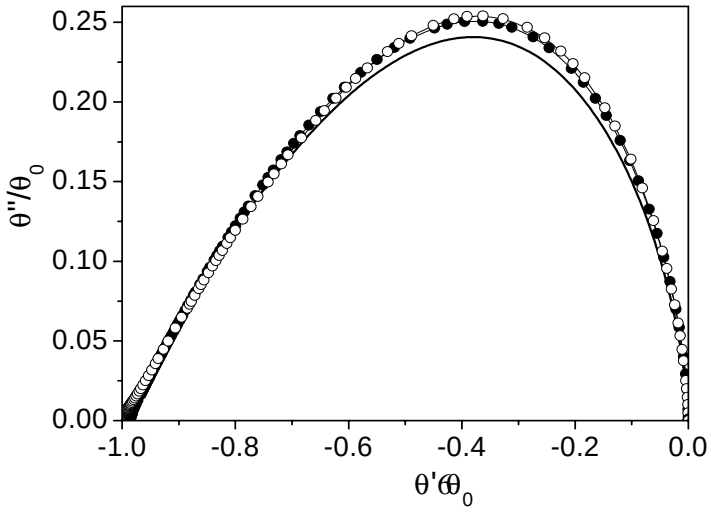

Fig. 6-16. . Parametric plot of the complex susceptibility determined from the θ'(T) and θ''(T) curves for IBADt0.23$_{Gott}$ (¸), compared with the plot obtained for the film SCt0.2$_{THEVA}$ (¹), measured at H_{ac}=0.5mT. Solid line shows the behaviour of θ''(θ') for a thin disk in the Bean critical state model.

Fig. 6-17 shows the curves J_c(T) determined for the model coated conductor, IBADt0.23$_{Gott}$, and for the YBCO thin film grown on a single crystal, SCt0.2$_{THEVA}$, determined from ac measurements (open symbols) and from dc-magnetic hysteresis loops (closed symbols). As in the other examples shown in the previous sections, the values of J_c(T) determined from ac-susceptibility measurements extrapolate to those calculated from dc-magnetic measurements.

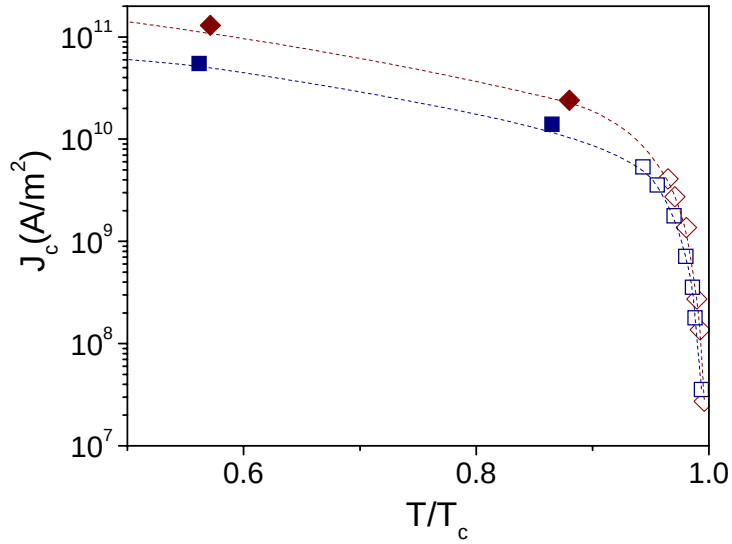

Fig. 6-17. Temperature dependence of the critical current density, J_c, determined from ac-susceptibility data (open symbols) for film SCt0.2$_{THEVA}$ (Ø) and the IBADt0.23$_{Gott}$ (Ã). Also shown are the results obtained from dc-magnetization (closed symbols).

The values of critical current density obtained for the film SCt0.2$_{THEVA}$ are higher than the values measured for sample IBADt0.23$_{Gott}$, since in the second case we are measuring the currents that flow through the GB network, in agreement with the in-

plane texture of ÷λ=8º, for the IBADt0.23$_{Gott}$ sample in which case we are measuring the currents that flow through the GB network.

6.2.2 COATED CONDUCTORS WITH DISTINCT GRAIN BOUNDARY NETWORKS

We further proceed by analyzing the ac-susceptibility response of different coated conductors grown on top of metallic substrates, with less homogeneous grain boundary networks. We will see with the following examples the unique capabilities of ac-susceptibility to analyze the distinct superconducting properties of different performed coated conductors.

Fig. 6-18 shows the real and imaginary components of the ac-susceptibility, θ' and θ'', measured for the IBAD CC, IBADt1.6a$_{Gott}$. This sample consists of a 1.6σm thick YBCO film grown by PLD on a non-magnetic Ni-Cr stainless steel tape buffered with a textured YSZ layer, with ÷λ| 12.7º. Upon comparison of the IBAD coated conductor signal with the one obtained for an IBAD substrate without the YBCO layer, we confirmed that subtraction of the substrate signal was not required in ac-susceptitibilty curves.

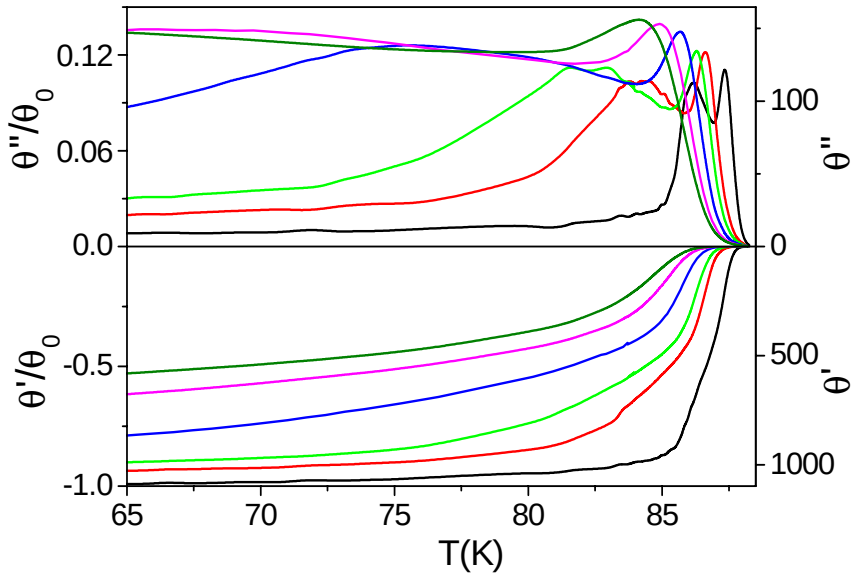

Fig. 6-18. Temperature dependence of the real, θ', and the imaginary, θ'', components of the ac-susceptibility, and the values normalized to its Meissner slope, θ'(T)/θ$_0$ and θ''(T)/θ$_0$ for IBADt1.6a$_{Gott}$ at σ$_0$H$_{ac}$=0.01, 0.1, 0.2, 0.5, 1 and 1.5mT at 1111Hz.

Results clearly reflect that the conductor is also affected by strong demagnetizing effects, θ'(5K)ℑ -1100. Notice that dissipation occurs in the conductor at much smaller fields and temperatures than for the previous model coated conductor analyzed, IBADt0.23$_{Gott}$. In addition, θ''(T) presents two peaks with θ''$_{peak}$ values of 130-

150. We have seen, in the previous section, that in a coated conductor the peak associated to the dissipation in the grains is negligible in the θ''(T) curve since the grain size is much smaller than the sample size. The observed experimental values of θ''_{peak} in the θ''(T) curves are about $\theta''_{peak}\Im$130-150, for both peaks, so that, according to the calculated values of θ''_{peak} shown in Table 6-1, the radius of the region associated to the dissipation of these peaks is about R$\Im$1mm (2R/t$\Im$1500 and t=1.6σm). Hence, we can say that for the coated conductor, the dissipation measured in both peaks appearing in the θ''(T) curve have to be associated to the currents flowing through all the sample, and not to the currents flowing inside the grains.

The presence of two peaks in the θ'' curve would indicate that in this coated conductor, two different critical state profiles can be established at different temperatures and thus, that the conductor is composed of two different grain boundary networks with different critical current densities. Fig. 6-19 shows a schematic representation of flux penetration for this particular situation where red colour represents flux penetration through low-J_c grain boundaries and green colour penetration through high-J_c grain boundaries. At low temperature, flux starts to penetrate through low-J_c grain boundaries forming a branching 2D network of penetrated flux that generates a critical-state profile through a certain area (Fig. 6-19a). When flux cannot further penetrate into the sample through these low angle grain boundaries, either because a separated domain has been formed or because any further penetration through the GB network would imply penetration via high-J_c grain boundaries, θ'' peaks (Fig. 6-19b). Upon increasing temperature, a second flux profile is induced, from the surface to the centre of the sample, with currents crossing GBs of higher J_c and a second peak of θ'' is generated (Fig. 6-19c). The two strongly different GB contributions may be associated to GB networks of different angle or different quality and consequently different J_c(T).

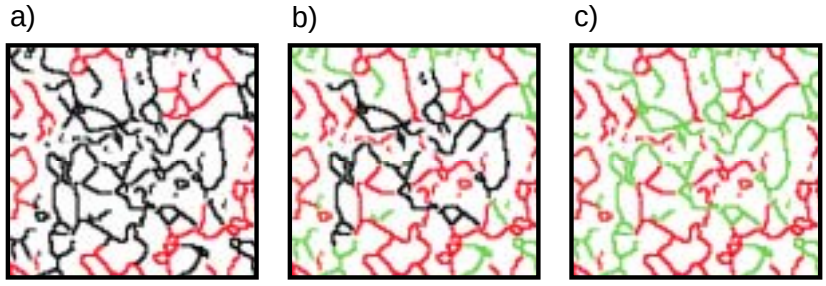

Fig. 6-19. Schematic representation of flux penetration through a coated conductor with two different GB networks of different critical current densities. In red it is shown flux penetration through low-J_c GBs and in green penetration through high-J_c GBs.

For the coated conductor that we have analyzed, IBADt1.6a$_{Gott}$, we can calculate the two $J_c(T)$ curves, associated to the different critical states profiles established in the conductor at different temperatures, analyzing the two peaks identified in the curves θ''(T), measured at different ac fields. Since the condition 2R/t>100, is accomplished for both peaks, we can use equation 3-12, $J_c(T_{peak})=2H_{ac}/1.94t$, in order to determine the two $J_c(T)$ curves. Results are shown in Fig. 6-20 (open circles), compared with the $J_c(T)$ curve obtained for a YBCO film grown on a single crystal, SCt0.2$_{THEVA}$ (open diamond). We have also presented the $J_c(T)$ curves obtained by dc-magnetization measurements (closed symbols). Notice that, for the sample IBADt1.6a$_{Gott}$, the J_c curve with the higher values of J_c is that which extrapolates to the dc-magnetization measurements, which corresponds to $J_c^{GB}(T)$ (see section 4.2.3). This result confirms then, that at that temperature, the induced currents percolate through the GB network and they do generate a critical state profile. Thus, the conductor is composed of two different grain boundary networks with one order of magnitude different J_c. We see, that in transport or magnetic measurements only the highest J_c percolative domain can be detected whereas other domain networks which still generate important ac dissipation in the conductor are invisible. The ac-susceptibility technique, able to identify all these J_c inhomogeneity distribution, is then a very useful technique for the study of dissipation in granular coated conductors.

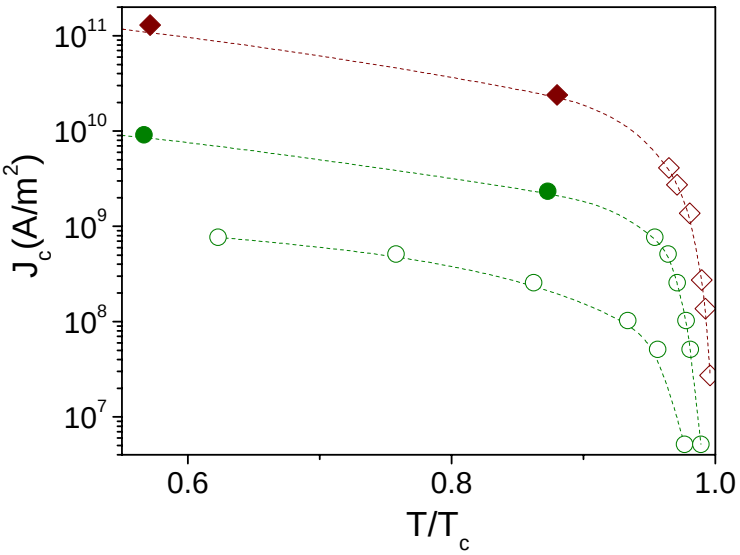

Fig. 6-20. Temperature dependence of the critical current density, J_c, determined from ac-susceptibility data (open symbols) for the film SCt0.2$_{THEVA}$ (Ø) and the CC IBADt1.6a$_{Gott}$ ([1]). For the sample IBADt1.6a$_{Gott}$, two J_c curves arising from two peaks observed in θ''(T) are represented. Also shown are the results obtained from dc-magnetization (closed symbols).

Further information about the effective flux penetration area associated to each grain boundary network can be obtained by means of the parametric plot θ''(θ'). Since

the dissipation area associated at each peak strongly depends on the value of the applied H_{ac}, we will use the minimum value of H_{ac} which induce a critical state regime in the sample, for determining the dissipation plot θ''(θ'). The onset of the Bean critical state regime has been determined by means of the methodology described in section 3.3.3. Fig. 6-21 shows Bean length, Θ_c, determined for IBADt1.6a$_{Gott}$, as a function of $\sigma_0 H_{ac}$, where we have indicated with arrows the onset of the Bean regime at different temperatures. We observe that a Bean critical state regime is developed for ac fields higher than, $\sigma_0 H_{ac}$=0.2mT, and thus this is the value that we have used for determining the parametric plot θ''(θ').

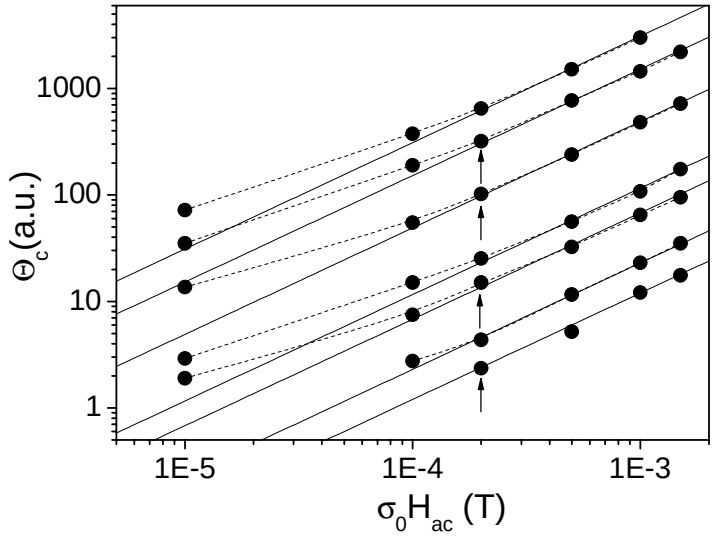

Fig. 6-21. Bean length, Θ_c, as a function of the field amplitude at different temperatures, T=85K, 84.5K, 84K, 82K, 80K, 70K, 50K, from top to bottom. Some of the points which describe the onset of the Bean regime are indicated.

Fig. 6-22 shows the normalized θ''(θ') plot obtained for the film IBADt1.6a$_{Gott}$ at H_{ac}=0.2mT. In this case, the two peaks are coupled since the dissipation associated to the high temperature peak starts when the other peak is still dissipating. We will determine the contribution associated to percolative currents with high J_c (high temperature peak) with an the effective volume fraction, f_1, by means of

$$G'_{peak1} \mid G'/f_1 \qquad 6\text{-}3$$

$$G''_{peak1} \mid G''/f_1 \qquad 6\text{-}4$$

and the contribution associated to the currents with low J_c (low temperature peak), with a volume fraction, f_2, using

$$G'_{peak2} \mid G'/f_2 \qquad 6\text{-}5$$

$$G''_{peak\,2} \mid G''/f_2 \qquad 6\text{-}6$$

With these equations and from the theoretical plot θ''(θ') simulated for a thin disk in the Bean critical state model (see Fig. 3-9), we can establish the theoretical curves expected for the two peaks appearing in the experimental curve θ''(θ'). Thus, with the values f_1 and f_2 as free parameters, we can determine $\theta''_{peak1}(\theta'_{peak1})$ and $\theta''_{peak2}(\theta'_{peak2})$. Solid line shown in Fig. 6-22 represents the theoretical curve expected for a coated conductor with homogeneous GB network, while the dashed lines are fitting plots for the two peaks associated to different GB networks with f_1≈0.5 and f_2≈0.45. Thus, we have obtained that two regions of similar dimensions, but with different critical current density, dissipate in the sample.

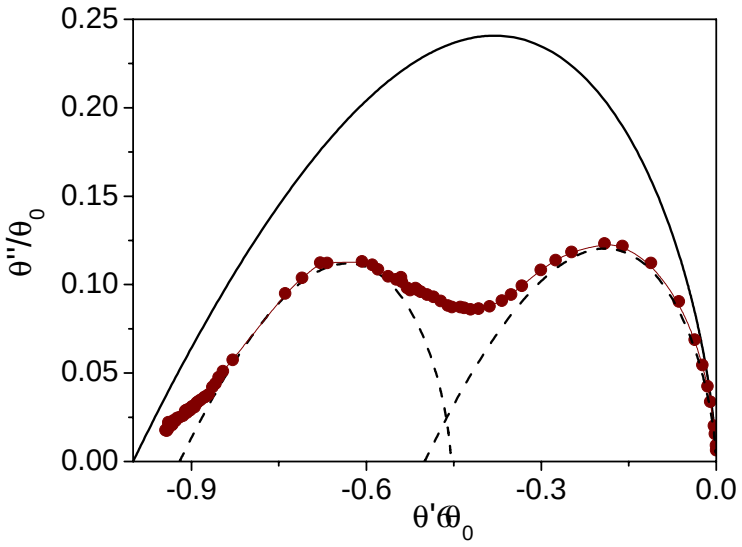

Fig. 6-22. Parametric plot of the complex susceptibility determined for IBADt1.6a$_{Gott}$ at $\sigma_0 H_{ac}$=0.2mT. Solid line shows the behaviour of θ''(θ') for a thin disk in the Bean critical state model and dashed lines correspond to the θ''(θ') curves calculated for the two dissipation peaks associated to different critical currents.

Additionally, we have analyzed another IBAD sample, IBADt1.6b$_{Gott}$, grown by PLD on a non-magnetic Ni-Cr stainless steel tape buffered with a textured YSZ layer, with t=1.6σm and ÷λ¦ 17.2º. Fig. 6-23 shows the temperature dependence of θ' and θ'' measured for IBADt1.6b$_{Gott}$ at different ac fields. In this case, only one peak is observed in the θ''(T) curve, though a long dissipative tail is present at low temperatures, even at low fields. Thus, this sample is composed of one main grain boundary network in agreement with the single peak in θ''(T), and a distribution of small size HAGB domains, as exemplified by the non-zero value of θ''(T) at low temperatures.

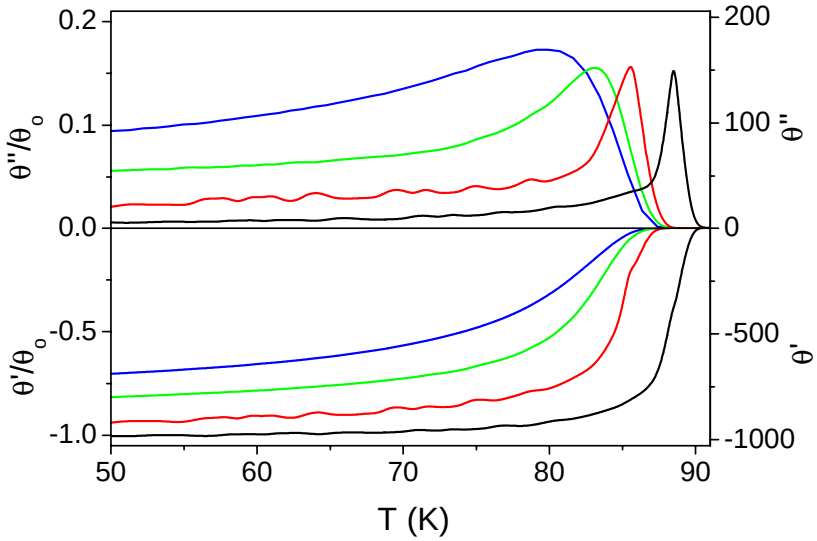

Fig. 6-23. Temperature dependence of the real, θ', and the imaginary, θ'', components of the ac-susceptibility, and the values normalized to its Meissner slope, $\theta'(T)/\theta_0$ and $\theta''(T)/\theta_0$ for IBADt1.6b$_{Gott}$ for $\sigma_0 H_{ac}$=0.01, 0.1, 0.5 and 1mT at 1111Hz.

In order to better analyze the dissipation in the sample, we have used the parametric plot θ''(θ') presented in Fig. 6-24. The effective volume fraction associated to the main grain boundary network that generates a critical state profile, have been determined by adjusting equation 6-7 at the experimental values, which gives f=0.65.

$$G'_{peak} \mid G'/f \qquad 6\text{-}7$$

The remaining fraction, (1-f)=0.35, is that associated to the small domains which induce the ac losses appearing at low temperature.

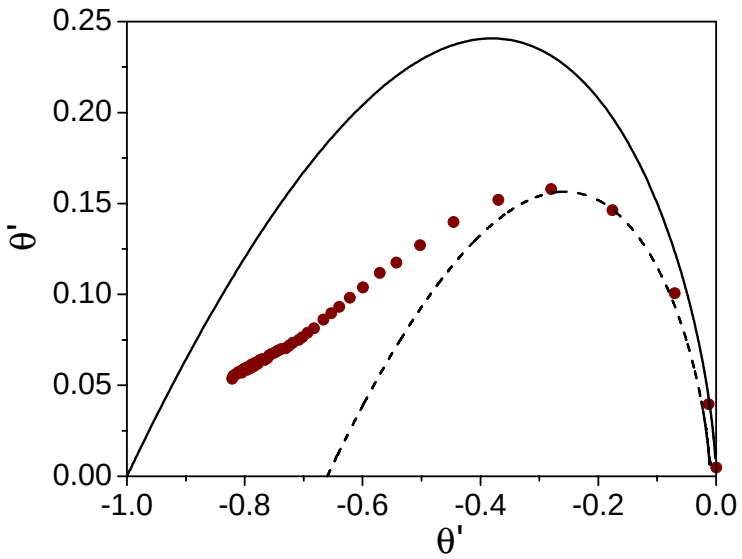

Fig. 6-24. Parametric plot, θ''(θ'), determined for IBADt1.6b$_{Gott}$ at $\sigma_0 H_{ac}$=0.5mT. Solid line shows the behaviour of θ''(θ') for a thin disk in the Bean critical state model and dashed line correspond to the fitting curve θ''(θ') calculated for the main dissipation peak.

From the θ''(T) curves shown in Fig. 6-23 we have determined the values of J_c(T) by means of equation 3-12 and we have compared the results obtained with the ones presented in Fig. 6-20 for the coated conductor, IBADt1.6a$_{Gott}$, and for the thin film grown on a single crystal, SCt0.2$_{THEVA}$ (Fig. 6-25). The values of critical current density obtained for the film SCt0.2$_{THEVA}$ are higher than the values measured for both coated conductors in agreement with the reduced texture quality associated to the coated conductors, ÷λ| 12.7º and 17.2º for IBADt1.6a$_{Gott}$, and IBADt1.6b$_{Gott}$, respectively.

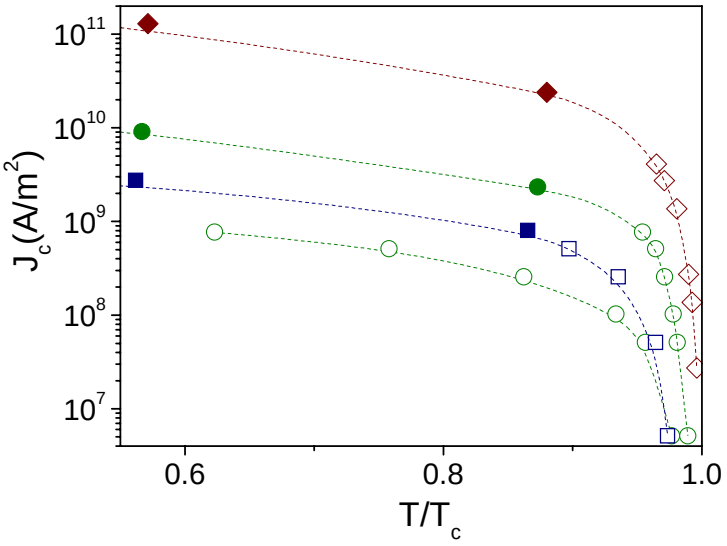

Fig. 6-25. Temperature dependence of the critical current density, J_c, determined from ac-susceptibility data (open symbols) for the film SCt0.2$_{THEVA}$ (Ø) and the CCs IBADt1.6a$_{Gott}$ (¹) and IBADt1.6b$_{Gott}$ (Ã). Also shown are the results obtained from dc-magnetization (closed symbols).

The same ac analysis has also been realized in several RABiTS samples. In this case, the signal coming from the nickel substrate has to be considered since, although it is much lower than the superconductor signal, it is not negligible. To do that, we have used the same procedure than in the magnetization measurements (see section 4.2.1), and we have removed the signal measured at 100K in all the curves.

Fig. 6-26 shows the ac-susceptibility data measured for the sample RABt1.08$_{ORNL-A}$, which consists of a 1.1σm thick YBCO film grown by ex situ conversion of BaF_2-based precursors on a Ni-W substrate, with an excess of liquid formation during the process (see section 5.1.1) and with ÷λ| 5.3^o. It has been observed, by dc-magnetic measurements (see section 5.1.1) that, in these conditions, large grains are formed in the coated conductor overgrowing the substrate grain boundary network, and the samples present a lower GB critical current density, J_c^{GB}(77K)=6.1.10^{9}A/m^2, than those grown by the optimum parameters. Notice that, for this particular sample, we can

even distinct three different dissipation peaks, indicating that when the grain boundary network does not replicate the substrate pattern, a non homogenous distribution of grain boundaries with different J_c is favourable, forming networks of different performances.

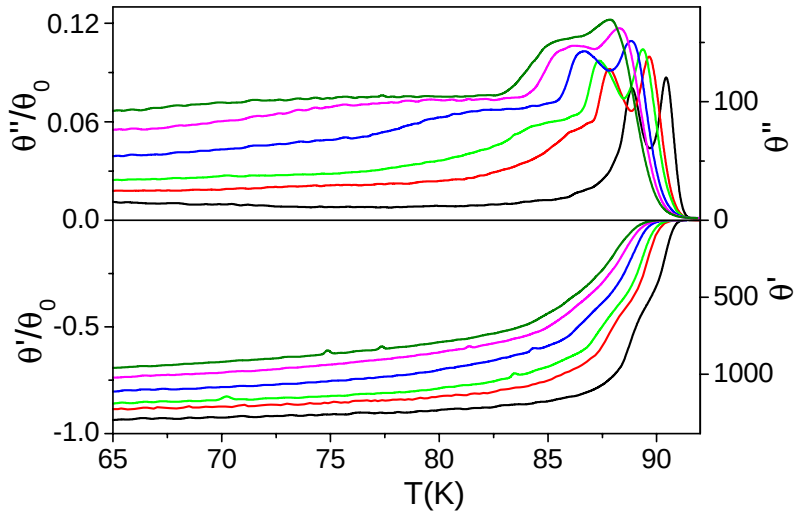

Fig. 6-26. Temperature dependence of the real, θ', and the imaginary, θ'', components of the ac-susceptibility, and the values normalized to its Meissner slope, θ'(T)/θ0 and θ''(T)/θ0 for RABt1.08ORNL-A for σ0Hac=0.01, 0.1, 0.2, 0.5, 1 and 1.5mT at 1111Hz.

The parametric plot θ''(θ') determined at $\sigma_0 H_{ac}$=0.2mT has been represented in Fig. 6-27. We have used equation 6-7 in order to adjust the three peaks appearing in the θ''(θ') curve. The effective volume fractions, that we have obtained are f≅0.4 for the two peaks appearing at high temperature and f≅0.2 for the peak located at low temperature. So that, the effective volume associated to the high critical current density is only a 40% of the sample.

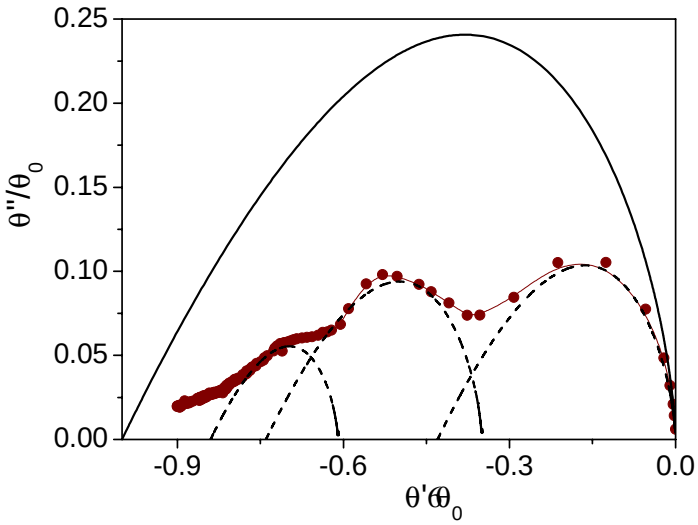

Fig. 6-27 Parametric θ''(θ') plot determined at σ0Hac=0.2mT for RABt1.08ORNL-A. Solid line shows the behaviour of θ''(θ') for a thin disk in the Bean critical state model and dashed lines are fitting θ''(θ') plots for the three different peaks.

For comparison purposes, we have analyzed another RABiTS sample, RABt1.41$_{ORNL-C}$, consisting of a 1.4σm YBCO layer grown on the same Ni-W substrate, with an optimized process which produces a grain structure replicating the underneath substrate (see section 5.1.1). This sample present a higher J_c^{GB}(77K)=1.6.10^{10}A/m^2, than the previous one. Fig. 6-28 Shows the parametric plots determined for both samples at $\sigma_0 H_{ac}$=0.2mT. Notice that for the sample grown with the optimum process we only detect one dissipation peak with an effective volume fraction of f=0.9, and thus a better homogeneity of the GB network is observed. In general, we have found that for the most homogeneous samples we obtain high GB critical current densities.

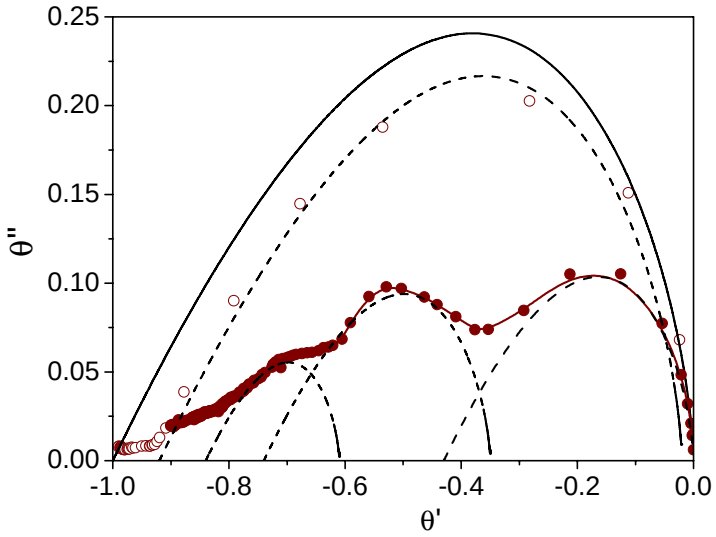

Fig. 6-28. Parametric θ''(θ') plots determined at $\sigma_0 H_{ac}$=0.2mT for RABt1.08$_{ORNL-A}$ (closed symbols) and RABt1.41$_{ORNL-C}$ (open symbols). Solid line shows the behaviour of θ''(θ') for a thin disk in the Bean critical state model and dashed lines are fitting plots, θ''(θ'), of he experimental data.

The determination and understanding of microstructural mechanisms leading to the appearance of these distinct-boundary networks domains is particularly important for the development of coated conductors in an industrial scale. In particular, we have seen that it is possible to induce the formation of grain boundary networks with different J_c when the conductor is mechanically deformed (see section 5.4)

Finally, Fig. 6-29 shows the real and imaginary components of ac-susceptibility measured at $\sigma_0 H_{ac}$=0.2mT for the IBAD coated conductor IBADt1$_{Gott}$ as it has been grown (solid lines) and after four consecutive bending test, with induced deformations of κ=0.32%, κ=0.4% and 0.62%, described in section 5.4 (dashed lines).

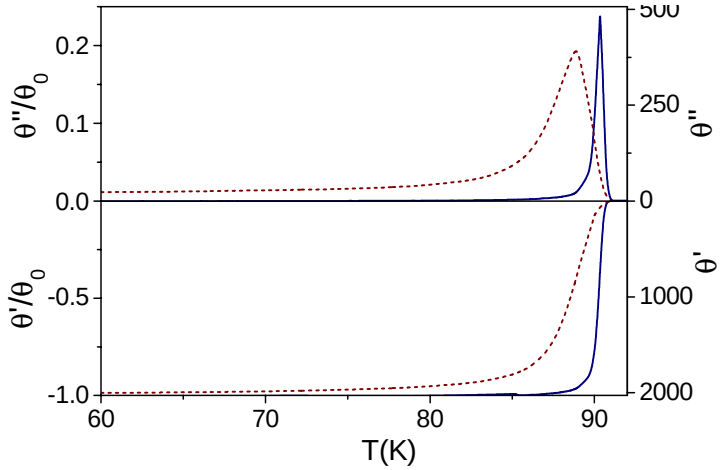

Fig. 6-29 Temperature dependence of the real, θ', and the imaginary, θ'', components of the ac-susceptibility, and the values normalized to its Meissner slope, θ'(T)/θ0 and θ''(T)/θ0 for IBADt1Gott before bending test (solid line) and after four consecutive bendings with induced deformations of κ=0.32%, κ=0.4% and 0.62% (dashed line) for σ0Hac=0.05mT at 1111Hz.

In the first measurement, before any bending, the ac-susceptibility curves are very similar from those previously shown for a coated conductor with homogeneous grain boundary network (see Fig. 6-15). At low temperatures θ'/θ_0=-1 and the peak value $\theta''_{peak}/\theta_0 \Im 0.24$. So that, one can assume that before bending the coated conductor presents a homogeneous grain boundary distribution.

After bending tests, the peak is located at lower temperatures, which implies a decrease in the percolative critical current density, in agreement to that observed by dc-magnetization measurements in section 5.4. Although only one peak is observed in θ''(T), a long dissipative tail is formed at low temperatures and θ''_{peak} is lower than the 0.24 expected value for homogeneous GB networks. This result evidences that after bending only a fraction of the whole sample dissipates at the peak. The remaining fraction should be associated with the dissipation tail observed at lower temperatures coming from small areas which have been damaged during the bending process forming sub-networks with a large distribution of J_c. So that, the tail could be considered, as an envelop of many θ''(T) peaks at different temperatures. In order to estimate the effective fraction of the sample which contributes to the dissipation at the peak, we have determined the parametric plot, θ''(θ'). Fig. 6-30 shows the values of θ''(θ') obtained for the sample $IBADt1_{Gott}$ before and after bending test at $\sigma_0 H_{ac}$=0.2mT. The effective volume fractions that we have obtained adjusting equation 6-7 at the experimental values are f=0.95 before the bending and f=0.8 after the bending. In the later case the fit has been performed considering only the dissipation at high

temperatures since at low temperatures we have the contribution of dissipation associated to damaged zones which occupy a 20% of the sample volume.

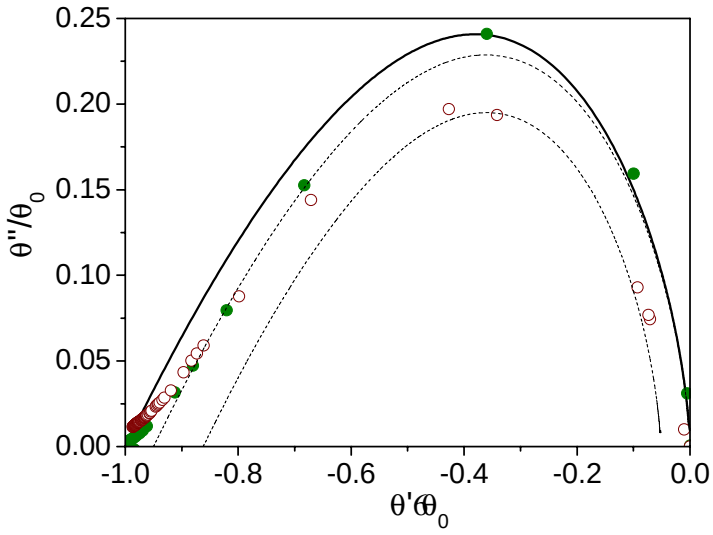

Fig. 6-30. Parametric θ''(θ') plots determined at $\sigma_0 H_{ac}$=0.2mT, for the coated conductor IBADt1$_{Gott}$, before bending (closed symbols) and after four consecutive bendings with induced deformations of κ=0.32%, κ=0.4% and 0.62% (open symbols). Solid line shows the curve θ''(θ') determined for a thin disk in the Ban critical state model while dashed lines are fitting plots θ''(θ') of the experimental data.

With all the analysis performed in this section, we have shown that the ac-susceptibility of YBCO IBAD coated conductors present a rich phenomenology where different GB networks are the sources of different critical-current densities that can be detected and evaluated.

6.3 DETERMINATION OF DYNAMIC PHASE DIAGRAMS AND IRREVERSIBILITY LINES OF YBCO COATED CONDUCTORS

We have determined the dynamic phase diagram of vortex motion in YBCO coated conductors with different GB network homogeneities and compared the obtained results with the phase diagram determined for a YBCO thin film grown on a single crystal, shown in Fig. 6-5.

The crossover from a linear response, appearing at low magnetic fields, to a nonlinear regime, H_{ac}^{l}, has been determined by analyzing the dependence of θ' with the ac magnetic field. Fig. 6-31 shows the values of θ'/θ_0 as a function of the ac magnetic field, obtained for a coated conductor with a homogeneous GB network, IBADt0.23$_{Gott}$, (see section 6.2.1) at different temperatures. We have indicated with arrows the values of H_{ac}^{l}, found at 87K and 75K. The curve, H_{ac}^{l}(T), determined at different temperatures is shown in Fig. 6-32. Similar curves have been generated for a

non homogeneous coated conductor IBADt1.6a$_{Gott}$, which presented two dissipation peaks at the θ''(T) curve (section 6.2.2). The values of H_{ac}^{I}(T) obtained for this sample have also been represented in the phase diagram of Fig. 6-32.

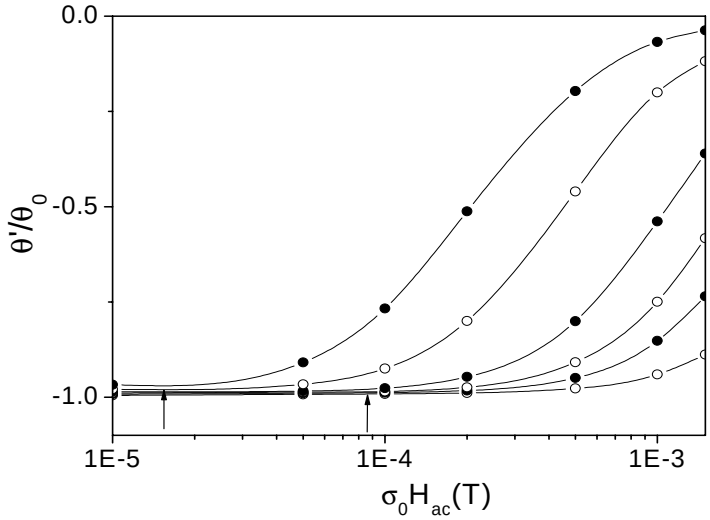

Fig. 6-31. θ' component of the ac-susceptibility as a function of the ac field obtained for the sample IBADt0.23$_{Gott}$, for zero dc field at different temperatures , T=87K, 86K, 84K, 82K, 80K, 75K, from top to bottom. Some of the points which describe the crossover to a linear response, $\sigma_0 H_{ac}^{I}$(T), are indicated.

Moreover, we have determined the onset of the Bean critical state regime, $\sigma_0 H_{ac}^{c}$(T), also indicated in the phase diagram, by means of the methodology described in section 3.3.3. Fig. 6-21 shows some of the obtained values for the sample IBADt1.6a$_{Gott}$, at different temperatures. The transitions $\sigma_0 H_{ac}^{c}$(T) and $\sigma_0 H_{ac}^{I}$(T), found for the two CC, IBADt0.23a$_{Gott}$ and IBADt1.6a$_{Gott}$, are shown in Fig. 6-32 together with those obtained for the non-granular film SC SCt0.2$_{THEVA}$.

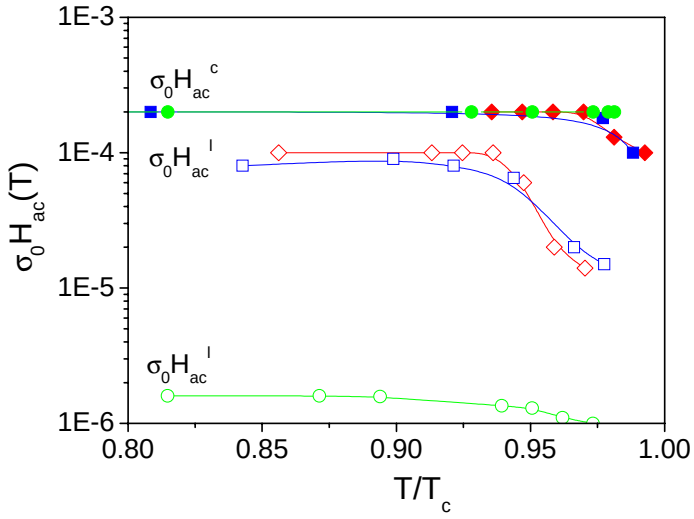

Fig. 6-32. Dynamic phase diagram, $\sigma_0 H_{ac}$ vs. T/T_c, determined for a YBCO thin film grown on a single crystal, SCt0.2$_{THEVA}$ (diamond), and for two different coated conductors, an homogenous one, IBADt0.23$_{Gott}$ (square) and a non homogeneous, IBADt1.6a$_{Gott}$ (circles), with f=1111Hz and zero dc applied field. Open symbols corresponds to $\sigma_0 H_{ac}^{I}$(T) and closed symbols to $\sigma_0 H_{ac}^{c}$(T).

Comparing the different regions obtained, we observe that the onset of the Bean critical state regime, $\sigma_0 H_{ac}^{c}(T)$, is almost the same for the two coated conductors and it coincides with the one found for the YBCO thin film grown on a single crystal. However, notice that a clear difference is observed in the $\sigma_0 H_{ac}^{l}(T)$ lines. For the YBCO coated conductor with homogeneous grain boundary network, $IBADt0.23_{Gott}$, we have obtained a similar $\sigma_0 H_{ac}^{l}(T)$ curve than for the non-granular YBCO thin film, $SCt0.2_{THEVA}$, but for the non homogeneous coated conductor $IBADt1.6a_{Gott}$, we clearly observe that the non linear regime occurs at much lower ac magnetic fields. So that, the region where a non linear regime occurs, is much extended for the non homogeneous coated conductor.

We note therefore that, the dissipation regimes governing the AV may also account for the dissipation of AJV at the GB dislocations and that even similar driving forces might be required to go from one regime to the other if the CC is of the best quality. For the non homogeneous coated conductor, $IBADt1.6a_{Gott}$, which presented two GB networks with different J_c^{GB}, we clearly observe that the transition from linear to non linear regime is very much decreased, indicating that in the regions where the AJV are less pinned (regions with low J_c^{GB}) an inter-valley motion occurs with very low driving forces. Instead, the transition to the critical state regime needs larger applied ac fields, similar to those needed for a non-granular film, since in this case it is necessary an intra-valley global motion of all the AJVs, i.e. vortex associated to the low and high J_c^{GB}. For this particular coated conductor, since there are some regions of the sample with high critical current density (associated to the high temperature peak), the large driving forces required to enter all the vortices into the Bean critical state regime may induce motion of both AV and AJV. This would indicate that at the high temperatures where we are performing the analysis we are in the region III described in section 5.3.2.c already at very low magnetic fields. Thus, the onset to the Bean critical state regime occurs at similar values $\sigma_0 H_{ac}^{c}(T)$ for the CC than for the non-granular thin films.

From the evolution of the ac-susceptibility peaks measured at different dc-magnetic fields superimposed to a fixed ac field of $\sigma_0 H_{ac}$=0.01mT, we have determined the irreversibility line for the coated conductors $IBADt0.23_{Gott}$ and $IBADt1.6a_{Gott}$. Fig. 6-33 shows the normalized susceptibility curves, $\theta'(T)$ and $\theta''(T)$, obtained for the non homogeneous coated conductor $IBADt1.6a_{Gott}$. For this particular sample we have determined two different IL associated at the two peaks appearing in the $\theta''(T)$ curves.

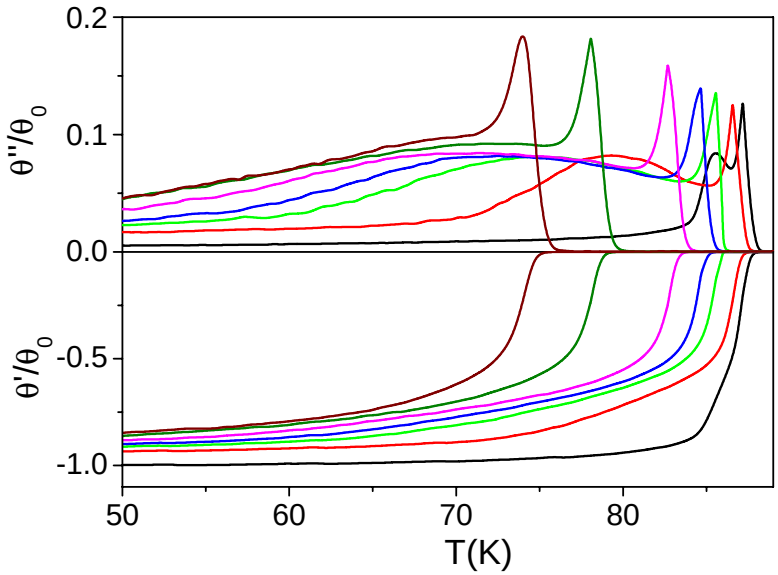

Fig. 6-33. Temperature dependence of θ'/θ_0 and θ''/θ_0 obtained for the coated conductor IBADt1.6a$_{Gott}$ at $\sigma_0 H_{ac}$=0.01mT and f=1111Hz for different applied dc fields $\sigma_0 H_{ac}$=0T, 0.1T, 0.5T, 1T, 2T, 5.5T and 9T.

Fig. 6-34 shows the irreversibility lines determined for the coated conductors IBADt1.6a$_{Gott}$ and IBADt0.23$_{Gott}$, compared with the IL found for the non-granular thin film, SCt0.2$_{THEVA}$, (see section 6.1.1). Notice that the IL determined from the high temperature peak in IBADt1.6a$_{Gott}$ is very close to those observed for the homogeneous coated conductor, IBADt0.23$_{Gott}$ and for the non-granular thin film SCt0.2$_{THEVA}$. So that, all the experimental curves, can be fitted by the same equation, $H=H_0(1-T/T_c)^B$ with B=1.42, 1.40 and 1.45 for the coated conductors IBADt0.23$_{Gott}$ and IBADt1.6a$_{Gott}$ and for the non-granular film SCt0.2$_{THEVA}$, respectively. This would indicate that the transition from an irreversible to a reversible vortex state (transition to a liquid vortex state) occurs at similar fields and temperatures, for the AV in a non-granular film than for the AJV in the coated conductor, and thus that high quality CC can approach the same results as non-granular thin film. In this situation we can consider again that both AJV and AV move in the coated conductor when we are determining the IL (region II in the phase diagram shown in section 5.3.2.c). However, the IL determined from the low temperature peak of IBADt1.6a$_{Gott}$, associated to a GB network with very low J_c^{GB}, is clearly below the other ones, and does not fit with the equation $H=H_0(1-T/T_c)^B$. In this case, the irreversibility transition occurs at lower temperatures and magnetic fields, evidencing the motion characteristics of AJV less pinned at the low J_c GBs. (open circles of Fig. 6-34).

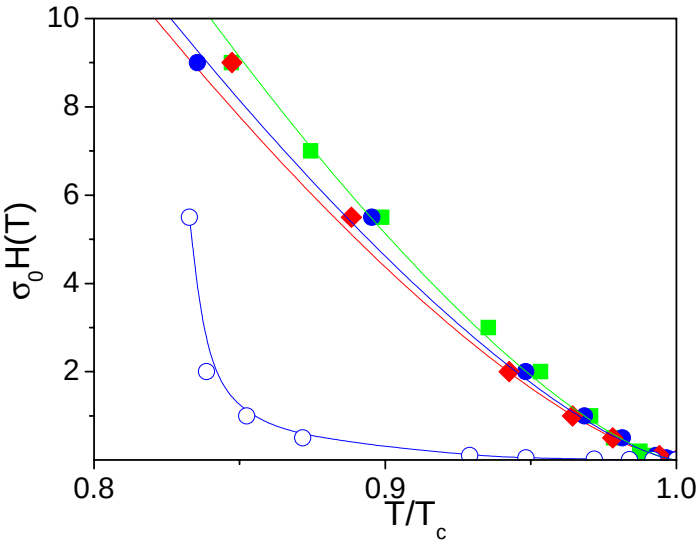

Fig. 6-34. Irreversibility lines measured for SCt0.2$_{THEVA}$ (↓), IBADt0.23$_{Gott}$ (Á) and for low (ƺ) and high (ȩ) temperature peak of IBADt1.6a$_{Gott}$.

6.4 DETERMINATION OF ACTIVATION ENERGIES

We have seen in the previous section that vortex dynamics of high temperature superconductors is a complex problem due to the extreme richness of the magnetic phase diagram. Up to now all the analysis have been performed at a fixed frequency of f=1111Hz, at different ac magnetic fields. In this section we have investigated the ac-susceptibility of YBCO coated conductors and non-granular thin films as a function of temperature in different dc-magnetic fields and frequencies, at low ac fields, $\sigma_0 H_{ac}$=0.01mT, and obtained the current and field dependence of the activation energy for depinning, $U_e(T,H_{dc},J)$, which is the height of the potential barrier that vortices must overcome when hopping from a pinning site to another.

Ac-susceptibility measurements of HTSC have revealed the importance of time effects, i.e. frequency dependence, in the determination of the critical current density due to the strong influence of flux creep. For thermally activated vortex motion, the shift in the temperature of the maximum losses, T_{peak}, with the frequency can be described in terms of an Arrhenius law [68,69,71].

$$f = f_0 \exp\left[-U_e(T,J,B)/kT_{peak}\right] \qquad 6\text{-}8$$

where f_0 is a characteristic frequency and k=8.6.10^{-5}eV/K is the Boltzman constant.

In general, the activation energy can be written as [69,71,112,113].

$$U_e(T,H_{dc},J) = U_e(T)U_e(H_{dc})U_e(J) \qquad 6\text{-}9$$

where it has been found that the dependence with temperature, applied dc-magnetic field and current density can be described by,

$$U(T,H_{dc},J) = U_0\left(1-\left(\frac{T}{T_c}\right)^{\nu}\right)^{\iota}\left(\frac{H_{dc}}{H_0}\right)^{-\eta}\left(\frac{J}{J_0}\right)^{-\mu} \qquad 6\text{-}10$$

where, U_0, H_0 and J_0 are scaling values, and ι, ν, η and σ are fitting parameters. ι and ν usually approaches the value 1.

We have applied this analysis, previously preformed in several high temperature single crystals [69,71,112,114], to non-granular YBCO thin films and coated conductors, in order to study their associated activation energies.

First of all, we present the results found for a YBCO thin film grown by BaF_2, on a single crystal, $SCt0.27_{ORNL\text{-}A}$. In order to study the field dependence of the activation energy we have analyzed the temperature of the maximum in $\theta''(T)$, T_{peak}, as a function of frequency, at different applied dc fields. Fig. 6-35 shows the Arrhenius plots ln(f) vs $1/T_{peak}$, obtained at several applied dc-magnetic fields. At each dc-magnetic field we can determine an activation energy by using the expression 6-8.

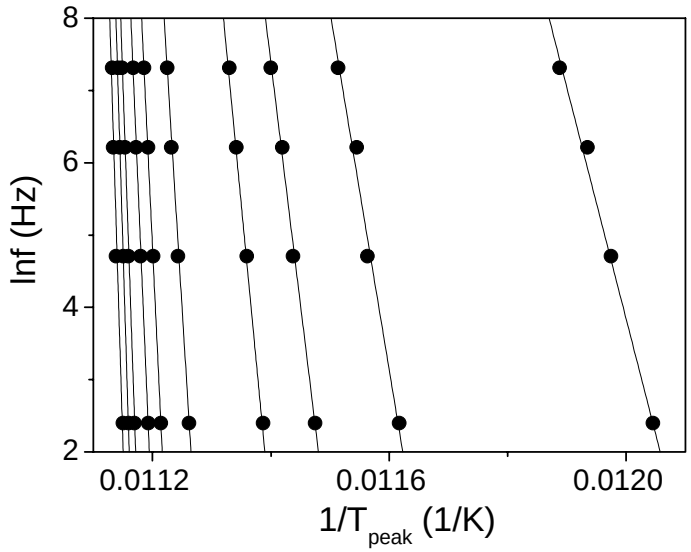

Fig. 6-35. ln(f)vs $1/T_{peak}$, measured for the non-granular film $SCt0.27_{ORNL\text{-}A}$, at $\sigma_0 H_{ac}$=0.01mT, for dc fields of $\sigma_0 H_{dc}$=0.005T, 0.01T, 0.02T, 0.05T, 0.1T, 0.2T, 0.5T, 0.7T, 1,2T and 5.5T, from left to right.

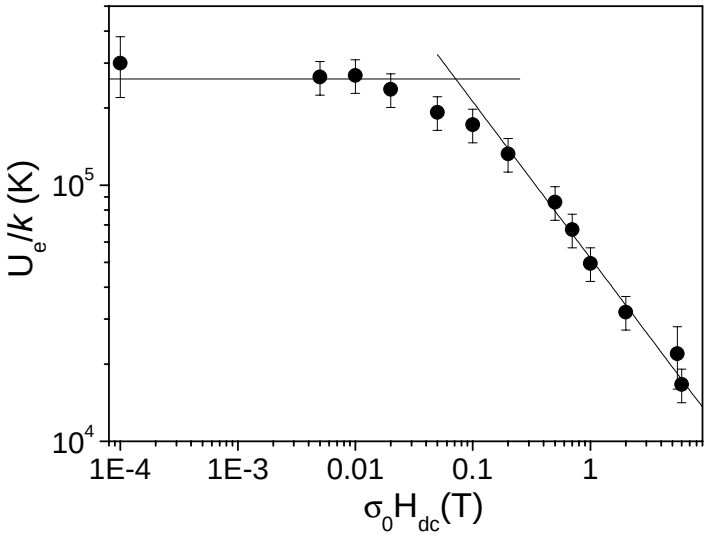

Fig. 6-36. Field dependence of the activation energy, determined for the non-granular thin film, SCt0.27$_{ORNL-A}$.

Fig. 6-36 shows the dc-magnetic field dependence of the activation energy determined for the non granular film SCt0.27$_{ORNL-A}$. We observe a plateau at low dc-magnetic fields and a power law dependence $U_e(H_{dc})\nabla(H_{dc}/H_0)^{-\eta}$ at high magnetic fields. A plateau in $U_e(H_{dc})$ can be associated to a single vortex pinning regime while the power law exponent fond at high magnetic field is similar to those observed for YBCO single crystals where $\eta \Im 0.5$ were obtained considering plastic creep [71,112,115,116]. Therefore, the crossover that we measure in the $U_e(H_{dc})$ curve, $\sigma_0 H_{cross}^{ac}$, can be correlated with the crossover determined from the analysis of $J_c^G(H)$, $\sigma_0 H_{cross}$, that also considered the transition from a single vortex pinning regime to a regime dominated for vortex-vortex interaction (see section 5.3.2.b).

In order to see if the separation of the activation energy $U_e(T,H_{dc},J)$ into the different factors $U_e(T)U_e(H_{dc})U_e(J)$ is applicable in our samples and thus, that the analysis of $U_e(H_{dc})$ does not depend on the value of J considered, we have performed the analysis of U_e at different values of θ'. i.e. different values of J, for several H_{dc} fields. Fig. 6-37 shows the curves ln(f) as a function of 1/T, determined at $\sigma_0 H_{ac}$=0.01mT and $\sigma_0 H_{dc}$=0.005T, for different values of θ'/θ_0. Notice that, an Arrhenius law can be adjusted for each curve and thus we can determine the activation energy as a function of $\theta'(J)$, by means of equation 6-8.

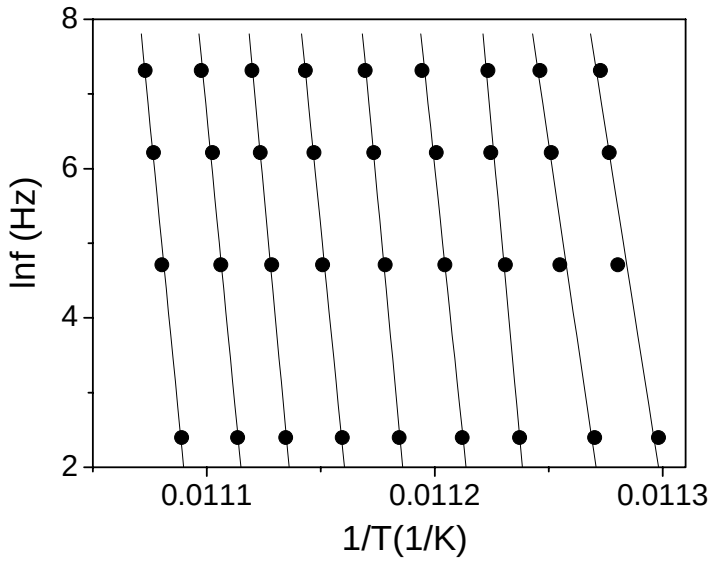

Fig. 6-37 Arrhenius plots ln(f) vs 1/T obtained for the sample SCt0.27$_{ORNL-A}$ at fixed values of θ'/θ_0 from a set of $\theta'(T)$ curves measured at several frequencies, with $\sigma_0 H_{dc}$=0.005T and $\sigma_0 H_{ac}$=0.1Oe.

The same procedure to find the curve $U_e(\theta')$ has been repeated at different dc applied fields. Results are shown in Fig. 6-38.

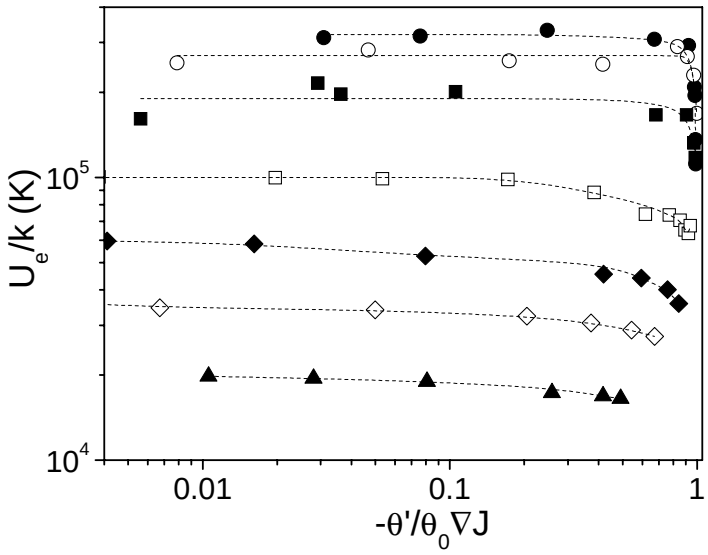

Fig. 6-38. Activation energy as a function of $\theta'\nabla J$, determined for the sample SCt0.27$_{ORNL-A}$ at $\sigma_0 H_{ac}$=0.01mT for different dc fields, $\sigma_0 H_{dc}$=0.005T (¸), 0.01T(¹), 0.1T (Â), 0.5T (Ã), 1T (ß), 2T (Ï)and 6T (¡).

By scaling the values of $U_e(\theta'(J))$ with the magnetic field according to the dependence obtained for $U_e(H_{dc})$ in Fig. 6-36, i.e. a plateau at low fields ($\sigma_0 H_{dc}$<0.01T) and a power law dependence, $U_e(H_{dc})\nabla(H_{dc}/H_0)^{-0.6}$ at high fields ($\sigma_0 H_{dc}$>0.1T), we have obtained a universal curve $U_e^{scaled}(\theta'(J))$. This result confirms then that independent dependences of the activation energy with H_{dc} and J can be considered, in agreement with equation 6-9.

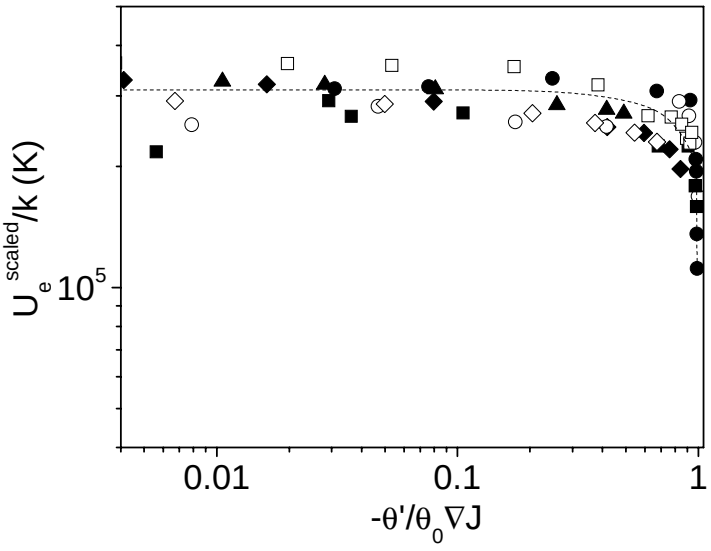

Fig. 6-39. Activation energy values determined for the sample SCt0.27$_{ORNL-A}$, scaled according the magnetic field dependence shown in Fig. 6-36 , as a function of θ'∇J, at various dc applied fields, $\sigma_0 H_{dc}$=0.005T (¸), 0.01T(¹), 0.1T (Â), 0.5T (Ã), 1T (ß), 2T (Ï)and 6 (¡).

The exact dependence of U_e with the current density, J, can be determined from the curves shown in Fig. 6-38 if we know the function θ'(J). This function is easy to find in the Bean critical state regime, where one can determine the curve $\Theta_c(\theta')$, (see section 3.3.3) which can be related with J by means of equation 3-14, i.e. $\Theta_c = H_{ac}/J(T)$. However, this is not strictly correct in our case, since we performed these measurements at too low ac field, $\sigma_0 H_{ac}$=0.01mT. Thus according to the phase diagrams shown in the previous section, we are below the critical state region, although we are in the non linear regime. Consequently, we have repeated the same analysis of $U_e(\theta')$ at a higher ac magnetic field, $\sigma_0 H_{ac}$=0.5mT, for a fixed dc applied magnetic field, $\sigma_0 H_{dc}$=0.05T. For this value of the ac field, according to the phase diagram shown in Fig. 6-32, the curves are measured within the critical state regime and thus we can determine the dependence of $U_e(J)$ from $U_e(\theta')$ by calculating the function θ'(J). Fig. 6-40 shows the experimental values $\Theta_c(\theta')$ determined for the sample SCt0.27$_{ORNL-A}$ by using two θ'(T) curves, measured at $\sigma_0 H_{ac}$=0.4mT and 0.6mT, according to the methodology described in section 3.3.3. Notice that the determination of $\Theta_c(\theta')$ described in see section 3.3.3 give us the values of Θ_c in arbitrary units. In order to find the absolute values of J_c we have considered the thin film approximation, where $J_c(T_{peak}) = 2H_{ac}/1.94t$ and that θ'/θ_0 at the peak position is θ'/θ_0= -0.38 (see sections 3.3.1 and 3.3.2).

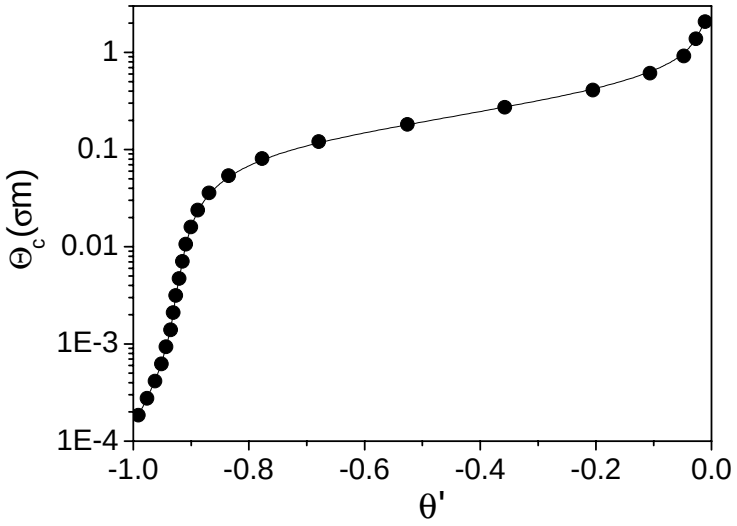

Fig. 6-40. Bean length Θ_c, as a function of θ', obtained for the sample SCt0.27$_{ORNL-A}$ through the method described in section 3.3.3.

By means of the curve shown in Fig. 6-40 and the equation 3-14, we have determined the relation $\theta'(J)$. Then we have converted the curve $U_e(J)$ determined at $\sigma_0 H_{ac}$=0.5mT and $\sigma_0 H_{dc}$=0.05T to the curve $U_e(J)$ shown in Fig. 6-41.

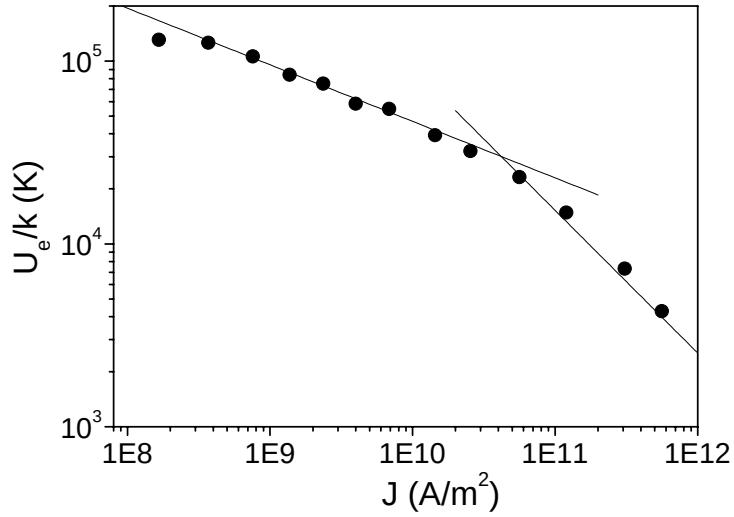

Fig. 6-41. Current density dependence of the activation energy determined for sample SCt0.27$_{ORNL-A}$ at $\sigma_0 H_{ac}$=0.5mT and $\sigma_0 H_{dc}$=0.05T.

We observe two different dependence of $U_e(J)$. At low current densities we can adjust a power law, $U_e(J) \nabla (J/J_0)^{-\sigma}$, with σ=0.3 while at high current densities we observe a stronger dependence of $U_e(J)$ with σ=0.74. The exponent fitted at high current densities is similar to that predicted for a flux creep regime caused for large vortex bundles σ=7/9 [98]. At low current densities we adjust power law dependence with a lower exponent which could be also fitted with a logarithmic dependence as it was also observed in [114,115].

Now, we will perform the same analysis of $U_e(H_{dc},J)$ to YBCO coated conductors with different GB network homogeneity in order to study the activation energies associated to the AJV pinned at the GB dislocations. Firstly we have analyzed the $U_e(H_{dc})$ dependence for a RABiTS coated conductor which presented a homogeneous GB network (one dissipation peak in the θ''(T) curve), $RABt1.41_{ORNL-C}$, and a non homogeneous IBAD coated conductor, $IBADt1.6a_{Gott}$, which presented two dissipation peaks associated to GB networks with different J_c^{GB}.

Fig. 6-42 shows the values ln(f) vs. $1/T_{peak}$, measured for the coated conductor $RABt1.41_{ORNL-C}$, at $\sigma_0 H_{ac}$=0.01mT, for several dc fields. Similar results have been obtained for the other coated conductor analyzed. From the figure we can see that an Arrhenius law (equation 6-8) can also be used to describe the $T_{peak}(f)$ dependence in coated conductors. This behaviour points to the existence of flux creep motion of AJV in the GBs as it has also been observed in [35] and thus we can determine their activation energy.

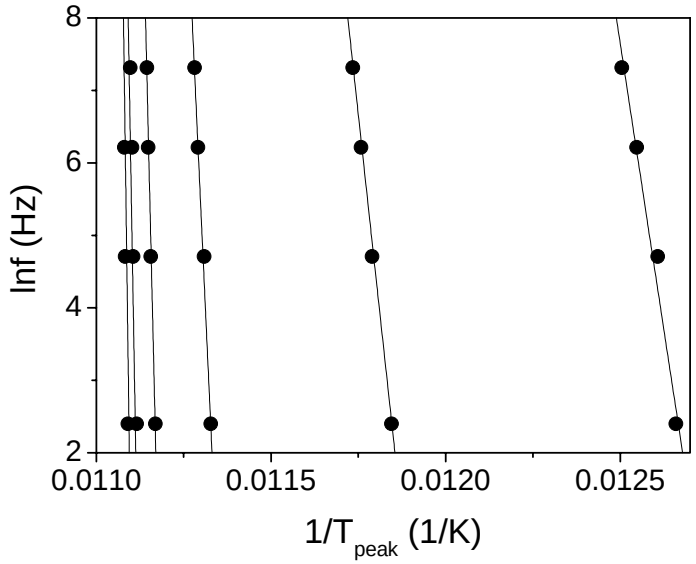

Fig. 6-42. ln(f) vs. $1/T_{peak}$, measured for the sample $RABt1.41_{ORNL-C}$ at $\sigma_0 H_{ac}$=0.01mT, for dc fields of $\sigma_0 H_{dc}$=0T, 0.005T, 0.1T,0.5T,2T and 5.5T.

Fig. 6-43 shows the dc field dependence of the activation energy, U_e, determined from the slopes of the linear fits in Fig. 6-42 for $RABt1.41_{ORNL-C}$ and for the other CC analyzed, $IBADt1.6a_{Gott}$ (in this case we have only analyzed the peak appearing at high temperatures, associated to a GB network with a high critical current density)

Notice that, as for the non-granular thin film previously analyzed (Fig. 6-36), we have obtained a plateau of U_e at low dc-magnetic fields and a power law dependence,

$U_e(H_{dc})=(H_{dc}/H_0)^{-\eta}$ at high fields. Moreover the values U_e/k obtained are also very similar than those obtained for the non-granular film for all the applied dc-magnetic fields. This results would indicate that at the high temperatures where we are performing the analysis of the activation energies, we are measuring the motion of all the vortices present in the coated conductor (AV inside the grains and AJV at the grain boundaries) and thus that we are performing the analysis of $U_e(H_{dc})$ in the region II defined in section 5.3.2.c. Moreover, we have observed, in the dynamic phase diagram analyzed in the previous section, that the transition to a Bean critical state regime occurs for the same values of ac fields and temperatures in non-granular thin films and coated conductors, indicating that there we are inducing motion of both types of vortices (AJV and AV), as well. Hence, the η exponent of the power law describes a rather complicated situation where both types of vortices move. The values of η that we have obtained are η=0.46 and 0.5 for IBADt1.6a$_{Gott}$ and RABt1.41$_{ORNL-C}$, respectively, which are very similar to the one obtained for the non-granular film SCt0.2$_{THEVA}$, η=0.6. All this exponents are consistent with the value η=0.5 obtained considering a plastic creep regime [71,112,115,116]. The plateau observed at low applied fields would be then associated to a single vortex regime where motion of AJV and AV occurs.

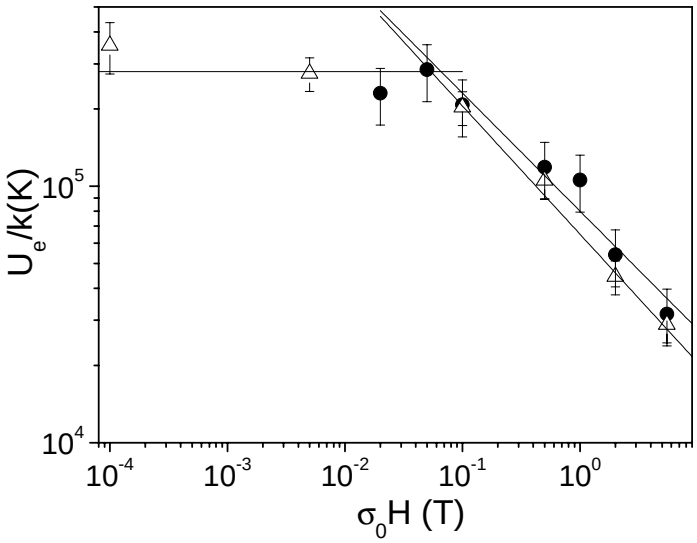

Fig. 6-43 Field dependence of the activation energy, determined for the coated conductors RABt1.41$_{ORNL-C}$ (r),IBADt1.6a$_{Gott}$ (¸).

The crossover from single vortex pinning to a regime where strong interaction between vortices have to be considered, $\sigma_0 H_{cross}^{ac}$, can be related with the crossover field determined when we analysed the field dependence of J_c^G for a non-granular thin film, $\sigma_0 H_{cross}$ although in that situation we were analyzing motion of AV and in this case we have to consider motion of both AJV and AV. So that we divide the region II

defined in section 5.3.2.c in two different regimes. Region III, above $\sigma_0 H_{cross}^{ac}$, where motion of both AJV and AV has to be considered as an interacting system and region IV (below$\sigma_0 H_{cross}^{ac}$) where also AJV and AV motion occurs but in a single vortex pinning regime (Fig. 6-45).

Additionally, we have studied the dependence of the activation energy with the current density, $U_e(J)$, for the RABiTS coated conductor, $RABt0.34_{ORNL-B}$, in the same way that we have done for the non-granular thin film $SCt0.27_{ORNL-A}$ presented above. In order to find the correct function $\Theta_c(\theta')$, we have measured the $\theta'(T)$ curves at $\sigma_0 H_{ac}$=0.5mT, within the critical state regime.

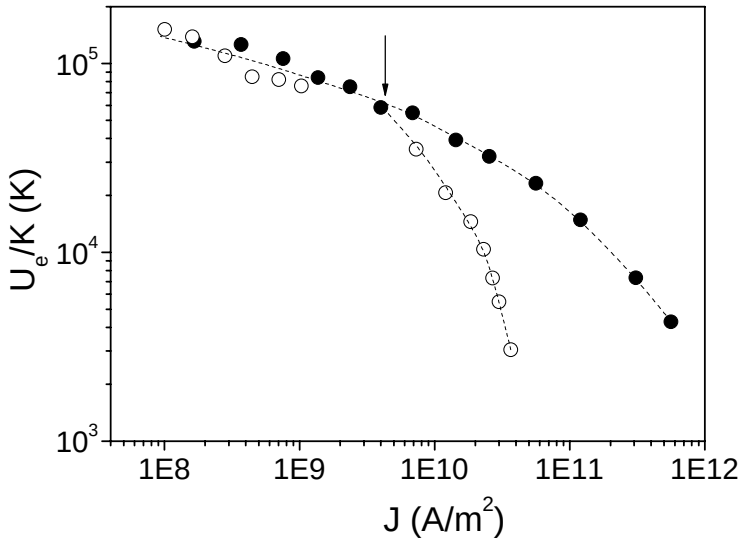

Fig. 6-44. Activation energy as a function of J determined for the coated conductor $RABt0.34_{ORNL-B}$ (open symbols) and for the non-granular film $SCt0.27_{ORNL-A}$ (closed symbols) at $\sigma_0 H_{ac}$=0.5mT and $\sigma_0 H_{dc}$=0.05T

Comparing the $U_e(J)$ curves obtained for the non-granular thin film, $SCt0.27_{ORNL-A}$, and for the coated conductor, $RABt0.34_{ORNL-B}$, we observe that at low current densities we have obtained very similar values of U_e/k which indicates that at the temperatures where we are performing the analysis we would induce motion of both AV and AJV in the coated conductor (Notice that low current densities means high temperatures). At high current densities the activation energy measured for the coated conductor is lower than that measured for the non-granular film which means that in this case (at lower temperatures) motion of less pinned AJV would occurs at lower energies than AV inside the grains and thus that in this region we are only inducing motion of AJV. At the temperature where the energies joints we can define a crossover point which separates a region where we have to consider motion of AJV from another region where we are moving AV and AJV at the same time. This crossover point,

$\sigma_0 H_{joint}^{ac}$, can be correlated with the crossing field, $\sigma_0 H_{joint}$, determined from the analysis of the $J_c^{GB}(H)$ and $J_c^{GB}(H)$ performed in section 5.3.2.c.

Finally, we present a magnetic phase diagram where we have included the different regimes of vortex motion determined by magnetization and ac-susceptibility measurements.

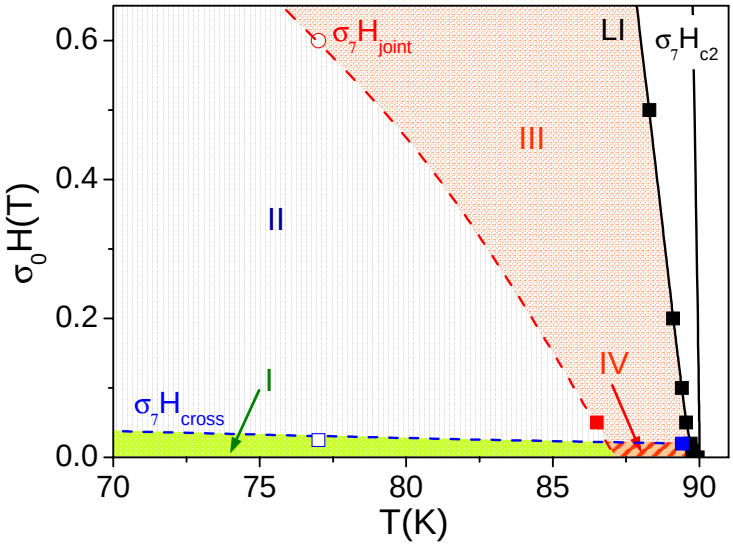

Fig. 6-45. General magnetic phase diagram for AV and AJV in a coated conductor, determined from the analysis of $J_c^{GB}(H)$, $J_c^{G}(H)$ (open symbols) and the activation energies $U_e(H_{dc},J)$ (closed symbols) where four different regimes can be described.

In this phase diagram we can distinguish between four different regimes.

For $\sigma_0 H<\sigma_0 H_{cross}$ and $\sigma_0 H<\sigma_0 H_{joint}$ (region I), we have to consider motion of AJV at the GBs ($J_c^{GB}<J_c^{G}$). In this region, we observe a plateau of $J_c^{GB}(H)$ which might be understood assuming a plastic motion of AJV in between the strongly pinned AV in the grains ($\sigma_0 H<B_A^{G}$). Hence, we consider that vortex-vortex interaction force dominates over the pinning force.

For $\sigma_0 H>\sigma_0 H_{cross}$ but $\sigma_0 H<\sigma_0 H_{joint}$ (region II), we are still measuring AJV motion ($J_c^{GB}<J_c^{G}$). In this case we observe a power law dependence $J_c^{GB}(H)\nabla H^{-0.5}$ which can be described considering AJV motion in an individual pinning regime governed by a 1D distribution of linear defects. So that, in this region the pinning force dominates over the interaction force.

For $\sigma_0 H>\sigma_0 H_{cross}$ and $\sigma_0 H>\sigma_0 H_{joint}$ (region III), we are inducing vortex motion of both AV and AJV ($J_c^{GB}=J_c^{G}$). The pinning regime that we observe is dominated by

interaction between vortices in a rather complicated situation where both AV and AJV move.

For $\sigma_0 H < \sigma_0 H_{cross}$ and $\sigma_0 H > \sigma_0 H_{joint}$ (region IV), we are also inducing vortex motion of both AV and AJV (U_e/k for the coated conductor is equal that U_e/k for the non-granular film) but in this case vortex motion is dominated by a single vortex pinning regime.

6.5 CONCLUSIONS

In this Chapter we have analyzed the ac-susceptibility response of non-granular thin films and coated conductors. In particular, we have presented evidence that a YBCO coated conductor may be understood as a network of GBs through which flux penetrates generating a global critical-state profile with a GB J_c. Different dissipative domains associated to GB networks with different critical current density have been identified in non homogeneous coated conductors. Additionally, we have estimate the area enclosed within the different dissipative domains by evaluating the parametric plots $\theta''(\theta')$. We have observed that in general the highest critical current densities are obtained for the most homogeneous samples and that it is possible to induce inhomogeneities when the conductor is mechanically deformed.

By varying the amplitude of the ac-magnetic field, we have been able to cover different regimes of vortex motion and determine a dynamic phase diagram for non-granular YBCO thin films and coated conductors. In both systems we have observed a linear response, associated to the oscillation of pinned vortices inside the potential wells (Campbell regime) at low amplitudes, while at high amplitudes a critical state develops. In between a large non linear transition is observed. We have determined the transition lines that separate the different regimes in coated conductors with different GB network homogeneity. We have observed that the onset of the Bean regime is almost the same for the non-granular thin films and coated conductors analysed indicating that the driving forces required to enter vortices into the Bean critical state regime are similar for the AJV placed at the GB than for the AV within the grains and thus that motion of both vortices should be considered. However, the transition from the non linear regime to the linear regime occurs at much lower ac fields for the non homogeneous coated conductors. By comparing the irreversibility lines obtained for the different samples, we have observed that the IL determined for homogeneous coated conductors is similar to that obtained for non-granular thin films

indicating once more, that in the coated conductor we must induce movement of both AJV and AV. For the non homogeneous samples, different IL can be determined associated to GB networks with different critical current density. In that case the IL associated to GB domains with low critical current density is clearly below the one associated to high critical current density GB networks.

Finally, by analysing the ac-susceptibility curves of non-granular thin films and coated conductors at different frequencies we have determined the thermal activation energy as a function of the dc applied field, H_{dc}, and the current density, J, $U_e(H_{dc},J)$, and we have observed that both dependences can be analyzed separately.

Similar values of $U_e(H_{dc})$ have been obtained for non-granular films and coated conductors indicating that also in this case, at the high temperatures where we are performing the analysis of the activation energies, we are measuring motion of both AJ and AJV. We have identified two different regimes in the $U_e(H_{dc})$ curve, a plateau at low H_{dc} (associated to single vortex pinning) and a power law dependence, $U_e(H_{dc})=(H_{dc}/ H_0)^{-\eta}$, with $\eta \Im 0.5$, which can be described considering a plastic creep regime. The crossover from these two different regimes has been related to the crossover that we measure in section 5 for non-granular thin films, $\sigma_0 H_{cross}$, which defines the transition from a single vortex pinning to a collective pinning regime but in this case we are measuring motion of both AJV and AJ.

By analysing the dependence of $U_e(J)$, we have determined the crossover field, $\sigma_0 H_{joint}^{ac}$, which marks the point where the activation energy measured for the coated conductor merge with the activation energy of a non-granular film. This crossover field has been correlated with the joining field determined from J_c measurements in section 5, $\sigma_0 H_{joint}$.

Finally, by considering all the crossing fields determined by analysing $J_c(H)$ in section 5 and $U_e(H_{dc},J)$ we have build consistent magnetic phase diagram where distinct vortex motion regimes can be identified.

CHAPTER 7

GENERAL CONCLUSIONS

In this thesis we have presented a complete analysis of the electromagnetic response measured for non-granular thin films and coated conductors by means of dc-magnetometry and ac-susceptibility. We have studied the principal effects that the granular nature of coated conductors induces in their magnetic behaviour.

We have shown that it is possible to identify the granularity present in a coated conductor simply by measuring its hysteresis loop since it shows an unconventional behaviour with a maximum in the reverse magnetization curve at a positive applied magnetic field instead of at zero field as expected for a superconducting thin film without granularity. The detected shift in the peak position has been ascribed to granularity effects due to the return field that grains induce at the grain boundaries (GBs). By analysing several hysteresis loops at different applied fields we have devolved a methodology able to determine the grain, J_c^G, and grain boundary, J_c^{GB} critical current densities for a given coated conductor and additionally its average

magnetic grain size, <2a>. We have verified the validity of the formalism developed and its assumptions by applying the methodology to different situations. We have been able to reproduce the experimental hysteresis loops only by assuming the contribution of the return field at the grain boundaries. Moreover we have observed the same phenomenon by means of complementary techniques such us magneto optical imaging and critical current transport measurements.

The simplicity of the methodology developed has allowed us to determine the values of J_c^G and J_c^{GB} at about zero field and <2a> for a number of IBAD and RABiTS coated conductors and analyze their dependence on fundamental parameters such us YBCO grain size, texture of the YBCO layer, thickness of the YBCO layer, growing process as well as effects from modifications induced at the grain boundaries by mechanical deformation of the tapes.

We have shown that the values of magnetic grain size that we determine by magnetization measurements are in agreement with the structural ones measured by EBSD and that these values differ in one order of magnitude in IBAD and RABiTS coated conductors, <2a>≈0.5-2.5σm for IBAD CCs and <2a>≈20-100σm for RABiTS CCs. By analyzing samples grown by ex situ BaF_2 based precursors using different growing conditions we have observed that it is possible to increase the percolative critical current density, J_c^{GB}, in a coated conductor by changing the nature or the effective length of the grain boundaries without changing J_c^G, i.e. without modifying pining inside the grains.

By analysing samples with different texture we have studied the dependence of J_c^G and J_c^{GB} with the GB misorientation. We have observed that J_c^{GB} decreases exponentially with the misorientation angle while J_c^G is not affected. From this we can conclude that the GB misorientation is a clear limitation factor for the critical current density that percolates through the sample and that texture has to be improved as much in coated conductors in order to achieve high critical current densities.

YBCO coated conductors with similar texture and different thickness have been analyzed in order to find the dependence of J_c^G and J_c^{GB} with the YBCO thickness. We have found that both J_c^G and J_c^{GB} decreases when we increase the YBCO thickness indicating that there exists a correlation between both critical current densities. Based in these results we have proposed an interaction between Abrikosov vortices (AV) located inside the grains and Abrikosov Josephson vortices (AJV) at the GBs, which

assumes that strong pinned AV in the grains could hold AJV in the GBs retarding its motion.

By measuring the field dependence of J_c^G for YBCO non-granular thin films, and J_c^{GB} for YBCO coated conductors we have identified different vortex motion regimes in both systems.

For the non-granular films we have determined a crossover field $\sigma_0 H_{cross} \Im B_A$, that separates a region with J_c independent of the magnetic filed (for $\sigma_0 H < \sigma_0 H_{cross}$) from another region with $J_c(H) \nabla H^{-\zeta}$. The observed plateau can be described considering a single vortex pinning regime while the power law corresponds to an interacting regime where interstitial Abrikosov vortices should be considered. The exponent ζ varies from 0.5 to 1, according to motion of Abrikosov vortex bundles in a plastic or collective pinning regime, respectively. When approaching the irreversibility field, we have found a fast decrease of $J_c(H)$.

For YBCO coated conductors we have also observed a crossover field, $\sigma_0 H_{cross}^{CC}$, that separates a plateau of J_c from a power law dependence of $J_c(H) \nabla H^{-\zeta}$. However, in this case $\sigma_0 H_{cross}^{CC}$ cannot be related with the matching field associated to the GB dislocations, since it is always higher than the applied magnetic field, $B_A^{GB} \Im 100T$, but it can be related with the matching field associated to the coated conductor grains, $\sigma_0 H_{cross}^{CC} \Im B_A^G$. Additionally we have obtained for all the coated conductors analyzed an exponent $\zeta \Im 0.5$. The plateau observed at low magnetic fields have been associated to a plastic motion of AJV in a channel surrounded of strongly pinned AV ($\sigma_0 H < B_A^G$) while the power law behaviour has been described by considering an individual vortex pinning regime governed by a 1D distribution of linear defects. These results would indicate that when interstitial vortices appears at the grains, the AJV motion change form a strong interacting system of AV-AJV to a system governed by an individual vortex pinning regime at the GBs.

Additionally, another crossing field has been identified at higher magnetic fields, $\sigma_0 H_{joint}$, which determines the point where J_c^{GB} and J_c^G merge and thus, marks the transition to a regime where both AJV and AV move. From the values $\sigma_0 H_{cross}^{CC}$ and $\sigma_0 H_{joint}$ determined at different temperatures we have build up a magnetic phase diagram describing the three different regimes found for vortex motion in coated conductors.

By means of ac-susceptibility measurements we have analyzed the ac-susceptibility response of coated conductors and non-granular thin films. We have evidenced that a coated conductor may be understood as a network of GBs through which flux penetrates generating a critical-state with a J_c^{GB}. By analysing the parametric plots $\theta''(\theta')$ for non homogeneous coated conductors we have identified different dissipative domains associated to GB networks with different J_c^{GB}.

By analysing the ac-susceptibility curves measured for non-granular films and coated conductors at different ac field amplitudes, we have identified different regimes of vortex motion. At low ac fields we have observed a linear response associated to the Campbell regime, at higher fields we have identified the transition to a critical state and in between of these two regimes we have found a non linear region. We have determined the transition lines that separate the different regions for a non-granular film and for different coated conductors and we have build their dynamic phase diagram. The transition line to the critical state regime and also the irreversibility line appear at similar temperatures and ac fields for both systems indicating that at the large temperatures and ac fields where we are performing the analysis, motion of AV and AJV should be considered. On the contrary the transition line which separates the non linear and the linear regime appears to be different, being lower for non homogeneous coated conductors.

We have determined the thermal activation energy U_e, as a function of the dc applied field, H_{dc}, and the current density, J, for coated conductors and non-granular films. We have observed that both dependences can be decoupled and analyzed separately.

By comparing the $U_e(H_{dc})$ curves found for non-granular films and coated conductors we have observed that the values of U_e and also the dependences with H_{dc}, are very similar in both systems. From this result we conclude that at the high temperatures where we are performing the analysis of the activation energies we are also measuring motion of both AJ and AJV in the CCs. We have identified two different regimes in the $U_e(H_{dc})$ curve, a plateau at low H_{dc} associated to a single vortex pinning and a power law dependence $U_e(H_{dc})=(H_{dc}/H_0)^{-\eta}$, with $\eta \Im 0.5$, which can be described considering a plastic creep regime. The crossover from these two different regimes can be related with the crossover that we measure in the field dependence J_c for non-granular thin films, $\sigma_0 H_{cross}$, which defines the transition from a single vortex pinning to

a collective pinning regime but in this case for coated conductors we are measuring movement of both AJV and AJ.

By analysing the dependence of $U_e(J)$, we have found that similar values of U_e are obtained at low current densities for coated conductors and non-granular films while at high current densities the activation energy measured for coated conductors is lower than that obtained for non-granular films. We have defined a crossover point that separates the region where similar energies are detected (region where motion of AJV and AJ has to be considered) from the region where the activation energy is lower for coated conductors (where we only should consider motion of AJV). This crossover point seems to correlate with the crossing field, $\sigma_0 H_{joint}$, determined from the analysis of the critical current density.

Finally, we include the different vortex regimes in a single magnetic phase diagram where both the magnetization and the ac-susceptibility results are joined and which enables us to describe the general behaviour of AJV and AV in coated conductors.

BIBLIOGRAPHY

1. J. R. Waldram, *Superconductivity of Metals and Cuprates*, Edited by Institut of Physics Publishing, (1996).
2. J. Bardeen, L. N. Cooper, and J. R. Schrieffer, Physical Review **108,** 1175 (1957).
3. J. G. Bednorz and K. A. Muller, Zeitschrift fur Physik B-Condensed Matter **64,** 189 (1986).
4. K. H. Fischer and T. Nattermann, Physical Review B **43,** 10372 (1991).
5. M. P. A. Fisher, Physical Review Letters **62,** 1415 (1989).
6. G. Blatter, M. V. Feigelman, V. B. Geshkenbein, A. I. Larkin, and V. M. Vinokur, Reviews of Modern Physics **66,** 1125 (1994).
7. D. R. Nelson and V. M. Vinokur, Physical Review B **48,** 13060 (1993).
8. D. R. Nelson, Physical Review Letters **60,** 1973 (1988).
9. A. Houghton, R. A. Pelcovits, and A. Sudbo, Physical Review B **40,** 6763 (1989).
10. D. R. Nelson and V. M. Vinokur, Physical Review Letters **68,** 2398 (1992).
11. M. Charalambous, J. Chaussy, P. Lejay, and V. Vinokur, Physical Review Letters **71,** 436 (1993).
12. H. Safar, P. L. Gammel, D. A. Huse, D. J. Bishop, J. P. Rice, and D. M. Ginsberg, Physical Review Letters **69,** 824 (1992).
13. R. H. Koch, V. Foglietti, W. J. Gallagher, G. Koren, A. Gupta, and M. P. A. Fisher, Physical Review Letters **63,** 1511 (1989).
14. M. Suenaga, A. K. Ghosh, Y. W. Xu, and D. O. Welch, Physical Review Letters **66,** 1777 (1991).

15. P. W. Anderson, Physical Review Letters **9,** 309-& (1962).

16. M. Tinkham, *Introduction to Superconductivity*, Edited by McGraw-Hill, New York (1975).

17. E. H. Brandt, Physica C **195,** 1 (1992).

18. E. H. Brandt, Physical Review B **55,** 14513 (1997).

19. M. V. Feigel'man, V. B. Geshkenbein, A. I. Larkin, and V. M. Vinokur, Physical Review Letters **63,** 2303 (1989).

20. M. F. Chisholm and S. J. Pennycook, Nature **351,** 47 (1991).

21. D. Dimos, P. Chaudhari, J. Mannhart, and F. K. Legoues, Physical Review Letters **61,** 219 (1988).

22. D. Dimos, P. Chaudhari, and J. Mannhart, Physical Review B **41,** 4038 (1990).

23. H. Hilgenkamp and J. Mannhart, Reviews of Modern Physics **74,** 485 (2002).

24. D. Larbalestier, A. Gurevich, D. M. Feldmann, and A. Polyanskii, Nature **414,** 368 (2001).

25. A. Gurevich and E. A. Pashitskii, Physical Review B **57,** 13878 (1998).

26. D. T. Verebelyi, D. K. Christen, R. Feenstra, C. Cantoni, A. Goyal, D. F. Lee, M. Paranthaman, P. N. Arendt, R. F. DePaula, J. R. Groves, and C. Prouteau, Applied Physics Letters **76,** 1755 (2000).

27. E. Sarnelli, P. Chaudhari, and J. Lacey, Applied Physics Letters **62,** 777 (1993).

28. A. Diaz, L. Mechin, P. Berghuis, and J. E. Evetts, Physical Review Letters **80,** 3855 (1998).

29. A. Gurevich, Physical Review B **46,** 3638 (1992).

30. A. Gurevich and L. D. Cooley, Physical Review B **50,** 13563 (1994).

31. A. Gurevich, Physical Review B **65,** (2002).

32. A. Diaz, L. Mechin, P. Berghuis, and J. E. Evetts, Physical Review B **58,** R2960-R2963 (1998).

33. M. J. Hogg, F. Kahlmann, E. J. Tarte, Z. H. Barber, and J. E. Evetts, Applied Physics Letters **78,** 1433 (2001).

34. C. Jooss, K. Guth, V. Born, and J. Albrecht, Physical Review B **65,** (2002).

35. D. X. Chen, E. Pardo, A. Sanchez, A. Palau, T. Puig, and X. Obradors, Applied Physics Letters **85,** 5646 (2004).

36. K. Heine, J. Tenbrink, and M. Thoner, Applied Physics Letters **55,** 2441 (1989).

37. Q. Li, G. N. Riley, R. D. Parrella, S. Fleshler, M. W. Rupich, W. L. Carter, J. O. Willis, J. Y. Coulter, J. F. Bingert, V. K. Sikka, J. A. Parrell, and D. C. Larbalestier, Ieee Transactions on Applied Superconductivity **7,** 2026 (1997).

38. T. Araki, H. Kurosaki, Y. Yamada, I. Hirabayashi, J. Shibata, and T. Hirayama, Superconductor Science & Technology **14,** 783 (2001).

39. M. Paranthaman, T. G. Chirayil, S. Sathyamurthy, D. B. Beach, A. Goyal, F. A. List, D. F. Lee, X. Cui, S. W. Lu, B. Kang, E. D. Specht, P. M. Martin, D. M. Kroeger, R. Feenstra, C. Cantoni, and D. K. Christen, Ieee Transactions on Applied Superconductivity **11,** 3146 (2001).

40. A. Usoskin, J. Knoke, F. Garcia-Moreno, A. Issaev, J. Dzick, S. Sievers, and H. C. Freyhardt, Ieee Transactions on Applied Superconductivity **11,** 3385 (2001).

41. J. Dzick, J. Wiesmann, J. Hoffmann, K. Heinemann, F. Garcia-Moreno, A. Isaev, H. C. Freyhardt, and W. Lechner, Ieee Transactions on Applied Superconductivity **9,** 2248 (1999).

42. Y. Iijima, K. Onabe, N. Futaki, N. Tanabe, N. Sadakata, O. Kohno, and Y. Ikeno, Journal of Applied Physics **74,** 1905 (1993).

43. S. R. Foltyn, P. N. Arendt, P. C. Dowden, R. F. DePaula, J. R. Groves, J. Y. Coulter, Q. Jia, M. P. Maley, and D. E. Peterson, Ieee Transactions on Applied Superconductivity **9,** 1519 (1999).

44. B. De Boer, J. Eickemeyer, N. Reger, L. Fernandez, J. Richter, B. Holzapfel, L. Schultz, W. Prusseit, and P. Berberich, Acta Materialia **49,** 1421 (2001).

45. D. P. Norton, A. Goyal, J. D. Budai, D. K. Christen, D. M. Kroeger, E. D. Specht, Q. He, B. Saffian, M. Paranthaman, C. E. Klabunde, D. F. Lee, B. C. Sales, and F. A. List, Science **274,** 755 (1996).

46. C. Park, D. P. Norton, D. K. Christen, D. T. Verebelyi, R. Feenstra, J. D. Budai, A. Goyal, D. F. Lee, E. D. Specht, D. M. Kroeger, and M. Paranthaman, Ieee Transactions on Applied Superconductivity **9,** 2276 (1999).

47. J. E. Evetts, M. J. Hogg, B. A. Glowacki, N. A. Rutter, and V. N. Tsaneva, Superconductor Science & Technology **12,** 1050 (1999).

48. D. M. Feldmann, J. L. Reeves, A. A. Polyanskii, G. Kozlowski, R. R. Biggers, R. M. Nekkanti, I. Maartense, M. Tomsic, P. Barnes, C. E. Oberly, T. L. Peterson, S. E. Babcock, and D. C. Larbalestier, Applied Physics Letters **77,** 2906 (2000).

49. D. M. Feldmann, D. C. Larbalestier, D. T. Verebelyi, W. Zhang, Q. Li, G. N. Riley, R. Feenstra, A. Goyal, D. F. Lee, M. Paranthaman, D. M. Kroeger, and D. K. Christen, Applied Physics Letters **79,** 3998 (2001).

50. B. Holzapfel, L. Fernandez, F. Schindler, B. De Boer, N. Reger, J. Eickemeyer, P. Berberich, and W. Prusseit, Ieee Transactions on Applied Superconductivity **11,** 3872 (2001).

51. N. A. Rutter, B. A. Glowacki, and J. E. Evetts, Superconductor Science & Technology **13,** L25-L30 (2000).

52. E. D. Specht, A. Goyal, and D. M. Kroeger, Superconductor Science & Technology **13,** 592 (2000).

53. A. Forkl, C. Jooss, R. Warthmann, H. Kronmuller, and H. U. Habermeier, Journal of Alloys and Compounds **251,** 146 (1997).

54. M. R. Koblischka and R. J. Wijngaarden, Superconductor Science & Technology **8,** 199 (1995).

55. A. A. Polyanskii, A. Gurevich, A. E. Pashitski, N. F. Heinig, R. D. Redwing, J. E. Nordman, and D. C. Larbalestier, Physical Review B **53,** 8687 (1996).

56. C. Jooss, J. Albrecht, H. Kuhn, S. Leonhardt, and H. Kronmuller, Reports on Progress in Physics **65,** 651 (2002).

57. R. Feenstra, T. B. Lindemer, J. D. Budai, and M. D. Galloway, Journal of Applied Physics **69,** 6569 (1991).

58. R. Feenstra, *Submitted to Ieee Transactions on Applied Superconductivity*

59. J. R. Clem and A. Sanchez, Physical Review B **50,** 9355 (1994).

60. C. P. Bean, Physical Review Letters **8,** 250-& (1962).

61. C. P. Bean, Reviews of Modern Physics **36,** 31-& (1964).

62. A. Sanchez and C. Navau, Physical Review B **64,** 214506-214506-10 (2001).

63. J. McDonald and J. R. Clem, Physical Review B **53,** 8643 (1996).

64. D. X. Chen, A. Sanchez, J. Nogues, and J. S. Munoz, Physical Review B **41,** 9510 (1990).

65. A. Sanchez and C. Navau, Superconductor Science & Technology **14,** 444 (2001).

66. D. X. Chen and R. B. Goldfarb, Journal of Applied Physics **66,** 2489 (1989).

67. T. H. Johansen and H. Bratsberg, Journal of Applied Physics **77,** 3945 (1995).

68. F. Gomory, Superconductor Science & Technology **10,** 523 (1997).

69. G. Pasquini, L. Civale, H. Lanza, and G. Nieva, Physical Review B **59,** 9627 (1999).

70. D. V. Shantsev, Y. M. Galperin, and T. H. Johansen, Physical Review B **61,** 9699 (2000).

71. L. Fabrega, J. Fontcuberta, L. Civale, and S. Pinol, Physical Review B **50,** 1199 (1994).

72. M. Nikolo and R. B. Goldfarb, Physical Review B **39,** 6615 (1989).

73. A. M. Campbell and J. E. Evetts, Advances in Physics **21,** 199-& (1972).

74. J. R. Thompson, L. KrusinElbaum, L. Civale, G. Blatter, and C. Feild, Physical Review Letters **78,** 3181 (1997).

75. A. Sanchez and E. Pardo, Private Communication.

76. K. H. Muller, C. Andrikidis, and Y. C. Guo, Physical Review B **55,** 630 (1997).

77. D. V. Shantsev, M. R. Koblischka, Y. M. Galperin, T. H. Johansen, L. Pust, and M. Jirsa, Physical Review Letters **82,** 2947 (1999).

78. J. R. Thompson, H. J. Kim, C. Cantoni, D. K. Christen, R. Feenstra, and D. T. Verebelyi, Physical Review B **69,** (2004).

79. J. E. Evetts and B. A. Glowacki, Cryogenics **28,** 641 (1988).

80. M. J. Hogg, F. Kahlmann, Z. H. Barber, and J. E. Evetts, Superconductor Science & Technology **14,** 647 (2001).

81. A. Palau, T. Puig, X. Obradors, E. Pardo, C. Navau, A. Sanchez, A. Usoskin, H. C. Freyhardt, L. Fernandez, B. Holzapfel, and R. Feenstra, Applied Physics Letters **84,** 230 (2004).

82. T. G. Holesinger, *Submitted to Journal of Materials Research*

83. P. C. Mcintyre, M. J. Cima, and M. F. Ng, Journal of Applied Physics **68,** 4183 (1990).

84. V. F. Solovyov, H. J. Wiesmann, and M. Suenaga, Physica C **353,** 14 (2001).

85. D. M. Feldmann, *Submitted to Journal of Materials Research*

86. D. M. Feldmann, D. C. Larbalestier, R. Feenstra, A. A. Gapud, J. D. Budai, T. G. Holesinger, and P. N. Arendt, Applied Physics Letters **83,** 3951 (2003).

87. S. R. Foltyn, P. N. Arendt, Q. X. Jia, H. Wang, J. L. MacManus-Driscoll, S. Kreiskott, R. F. DePaula, L. Stan, J. R. Groves, and P. C. Dowden, Applied Physics Letters **82,** 4519 (2003).

88. R. Feenstra, *Annual Peer Review, 2004*

89. D. M. Feldmann, *Annual Peer Review, 2004*

90. T. G. Holesinger, *Annual Peer Review, 2004*

91. G. Doornbos, B. Dam, J. C. Martinez, R. Surdeanu, U. Poppe, and R. Griessen, Physica C **282,** 2303 (1997).

92. B. Dam, J. M. Huijbregtse, F. C. Klaassen, R. C. F. van der Geest, G. Doornbos, J. H. Rector, A. M. Testa, S. Freisem, J. C. Martinez, B. Stauble-Pumpin, and R. Griessen, Nature **399,** 439 (1999).

93. J. M. Huijbregtse, F. C. Klaassen, A. Szepielow, J. H. Rector, B. Dam, R. Griessen, B. J. Kooi, and J. T. M. de Hosson, Superconductor Science & Technology **15,** 395 (2002).

94. F. C. Klaassen, G. Doornbos, J. M. Huijbregtse, R. C. F. van der Geest, B. Dam, and R. Griessen, Physical Review B **64,** 184523 (2001).

95. L. KrusinElbaum, L. Civale, J. R. Thompson, and C. Feild, Physical Review B **53,** 11744 (1996).

96. J. M. Huijbregtse, B. Dam, R. C. F. van der Geest, F. C. Klaassen, R. Elberse, J. H. Rector, and R. Griessen, Physical Review B **62,** 1338 (2000).

97. L. Civale, A. D. Marwick, T. K. Worthington, M. A. Kirk, J. R. Thompson, L. KrusinElbaum, Y. Sun, J. R. Clem, and F. Holtzberg, Physical Review Letters **67,** 648 (1991).

98. P. J. Kung, M. P. Maley, M. E. Mchenry, J. O. Willis, M. Murakami, and S. Tanaka, Physical Review B **48,** 13922 (1993).

99. M. O. Andre, M. Polichetti, H. Pastoriza, and P. H. Kes, Physica C-Superconductivity and Its Applications **338,** 179 (2000).

100. H. Pastoriza and P. H. Kes, Physical Review Letters **75,** 3525 (1995).

101. A. Pruymboom, P. H. Kes, E. Vanderdrift, and S. Radelaar, Physical Review Letters **60,** 1430 (1988).

102. L. Fernandez, Thesis; *Grain boundary networks in RABiTS based $YBa_2Cu_3O_{7-d}$ coated conductors,* 2004

103. C. Park, D. P. Norton, J. D. Budai, D. K. Christen, D. Verebelyi, R. Feenstra, D. F. Lee, A. Goyal, D. M. Kroeger, and M. Paranthaman, Applied Physics Letters **73,** 1904 (1998).

104. N. Cheggour, J. W. Ekin, C. C. Clickner, D. T. Verebelyi, C. L. H. Thieme, R. Feenstra, and A. Goyal, Applied Physics Letters **83,** 4223 (2003).

105. D. X. Chen, A. Sanchez, T. Puig, L. M. Martinez, and J. S. Munoz, Physica C **168,** 652 (1990).

106. T. Herzog, H. A. Radovan, P. Ziemann, and E. H. Brandt, Physical Review B **56,** 2871 (1997).

107. L. Civale, T. K. Worthington, and A. Gupta, Physical Review B **43,** 5425 (1991).

108. L. KrusinElbaum, L. Civale, F. Holtzberg, A. P. Malozemoff, and C. Feild, Physical Review Letters **67,** 3156 (1991).

109. E. Rodriguez, A. Gou, B. Martinez, S. Pinol, and X. Obradors, Physical Review B **57,** 8687 (1998).

110. K. A. Muller, M. Takashige, and J. G. Bednorz, Physical Review Letters **58,** 1143 (1987).

111. T. Puig, A. Palau, X. Obradors, E. Pardo, C. Navau, A. Sanchez, Ch. Jooss, H. C. Guth, H. C. Freyhardt, and J. G. Bednorz, Superconductor Science and Technology **17,** 1283 (2004).

112. P. J. Kung, M. P. Maley, M. E. Mchenry, J. O. Willis, J. Y. Coulter, M. Murakami, and S. Tanaka, Physical Review B **46,** 6427 (1992).

113. M. J. Qin, X. Jin, H. L. Ji, Z. X. Shi, X. X. Yao, Z. G. Fan, and Y. Q. Shan, Journal of Applied Physics **77,** 2618 (1995).

114. J. Li, S. Y. Ding, J. S. Zhu, H. M. Shao, and Y. N. Wang, Journal of Applied Physics **77,** 6398 (1995).

115. M. J. Qin, S. Y. Ding, C. Ren, X. X. Yao, Y. X. Fu, C. B. Cai, T. S. Shi, and G. Y. Wang, Physica C **262,** 127 (1996).

116. V. M. Vinokur, M. V. Feigelman, V. B. Geshkenbein, and A. I. Larkin, Physical Review Letters **65,** 259 (1990).